

Ramsey-comb spectroscopy

VRIJE UNIVERSITEIT

Ramsey-comb spectroscopy

ACADEMISCH PROEFSCHRIFT

ter verkrijging van de graad Doctor aan
de Vrije Universiteit Amsterdam,
op gezag van de rector magnificus
prof.dr. F.A. van der Duyn Schouten,
in het openbaar te verdedigen
ten overstaan van de promotiecommissie
van de Faculteit der Exacte Wetenschappen
op woensdag 18 juni 2014 om 11.45 uur
in de aula van de universiteit,
De Boelelaan 1105

door

Jonas Morgenweg

geboren te Kamen, Duitsland

promotor: prof.dr. K.S.E. Eikema

To the girl I love

*So eine Fliege fragt nicht, wie funktioniert die Welt, das Universum.
Menschen stellen solche Fragen und dann werden sie Physiker vom
Beruf und finden heraus, wir leben in einem elfdimensionalen
Raum-Zeit-Kontinuum im Quantenschaum. Ob wir mit dieser
Erkenntnis jetzt so viel weiter sind als die Fliege, wage ich zu
bezweifeln. Aber so ist der Mensch, begreift auch nichts, aber auf
höherem Niveau.*

Adapted from Dieter Nuhr, German comedian (born 1960).

This thesis was approved by the members of the reviewing committee:

- Prof. Dr. H.J. Bakker
(FOM-Institute AMOLF, Amsterdam)
- Prof. Dr. T.J. Kippenberg
(École Polytechnique Fédérale de Lausanne)
- Prof. Dr. E.J.G. Peterman
(VU University Amsterdam)
- Prof. Dr. F. Riehle
(Physikalisch-Technische Bundesanstalt, Braunschweig)
- Prof. Dr. W.J. van der Zande
(Radboud University Nijmegen)



The work described in this thesis was performed as part of a research program of the Netherlands Organization for Scientific Research (NWO) and was carried out at the LaserLaB Amsterdam, VU University Amsterdam (De Boelelaan 1083, 1081 HV Amsterdam, The Netherlands). Investment support was provided by the EC's Seventh Framework Programme LASERLAB EUROPE and the Foundation for Fundamental Research on Matter (FOM).

Cover design: Dr. Nandana Acharjee provided the drafts for the girls on the swings. The surrounding “wiggles” are based on actual Ramsey-comb signals of atomic rubidium as described in Ch. 5 of this thesis.

ISBN: 978-94-6259-185-1

Printed by Ipskamp Drukkers B.V., Enschede

CONTENTS

CHAPTER 1: INTRODUCTION	1
1.1 Ramsey spectroscopy or the girl on the swing	1
1.2 Coherent pulse trains from optical frequency combs . . .	3
1.2.1 More power for challenging spectroscopy targets	3
1.3 Less can be more: Ramsey-comb spectroscopy	4
1.4 Short outline of this thesis	6
CHAPTER 2: PRELIMINARY: ELECTROMAGNETIC WAVES, FREQUENCY COMBS AND PULSE AMPLIFICATION	7
2.1 Electromagnetic waves in (non)linear media	7
2.2 Pulse propagation in time and space	9
2.2.1 Carrier-envelope phase and group velocity dispersion	11
2.2.2 A practical example: Temporal broadening of a Gaussian pulse	12
2.3 Pulse pairs and pulse trains	14
2.4 Frequency combs	16
2.4.1 On the technical realization of optical frequency combs	17
2.5 Phase-coherent optical parametric amplification	18
2.5.1 Numerical solutions to the coupled-wave equations	21
2.6 Amplification in laser gain media	22
2.6.1 Gain and saturation in short-pulse amplification	22
2.6.2 Grazing-incidence amplifiers	24
CHAPTER 3: THE DOUBLE-PULSE PUMP AMPLIFIER SYSTEM	27
3.1 The master oscillator	28
3.1.1 Laser gain material and diode pumping	28
3.1.2 The laser cavity	29
3.1.3 Repetition-rate control	30
3.2 Tailored pulse sequences from an 880 nm pumped Nd:YVO ₄ bounce amplifier	31
3.2.1 Introduction	31
3.2.2 Experimental setup	32

3.2.3	Amplifier performance and modeling	34
3.2.4	Conclusion	37
3.3	A 1.8 mJ, picosecond Nd:YVO ₄ bounce-amplifier pump front-end system for high-accuracy XUV-frequency comb spectroscopy	38
3.3.1	Introduction	38
3.3.2	Experimental setup	38
3.3.3	Results and discussion	41
3.3.4	Conclusion	43
3.4	Post-amplification to the 100 millijoule-level	44
3.4.1	Flashlamp-pumped amplifier in ring geometry	44
3.4.2	Amplification with diode-pumped modules	45

CHAPTER 4: MULTI-DELAY, PHASE-COHERENT PULSE PAIR GENERATION FOR PRECISION RAMSEY-COMB SPECTROSCOPY **49**

4.1	Introduction	49
4.2	Setup	51
4.2.1	Overview of the experimental system	51
4.2.2	The Ti:sapphire frequency comb	53
4.2.3	Electronic synchronization scheme	54
4.2.4	The parametric amplifier	55
4.2.5	The phase-measurement setup	56
4.3	Numerical simulations of a narrowband OPCPA system	58
4.3.1	Cross- and self-phase modulation	60
4.4	Analysis of the pump pulse pair	62
4.4.1	Temporal gain shaping	62
4.4.2	Spatial gain shaping	64
4.4.3	Wavefront differences	64
4.5	Phase-measurements of the amplified frequency comb pulses	65
4.5.1	Phase shifts at different pulse delays	65
4.5.2	Phase-shift scaling with amplified pulse ratio	67
4.5.3	Spatial dependence of the phase shift	68
4.6	Conclusion	69

CHAPTER 5: RAMSEY-COMB SPECTROSCOPY WITH INTENSE ULTRASHORT LASER PULSES **71**

5.1	Introduction	71
5.2	Principle of Ramsey-comb spectroscopy	72

5.3	Overview of the experimental setup	74
5.4	Two-photon Ramsey-comb signals from rubidium and cesium	75
5.5	Methods: Further experimental details	78
5.6	Supplementary information	79
5.6.1	The atomic phase evolution	79
5.6.2	Fitting the data: Time domain versus frequency domain	80
5.6.3	Discussion of the spectroscopic results	83
CHAPTER 6: RAMSEY-COMB SPECTROSCOPY: THEORY AND SIGNAL ANALYSIS		91
6.1	Introduction	91
6.2	Analytical framework	93
6.2.1	Quantum-interference excitation with laser pulse pairs	93
6.2.2	Combining Ramsey signals from different macro delays: Ramsey-comb spectroscopy	96
6.2.3	Extension to multiple transitions	99
6.2.4	Constant phase shifts	100
6.2.5	Time-dependent phase shifts	102
6.2.6	Spectral line-broadening mechanisms	102
6.3	Fitting of the Ramsey-comb signals	103
6.3.1	Frequency-domain approach	104
6.3.2	Time-domain approach	106
6.3.3	Numerical simulations of the time-domain fitting algorithm	108
6.4	Conclusion	115
CHAPTER 7: OUTLOOK		117
7.1	Upgrades of the current system	117
7.2	Future spectroscopy targets	118
7.2.1	Molecular hydrogen	118
7.2.2	The helium ion	119
APPENDIX A: FOURIER TRANSFORMS		121
A.1	Definition of the Fourier transform	121
A.2	Lists of common Fourier transforms and relationships	122
APPENDIX B: QUANTUM INTERFERENCE EXCITATION		125
B.1	Single-pulse excitation	125

B.2 Ramsey fringes from a coherent double-pulse sequence .	128
BIBLIOGRAPHY	131
LIST OF PUBLICATIONS	143
SUMMARY	145
SAMENVATTING	149
DANKWOORD	153

CHAPTER 1

INTRODUCTION

This thesis describes a new tool for versatile, high-precision laser spectroscopy, the “Ramsey comb”. For its eventual realization, both a unique laser amplifier system for producing high-energetic coherent pulse pairs as well as the theoretical framework and analysis model had to be developed. In this introductory chapter, the broader framework and historical perspective of the Ramsey-comb method are provided: Starting from traditional Ramsey spectroscopy, we discuss the advent of optical frequency combs (FCs) and its importance for optical metrology. The need for amplification of FC lasers then leads to the novel method of Ramsey-comb spectroscopy as a powerful and easily scalable alternative to traditional direct FC spectroscopy.

1.1 Ramsey spectroscopy or the girl on the swing

As the name suggests, Ramsey-comb spectroscopy is fundamentally based on Norman Ramsey’s Nobel-prize-winning method of excitation with separated oscillating fields [1–3]. As an intuitive example, let us consider that the author would like to measure earth’s gravity with the help of his little niece Lene, who is sitting on a swing (initially at rest). Giving Lene a little push, she will start swinging back and forth at a frequency which depends (neglecting friction etc.) exclusively on the length of the swing’s rope and the gravity of earth. If after a certain time interval Lene experiences a second push, it will depend on the current position and direction of movement (i.e., the phase) of the swing, whether Lene will swing even higher or whether her maximum height will be decreased. By repeating the experiment at different time intervals between the two pushes and comparing it with how high Lene is swinging after the second

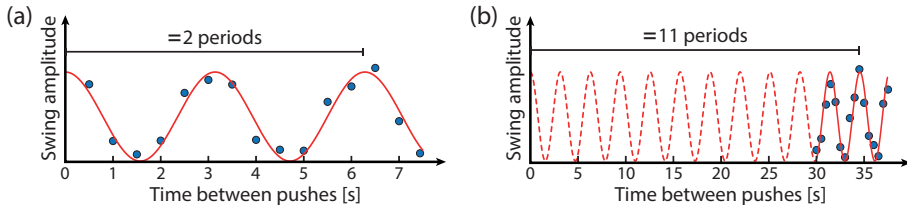


FIGURE 1.1: Schematic of possible measurement results (dots) for the maximum swing height as a function of time in between the two pushes (see text for more details). (a) 15 measurements each 0.5 seconds apart. (b) Same as in (a) but with the measurement series starting from 30 seconds after the first push.

push, we can obtain a periodic signal as sketched in Fig. 1.1(a). From this sinusoidal signal, we can then straightforwardly deduce the swinging period and hence the frequency of swinging Lene. The longer time span we cover (for the measurement in Fig. 1.1(a) only ~ 2.5 periods were recorded), the more accurate this determination will be. However, instead of recording the maximum swinging height for times close to zero, we could also measure the periodic signal at delays between the pushes of, e.g., 30.0 s, 30.5 s, 31.0 s, and so on as shown in Fig. 1.1(b). Because of the longer “lever arm” (11 periods), we can now determine the frequency more precisely than before by extrapolating back to zero time. With the help of the obtained swinging frequency, the length of the swing’s rope and some High school physics knowledge describing the motion of a pendulum we could then calculate earth’s gravity.

The girl on the swing is a greatly simplified yet instructive picture of Ramsey spectroscopy, a method developed to measure radio-frequency (RF) resonances in nuclei. In its original implementation, the two “pushes” were derived from two spatially separated microwave oscillators, a concept which also paved the way to nowadays most accurately defined physical unit, the second, based on the atomic cesium clock [4]. The initial Ramsey method was quickly extended to oscillating fields separated in time rather than in space [5] as it was actually also the case in the previous girl-on-the-swing example. This temporal version enabled the extension of Ramsey’s method to the optical domain using laser pulses [6–12]. All these pioneering optical measurements, however, missed an essential ingredient for the absolute frequency determination: Because the relative phase of the excitation pulses was unknown, the

inter-pulse delay could not be calibrated absolutely, and hence only frequency *intervals* could be measured.

1.2 Coherent pulse trains from optical frequency combs

The problem of producing laser pulses with a controlled optical phase was finally solved with the invention of the optical FC around the year 2000 by groups from JILA in Boulder [13, 14] and from the MPQ in Munich [15]. The FCs were based on Kerr-lens mode-locked Ti:sapphire oscillators, which shortly before had been introduced as suitable candidates to produce highly regular trains of optical pulses [16, 17]. While the stabilization of the inter-pulse delay had long been possible employing standard RF electronics, these groups had now additionally developed a method to measure and stabilize the optical (carrier-envelope) phase, thus effectively downcounting optical frequencies ($\sim 10^{14}$ Hz) to RF frequencies ($\sim 10^6$ - 10^9 Hz); prior to this achievement, referencing optical frequencies to RF standards had only been possible via elaborate frequency chains [18, 19]. In 2005, John L. Hall and Theodor W. Hänsch shared part of the Nobel prize in physics for pioneering this phase-stabilization method [20, 21], which will be discussed in more detail in Sec. 2.4.1.

The new possibility to produce long coherent pulse trains, or equivalently, a set of precisely calibrated optical frequencies had a strong impact on many areas of physics such as attosecond science [22], astronomy [23] but above all the field of precision spectroscopy [24], leading, e.g., to frequency measurements with up to 17 digit accuracy [25, 26]. Initially, the FC was used as an “optical ruler” to calibrate the narrowband spectroscopy lasers. However, only a few years later FC themselves were used to perform direct FC spectroscopy [27, 28], which can be regarded as an extension of the Ramsey principle with multiple, simultaneous excitations at regular time intervals. Since the FCs are typically based on pulsed oscillators [29], this enables to perform high precision spectroscopy with short (and therefore broadband) laser pulses.

1.2.1 More power for challenging spectroscopy targets

For many applications such as the spectroscopy on very weak transitions or nonlinear wavelength conversion of the typically near-infrared FCs, very high laser intensities are required, much more than what FC os-

cillators can typically deliver. In particular, high-precision spectroscopy in the (extreme) ultraviolet wavelength region has a wide range of applications such as searching for new forces beyond the standard model by measuring electronic transitions in molecules [30], testing quantum electrodynamics in He and He⁺ [31, 32], or paving the way for the next-generation “nuclear” clocks [33, 34]. Consequently, there have been substantial experimental efforts for increasing the peak power of FC laser pulses, including the amplification at full repetition rate [35, 36], amplification of a few selected pulses [37], and the employment of enhancement resonators [38, 39]. With the last two methods enough peak power has been generated for efficient high-harmonic generation of comb laser pulses to the extreme ultraviolet wavelength region. In two pioneering experiments, precision spectroscopy with a few MHz accuracy was performed at 51 nm in He using two mJ-level amplified FC pulses [31], and two years later at 82 nm in Ar using an enhancement resonator at full repetition rate [40]. However, both methods have their drawbacks: With selective amplification of two subsequent pulses only single transitions could be probed and the phase of the pulses had to be constantly monitored with high accuracy. Enhancement resonators, on the other hand, are difficult to tune over a wide wavelength range and extraction of upconverted light is rather inefficient. Therefore, we developed a universal and highly accurate novel form of Ramsey excitation, the “Ramsey comb”, which overcomes these limitations. It combines the highly successful and easily scalable concept of Ramsey spectroscopy with the referencing and tuning capabilities of FC lasers.

1.3 Less can be more: Ramsey-comb spectroscopy

The Ramsey-comb method is based on the coherent amplification of selected FC pulses. By picking only two pulses from the FC seed oscillator, much higher peak powers can be reached as opposed to full repetition rate amplification or even by employing cavity enhancement. However, if only FC pulse pairs at fixed delays can be amplified as in [31] where the selection was limited to two consecutive FC pulses, the method is limited to traditional albeit high-precision Ramsey-like spectroscopy. In particular, this means that only one isolated resonance can be recorded at a time and the frequency determination is very sensitive to phase shifts, e.g. during the amplification process. In [31], these phase shifts

thus had to be constantly monitored to correct the spectroscopic signals and together with the maximum FC pulse delay of ~ 10 ns limited the achievable accuracy.

Ramsey-comb spectroscopy circumvents these limitations by selectively amplifying FC pulses *at different pulse delays* equal to multiples of the FC repetition time. As a first consequence, this enables Ramsey-like measurements with much higher accuracy because of the increased inter-pulse delay of microseconds and more. In addition, the ability of combining a series of Ramsey signals further enhances the versatility of the selective-amplification approach. As schematically depicted in Fig. 1.2, multiple Ramsey-excitation signals can be combined to recover not only the accuracy but also the resolution of the FC seed laser, much as if the whole pulse train had been employed for the excitation. However, if more than one transition is excited simultaneously, the reconstructed spectrum will show subtle differences in the form of additional interferences that are absent in traditional direct FC spectroscopy. Fortunately, analyzing the complex multi-transition spectra is not necessary

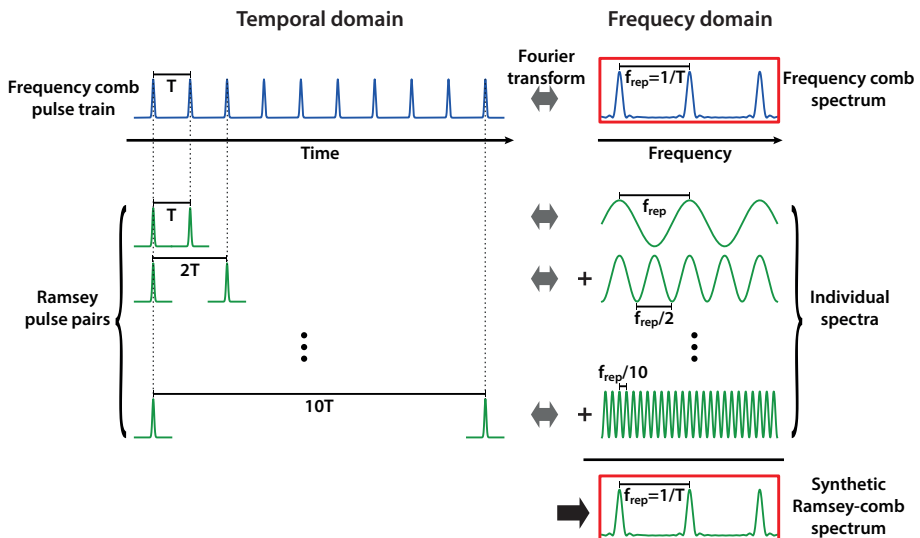


FIGURE 1.2: Comparison of direct frequency comb excitation (upper part) and Ramsey-comb excitation (lower part) when applied on a single transition; the repetition rate of the comb laser is $f_{\text{rep}} = 1/T$. On the left, the excitation pulse sequences are shown, while the corresponding spectra are sketched on the right side.

because in Ramsey-comb spectroscopy the characteristic temporal-phase evolution of the excited transitions is recorded through the individual Ramsey scans at different time delays. Based on this experimentally robust phase-evolution pattern, we developed a pure time-domain fitting method contrary to traditional spectroscopy methods that are generally based on fitting spectral line shapes in the frequency domain.

Another intriguing feature of the Ramsey-comb method is that constant phase shifts simply drop out in the analysis. This does not only include possible amplifier phase shifts (one of the limiting factors in [31]) but also other (transition-independent) phase shifts that are caused by the interaction with the excitation pulses, e.g., due to the well-known AC-Stark effect [41]. Note that the calibration of the latter one often represents a limiting factor in high-precision direct FC spectroscopy.

1.4 Short outline of this thesis

In order to efficiently discuss the experimental and conceptual aspects of Ramsey-comb spectroscopy, it is instructive to first recall some basic physical concepts. Therefore, in Ch. 2 we start by introducing the theoretical framework to describe optical pulses, coherent pulse trains and amplification of laser pulses in the contexts that are particularly relevant for this thesis.

After this introduction, the thesis continues with the description of the experimental system employed for performing Ramsey-comb spectroscopy starting with Ch. 3, which discusses the development of the double-pulse pump-laser amplifier system. The amplified pump pulses are then used to coherently amplify FC pulses in a parametric amplifier, which is the topic of Ch. 4.

Following the characterization of the experimental system, Ch. 5 contains the experimental demonstration of high-precision Ramsey-comb spectroscopy by measuring complex two-photon spectra in atomic rubidium and cesium. Along with the discussion of the spectroscopic results, the developed time-domain fitting algorithm is introduced. A comprehensive description of the analytical framework of the Ramsey-comb method then follows in Ch. 6, including numerical simulation results of the employed fitting method.

Finally, Ch. 7 provides a short outlook discussing interesting future spectroscopy targets and suggestions for potential upgrades of the experimental system.

CHAPTER 2

PRELIMINARY: ELECTROMAGNETIC WAVES, FREQUENCY COMBS AND PULSE AMPLIFICATION

In this chapter, some physical background is discussed which is of particular importance for the research carried out in the course of this thesis. For reasons of self-consistency, we start from the elementary level of Maxwell's equations but will quickly turn to more specific topics such as the description of optical pulses and pulse trains, both in the time and frequency domains. After introducing one of the core elements used in the experiments, the optical frequency comb, we will briefly discuss the amplification of laser pulses via nonlinear (parametric) interaction and in laser gain media.

2.1 Electromagnetic waves in (non)linear media

The most basic description of electromagnetic waves is derived from Maxwell's fundamental equations and has been discussed extensively in a wide range of textbooks (see, e.g., [42, 43]). Here we will restrict the derivation to propagation in the z -direction and neglect the magnetic field component, which leads to the differential equation:

$$\partial_z^2 E(z, t) - \frac{1}{c^2} \partial_t^2 E(z, t) = 0. \quad (2.1)$$

The solution to this equation are plane waves traveling with a phase velocity equal to the vacuum velocity of light c . The expression for such a wave of amplitude A , propagating in the positive z -direction is:

$$\begin{aligned} E(z, t) &= \text{Re} \left\{ 2Ae^{i(\omega t - kz)} \right\} \\ &= Ae^{i(\omega t - kz)} + c.c., \end{aligned} \quad (2.2)$$

undergoing oscillations in time at angular frequency ω and in space according to the wavenumber $k = \omega/c$. Keeping in mind that the electric field $E(z, t)$ must always be a real number, we will omit the complex conjugate (*c. c.*) during the following derivations for reasons of compactness.

When the electromagnetic radiation is surrounded by a (dielectric) medium, the induced polarization P of the medium affects the propagation and has to be included in Eq. (2.1), resulting in:

$$\partial_z^2 E(z, t) - \frac{1}{c^2} \partial_t^2 E(z, t) = \frac{1}{\epsilon_0 c^2} \partial_t^2 P(z, t), \quad (2.3)$$

where ϵ_0 is the electric permittivity of the vacuum. For a linear response to the electric field, the polarization $P(z, t)$ is described by [43]:

$$P(z, t) = \epsilon_0 \int_{-\infty}^t \chi_e(t - t') E(z, t') dt', \quad (2.4)$$

where $\chi_e(t)$ is the electric susceptibility of the medium*. The forward-propagating wave solution to Eq. (2.3) is still described by Eq. (2.2), but now the wavenumber k has become a complex function of frequency:

$$k = k(\omega) = \tilde{n}(\omega)\omega/c, \quad (2.5)$$

depending on $\tilde{n} = \sqrt{1 + \chi_e} = n + i\kappa$. The real part ($= n$) of \tilde{n} is usually referred to as the refractive index of the medium, while the imaginary part ($= \kappa$) indicates amplification or loss in the medium.

In general, however, the response of the medium is not linear in the electric field as assumed in Eq. (2.4) resulting in an intensity-dependent electric susceptibility of the medium. For an instantaneous response, we can expand the polarization in terms of electric field amplitude according to:

$$P(z, t) = \epsilon_0 \left[\chi_e^{(1)} E(z, t) + \chi_e^{(2)} E^2(z, t) + \chi_e^{(3)} E^3(z, t) + \dots \right]. \quad (2.6)$$

The nonlinear response of the medium leads to a variety of nonlinear optic effects that influence the amplitude, phase and frequency of the electromagnetic waves; comprehensive discussions of these effects can be found in range of textbooks such as [44, 45]. As an example, we consider

*In general, both the electric field and susceptibility are vector quantities, but for simplicity reasons we only investigate the situation with a polarization that is (anti-)parallel to the source field.

the leading nonlinear contribution in an isotropic medium, $\chi^{(3)}$, where by definition all even order susceptibilities are zero. In that case, the previously defined refractive index becomes [43]:

$$\tilde{n} = \sqrt{1 + \chi_e^{(1)} + \chi_e^{(3)}|E(z, t)|^2} = \tilde{n}_0 + \tilde{n}_2|E(z, t)|^2. \quad (2.7)$$

The index of refraction, $\text{Re}\{\tilde{n}\}$, is now intensity-dependent, which results in an additional nonlinear phase of the electromagnetic wave. Other important nonlinear effects include second harmonic generation and parametric amplification in the form of three wave mixing (both scaling with $\chi_e^{(2)}$), which will be discussed in more detail in Sec. 2.5. For the moment, however, we go back to the linear optics regime in order to analyze the effect of dispersion on the propagation of electromagnetic wave packets.

2.2 Pulse propagation in time and space

So far we exclusively considered the continuous-(plane-)wave solutions to Eqs. (2.1) and (2.3). However, because these equations are linear, we can write the general solution as a linear superposition of solutions with different angular frequencies:

$$E_t(z, t) = \int_{-\infty}^{\infty} A(\omega)e^{i(\omega t - kz)}d\omega = \int_{-\infty}^{\infty} A(\omega)e^{-ikz}e^{i\omega t}d\omega, \quad (2.8)$$

with $A(\omega)$ being the weighting function of the individual frequency components. Equation (2.8) is of the form $h_t(t) = \frac{1}{2\pi} \int_{-\infty}^{+\infty} h_\omega(\omega)e^{i\omega t}d\omega$, which lets us identify:

$$E_\omega(z, \omega) = \mathcal{FT}\{E_t(z, t)\} = 2\pi A(\omega)e^{-ikz} \quad (2.9)$$

as the Fourier transform of the temporal representation of the electric field $E(z, t)$ (see Appendix Ch. A). We have the flexibility to choose and quickly interchange between the time- and frequency-domain pictures via the appropriate Fourier and inverse Fourier transforms:

$$E_t(z, t) \underset{\mathcal{FT}^{-1}}{\overset{\mathcal{FT}}{=}} E_\omega(\omega, t). \quad (2.10)$$

Having these two equivalent representations greatly simplifies the analysis of various physical effects, which are typically much more straightforwardly treated in one out of the two domains, frequency or time. For the

convenience of the reader, the Appendix Ch. A provides two tables with common Fourier transforms (Tab. A.1) and related theorems (Tab. A.2) that have been applied in this thesis.

We make immediate use of the Fourier properties for analyzing the influence of linear material dispersion on the spatial propagation of an electromagnetic pulse. At $z = 0$, the pulse is conveniently represented in terms of a carrier frequency ω_0 and an envelope function $\mathcal{E}_t(0, t)$:

$$E_t(0, t) = \mathcal{E}_t(0, t)e^{i\omega_0 t}, \quad (2.11a)$$

$$E_\omega(0, \omega) = \mathcal{E}_\omega(0, \omega - \omega_0). \quad (2.11b)$$

In frequency domain, the decoupling of the carrier frequency simply leads to a shift of the spectral envelope $\mathcal{E}_\omega(0, \omega)$ as schematically depicted in Fig. 2.1.

Propagation (in positive z -direction) of these initial envelopes is most conveniently accounted for in the frequency domain:

$$\mathcal{E}_\omega(z, \omega) = \mathcal{E}_\omega(0, \omega)e^{-ikz}. \quad (2.12)$$

We use an inverse Fourier transform to subsequently convert to the time domain:

$$E_t(z, t) = \frac{1}{2\pi} \int_{-\infty}^{+\infty} \mathcal{E}_\omega(0, \omega - \omega_0)e^{-ikz} e^{i\omega t} d\omega. \quad (2.13)$$

If we then expand the wave number around $\omega = \omega_0$:

$$k(\omega) = k_0 + k^{(1)}(\omega - \omega_0) + \frac{1}{2}k^{(2)}(\omega - \omega_0)^2 + \dots, \quad (2.14)$$

we can rewrite Eq. (2.13) as:

$$E_t(z, t) = e^{i(\omega_0 t - k_0 z)} \mathcal{E}_t(z, t), \quad (2.15)$$

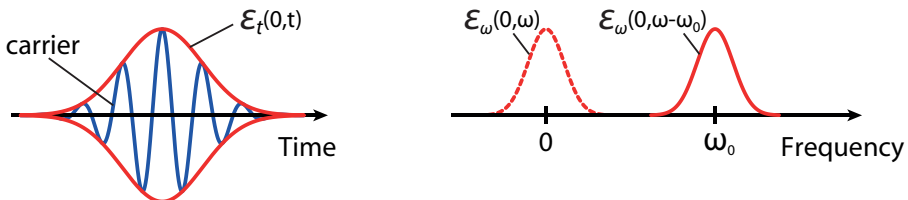


FIGURE 2.1: Visualization of the concept of temporal and spectral envelopes (\mathcal{E}_t and \mathcal{E}_ω , respectively), which are connected to each other by a Fourier transform.

with:

$$\mathcal{E}_t(z, t) = \frac{1}{2\pi} \int_{-\infty}^{+\infty} \mathcal{E}_\omega(0, \omega - \omega_0) e^{i[(\omega - \omega_0)t - (k - k_0)z]} d\omega. \quad (2.16)$$

2.2.1 Carrier-envelope phase and group velocity dispersion

If we limit the expansion of k to its first order (see Eq. (2.14)), the evaluation of the integral in Eq. (2.16) results in:

$$\begin{aligned} \mathcal{E}_t(z, t) &= \frac{1}{2\pi} \int_{-\infty}^{+\infty} \mathcal{E}_\omega(0, \omega - \omega_0) e^{i(\omega - \omega_0)(t - k^{(1)}z)} d\omega \\ &= \mathcal{E}_t(0, t - k^{(1)}z). \end{aligned} \quad (2.17)$$

We see that while the overall shape remains constant, the temporal envelope now travels at the group velocity $v_g = 1/k^{(1)}$. Since v_g is in general not equal to the phase velocity $v_p = \omega_0/k_0$, this results in a propagation-dependent phase offset between carrier and envelope. This so-called carrier-envelope phase shift will be of particular importance when discussing frequency comb lasers in Sec. 2.4.

The situation changes considerably if we include the quadratic term in the expansion of the wave vector in Eq. (2.14). The temporal envelope following from Eq. (2.16) then becomes:

$$\mathcal{E}_t(z, t) = \frac{1}{2\pi} \int_{-\infty}^{+\infty} \mathcal{E}_\omega(0, \omega - \omega_0) e^{i(\omega - \omega_0)[t - k^{(1)}z - k^{(2)}z(\omega - \omega_0)/2]} d\omega. \quad (2.18)$$

We see that the inclusion of the quadratic term leads to a frequency-dependent group velocity $v_g(\omega) = 1/[k^{(1)} + k^{(2)}(\omega - \omega_0)/2]$, which causes the temporal envelope to broaden during propagation due to the spread of the individual frequency components. This effect is usually referred to as group velocity dispersion and while often undesirable can also be employed to tailor pulse durations as we will see in the following section.

2.2.2 A practical example: Temporal broadening of a Gaussian pulse

It is instructive to apply the developed concepts to an analytically convenient and hence popular textbook example, the Gaussian pulse:

$$\mathcal{E}_t(0, t) = e^{-\frac{1}{2}\left(\frac{t}{\tau_p}\right)^2}, \quad (2.19a)$$

$$\mathcal{E}_\omega(0, \omega) = \tau_p \sqrt{2\pi} e^{-\frac{1}{2}(\omega\tau_p)^2}. \quad (2.19b)$$

One conclusion directly apparent from Eq. (2.19) is that the temporal width of the pulse ($\propto \tau_p$) is inversely proportional to the width of the frequency-domain envelope ($\propto 1/\tau_p$). This inverse scaling provides the important general insight that a short pulse requires a broad spectrum. We will now analyze two temporal pulse broadening effects.

First, we derive the temporal envelope of an initial Gaussian pulse which is spectrally clipped. In the experiments, this is applied to adjust the pulse lengths from the output of the pump oscillator (see Sec. 3.1). Analytically, the clipping is described by multiplying the spectral envelope $\mathcal{E}_\omega(0, \omega)$ with a window function, $\text{rect}(\omega/\Delta\omega)$ that is 1 for $|\omega| < \frac{\Delta\omega}{2}$ and 0 otherwise. The Fourier pair of the initially Gaussian envelopes then reads:

$$\mathcal{E}_t(0, t) \star \left[\frac{\Delta\omega}{2\pi} \text{sinc}\left(t \frac{\Delta\omega}{2\pi}\right) \right] \Leftrightarrow \mathcal{E}_\omega(0, \omega) \cdot \text{rect}\left(\frac{\omega}{\Delta\omega}\right); \quad (2.20)$$

the multiplication in the frequency domain translates into a convolution in the time domain. Figure 2.2 illustrates the spectral clipping process by showing the spectral and temporal envelopes before and after a spectral gate has been applied. It can be seen that apart from the anticipated temporal broadening because of the reduced spectral bandwidth, the spectral convolution with a sinc-function results in pre- and after-pulses in the time domain.

Another influence that can cause the pulse to broaden in time is group velocity dispersion as discussed in Sec. 2.2.1. Starting again with the temporal envelope as defined in Eq. (2.19a), the integral in Eq. (2.18) evaluates to:

$$\mathcal{E}_t(z, t) = \frac{\tau_p}{\sqrt{\tau_p + ik^{(2)}z}} e^{-\frac{(t-k^{(1)}z)^2}{2(\tau_p^2 + ik^{(2)}z)}}. \quad (2.21)$$

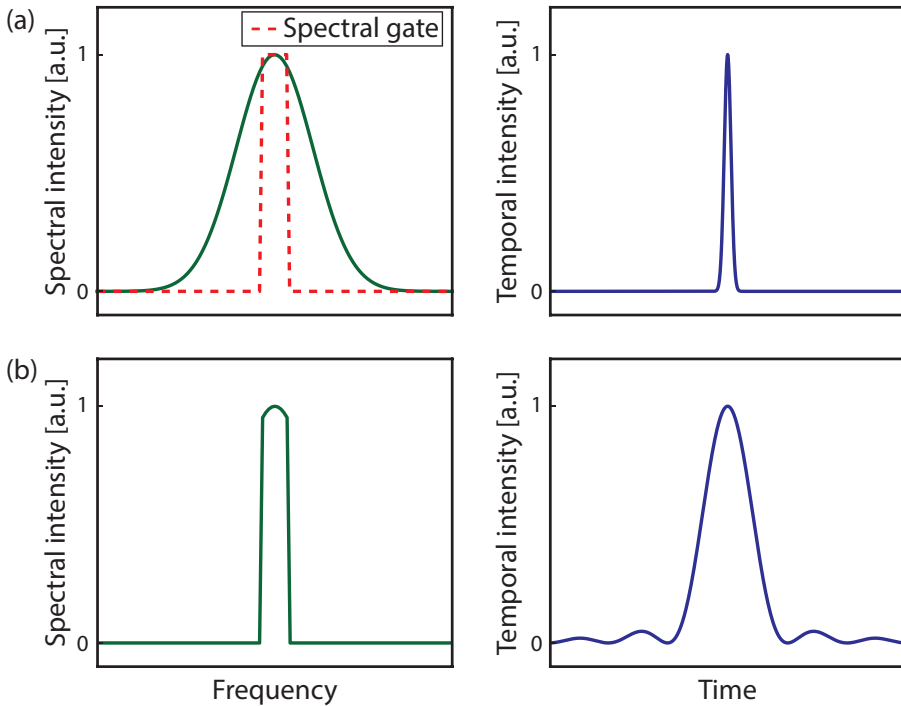


FIGURE 2.2: Simulation of the effect of spectral clipping. (a) Initial spectral and temporal envelopes of a Gaussian pulse. (b) Envelopes after the spectral clipping with the spectral gate indicated by the dashed line in (a).

From the real part of this expression we can derive the new pulse duration:

$$\tau_p'(z) = \tau_p \sqrt{1 + (k^{(2)}z/\tau_p)^2}, \quad (2.22)$$

which describes the increase in duration from its initial value τ_p due to the accumulated dispersion $k^{(2)}z$. Note that in the spectral domain, the dispersion only acts on the spectral phase:

$$\mathcal{E}_\omega(z, \omega) = \mathcal{E}_\omega(0, \omega) e^{-i[k_0 + k^{(1)}(\omega - \omega_0) + \frac{1}{2}k^{(2)}(\omega - \omega_0)^2]z} \quad (2.23)$$

but does not affect the spectral intensity, which is proportional to the absolute value of $\mathcal{E}_\omega(z, \omega)$.

2.3 Pulse pairs and pulse trains

Based on the previously developed framework for describing electromagnetic wave packets (light pulses), we will now discuss trains of N pulses, regularly spaced in time and equal in amplitude. With the shorthands $\mathcal{E}_t(t) = \mathcal{E}_t(0, t)$ and $\mathcal{E}_\omega(\omega) = \mathcal{E}_\omega(0, \omega)$ for the temporal and spectral envelopes of one individual pulse, respectively, and an inter-pulse delay of T we have:

$$\mathcal{E}_t^N(t) = \mathcal{E}_t(t) \star \sum_{n=0}^{N-1} \delta(t - nT), \quad (2.24a)$$

$$\mathcal{E}_\omega^N(\omega) = \mathcal{E}_\omega(\omega) \cdot \sum_{n=0}^{N-1} e^{-in\omega T}. \quad (2.24b)$$

The spectrum I_ω can be written in the more intuitive form of:

$$\begin{aligned} I_\omega(\omega) &\propto |\mathcal{E}_\omega^N(\omega)|^2 \\ &= |\mathcal{E}_\omega(\omega)|^2 \cdot \underbrace{|e^{in\omega T}|^2}_{=1} \left| \sum_{n=1}^N e^{-in\omega T} \right|^2 \\ &= |\mathcal{E}_\omega(\omega)|^2 \cdot (e^{-i\omega T} + \dots + e^{-iN\omega T}) \cdot (e^{+i\omega T} + \dots + e^{+iN\omega T}) \\ &= |\mathcal{E}_\omega(\omega)|^2 \cdot \sum_{n=1}^N [2(N - n)\cos(nT\omega) + 1], \end{aligned} \quad (2.25)$$

where in the last step we expanded the two terms in brackets and sorted out the pre-factors of the cosines ($\cos(x) = e^{-ix}/2 + e^{ix}/2$) of different harmonic orders. From Eq. (2.25) we see that apart from the single-pulse spectral envelope $|\mathcal{E}_\omega(\omega)|^2$, the spectrum comprises an additional substructure based on the superposition of cosines with spectral periods of $n\omega_{rep} = n2\pi/T$. In the case of $N = 2$, this simply leads to a cosine-modulated spectrum as shown in Fig. 2.3(a,b) for different inter-pulse delays. For $N > 2$, the superposition of the different harmonics causes a characteristic spectral interference pattern with $N - 2$ side maxima in between the main peaks (Fig. 2.3(c)).

In the limit of $N \rightarrow \infty$ (i.e., an infinite train of pulses), the Fourier transform of the time-domain comb function in Eq. (2.24a) is a comb function in the frequency domain. Hence the substructure of the spec-

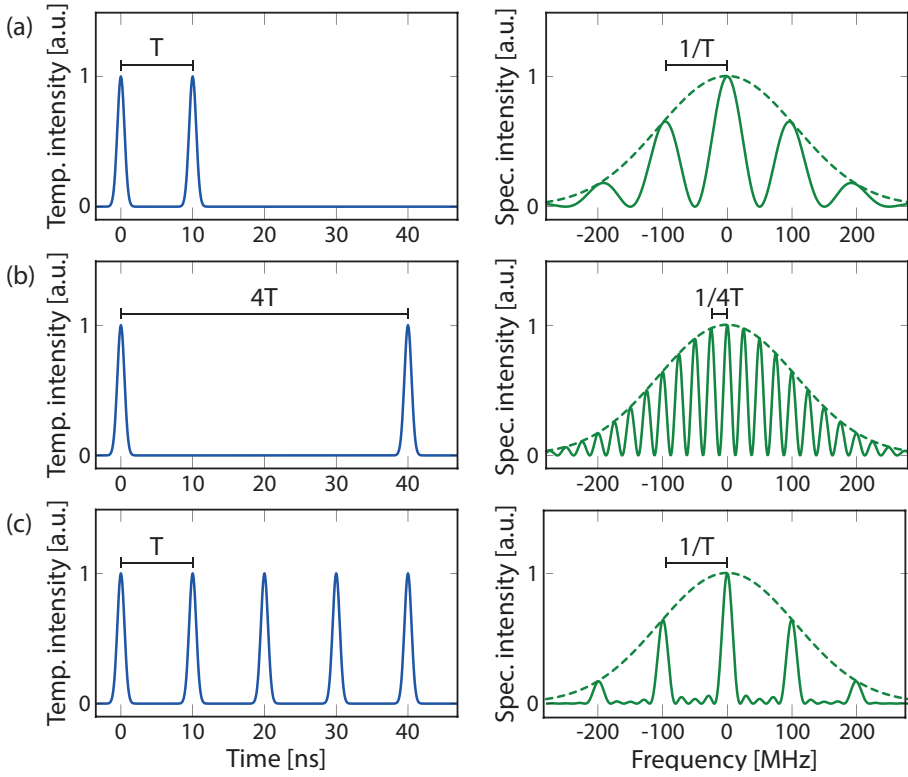


FIGURE 2.3: Temporal (left column) and spectral (right column) intensities for different pulse sequences. (a, b) Pulse pairs of different temporal spacings. (c) Pulse train of five regularly spaced pulses. While the shape of the overall spectral envelope (dashed line) remains constant, the spectral substructure changes according to the number and spacings of the pulses.

trum:

$$I_{\omega}(\omega) \propto |\mathcal{E}_{\omega}(\omega)|^2 \cdot \left| \sum_{n=0}^{\infty} \delta\left(\omega - \frac{n2\pi}{T}\right) \right|^2 \quad (2.26)$$

then also consists of a series of (theoretically) infinitesimal narrow peaks. However, this is not yet sufficient to realize what is conventionally called a frequency comb as we will see in the next section.

2.4 Frequency combs

Because in general the group and phase velocities of the light pulses are different due to dispersion, the carrier of the electromagnetic wave will acquire a phase shift relative to the temporal envelope (cf. Sec. 2.2.1). If this carrier-envelope phase shift ϕ_{ceo} is constant from pulse to pulse, we can incorporate ϕ_{ceo} in Eq. (2.24) as follows:

$$\mathcal{E}_t^N(t) = \mathcal{E}_t(t) \star \sum_{n=0}^{N-1} \delta(t - nT) e^{-in\phi_{ceo}}, \quad (2.27a)$$

$$\begin{aligned} \mathcal{E}_\omega^N(\omega) &= \mathcal{E}_\omega(\omega) \cdot \sum_{n=0}^{N-1} e^{-in(\omega T + \phi_{ceo})} \\ &= \mathcal{E}_\omega(\omega) \cdot \sum_{n=0}^{N-1} e^{-inT(\omega + \frac{\phi_{ceo}}{T})}. \end{aligned} \quad (2.27b)$$

The carrier-envelope phase shift thus causes a frequency shift of the spectral substructure of:

$$f_{ceo} = \frac{\omega_{ceo}}{2\pi} = \frac{\phi_{ceo}}{2\pi T}. \quad (2.28)$$

We swapped from angular frequencies to regular frequencies ($\omega = 2\pi f$) for reasons of convention and will continue so for the majority of this thesis. The carrier-envelope phase shift as well as its influence on the spectral substructure are schematically depicted in Fig. 2.4. For obvious reasons, the spectral features are usually referred to as "comb modes". With the repetition rate $f_{rep} = 1/T$, the expression for the " m^{th} " comb mode is:

$$f_m = f_{ceo} + m f_{rep}. \quad (2.29)$$

The spectral position of the comb lines is, therefore, fully determined by the pulse-to-pulse spacing $T = 1/f_{rep}$ and the carrier-envelope phase shift via f_{ceo} according to Eq. (2.28). In the next section we will discuss how these two parameters can be controlled in practice in order to create an optical ruler with precisely calibrated frequencies, an optical frequency comb.

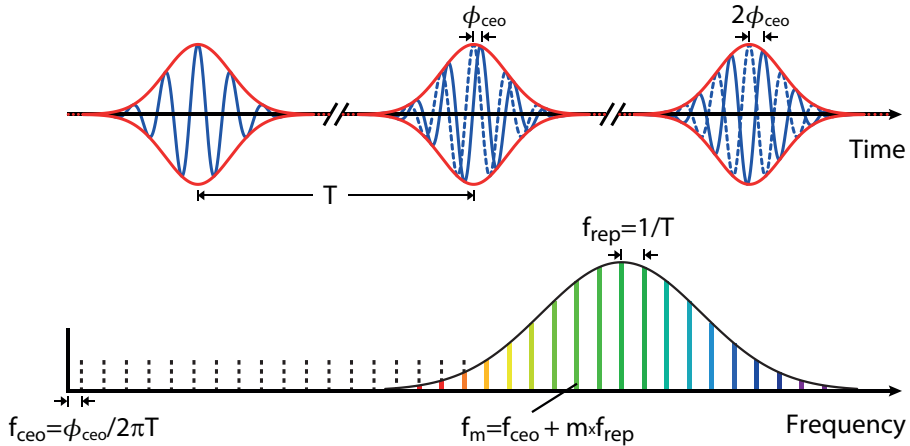


FIGURE 2.4: An infinite, coherent train of optical pulses spaced by a delay time T (upper part) is equivalent to a spectrum of equidistant infinitesimal narrow comb modes (lower part). A potential pulse-to-pulse phase shift ϕ_{ceo} transforms into the carrier-envelope offset frequency f_{ceo} .

2.4.1 On the technical realization of optical frequency combs

The prerequisite for an optical frequency comb is a regular train of short optical pulses, which are routinely produced by mode-locked laser oscillators (see, e.g., [46, 47]). For typical resonator lengths of about 1 m, the repetition rate of the emitted pulse train is in the order of 100 MHz and can be measured with a standard photodiode. Furthermore, f_{rep} can be compared to a local radio-frequency (RF) oscillator and straightforwardly be stabilized via feedback on the resonator length.

However, fixing the second parameter of the comb Eq. (2.29), i.e., the carrier-envelope frequency f_{ceo} , had not been possible for a long time. Because the optical carrier frequency is extremely high (in the order of 500 THz) as compared to convenient RF frequencies, a direct measurement with, e.g., a photodiode is far out of reach. Fortunately, this problem has been solved by the technique of self-referencing [14, 15]. In the standard “ f - $2f$ ”-implementation, the low frequency part of the pulse spectrum is upconverted via sum-frequency-mixing (SFM):

$$f_m = m f_{rep} + f_{ceo} \xrightarrow[SFM]{} f_{m'} = m' f_{rep} + 2 f_{ceo}. \quad (2.30)$$

The upconverted light is then mixed with the high frequency part of the spectrum by combining them on a single photodiode. The resulting beat

signal will contain the difference frequency:

$$\begin{aligned} f_{beat} &= (2f_{ceo} + m'f_{rep}) - (f_{ceo} + mf_{rep}) \\ &= f_{ceo} + (m' - m)f_{rep}. \end{aligned} \quad (2.31)$$

If the pulse spectrum covers a full octave, $(m' - m) = 0, 1, 2, \dots$ and the signal will contain the carrier-envelope frequency $f_{ceo} \leq f_{rep}$. By the use of appropriate low-pass filters one can isolate f_{ceo} and compare it to a local (RF) oscillator similar to referencing the repetition rate f_{rep} . Feedback on f_{ceo} is possible via different means but most commonly done via small changes of the intra-cavity intensity, e.g., by modulating the pump laser power. The slight change of the intra-cavity laser pulse intensity induces a change of the nonlinear refractive index according to Eq. (2.7), which affects the phase and group velocity of the pulse by different amounts and thus induces a change of f_{ceo} .

Although octave spanning spectra directly from the oscillator have been demonstrated [48] and are nowadays even commercially available, such a broadband operation is technically challenging as it requires a carefully tuned intra-cavity dispersion. Still the most common approach for getting sufficient spectral coverage is to employ nonlinear effects such as self-phase modulation and frequency mixing to spectrally broaden the oscillator output. This is possible because mode-locked lasers can straightforwardly produce ultrashort pulses $\ll 1$ ps, enabling high pulse intensities to efficiently drive these nonlinear processes. However, in bulk nonlinear materials such short pulses typically broaden very quickly due to material dispersion. The advent of group velocity-tailored micro-structured photonic fibers [49–51] solved this problem. Using these fibers, the peak intensity of the laser pulses can be maintained over sufficient interaction lengths to perform the required spectral broadening. With this tool, the first fully stabilized optical frequency combs were realized simultaneously in the groups of John L. Hall [14] and Theodor W. Hänsch [15], who were awarded part of the 2005 Nobel prize in physics for their pioneering work [20, 21].

2.5 Phase-coherent optical parametric amplification

In this section we discuss in more detail one particular nonlinear effect, optical parametric amplification (OPA). The technique of OPA is particularly interesting for the amplification of frequency comb pulses as it

has been shown that the temporal coherence of the seed pulses can be preserved during the amplification process [52–55].

The basic principle of OPA is simple: A high-intensity, high-frequency *pump* beam (angular frequency ω_p) amplifies a lower-frequency *signal* beam (ω_s). During the amplification process, a third so-called *idler* beam (ω_i) is created that satisfies energy conservation together with the two other beams:

$$\omega_p = \omega_s + \omega_i. \quad (2.32)$$

This conversion of photons of different frequencies is based on the combined nonlinear response of pump, signal and idler beam in a nonlinear medium (with a nonzero $\chi_e^{(2)}$, cf. Sec. 2.1). For example, the pump and signal beam will induce a combined nonlinear polarization according to (see, e.g., [56], assuming an instantaneous process and limiting ourselves to one spatial coordinate):

$$P = \epsilon_0 \chi_e^{(2)} E_p(z, t) E_s^*(z, t). \quad (2.33)$$

Taking into account the different contributions, the full (temporal) pulse propagation of the envelopes of pump, signal and idler beams can be described by a set of coupled-wave equations (see, e.g., [57, 58]; we temporarily refrain from the use of the subscript “ t ” for the temporal envelope for reasons of readability):

$$\partial_z \mathcal{E}_s + \sum_{n=1}^{\infty} \frac{(-i)^{n+1}}{n!} k^{(n)} \partial_t^n \mathcal{E}_s = -i \chi_e^{(2)} \frac{\omega_s}{2n_s c} \mathcal{E}_p \mathcal{E}_i^* e^{-iz\Delta k}, \quad (2.34a)$$

$$\partial_z \mathcal{E}_i + \sum_{n=1}^{\infty} \frac{(-i)^{n+1}}{n!} k^{(n)} \partial_t^n \mathcal{E}_i = -i \chi_e^{(2)} \frac{\omega_i}{2n_i c} \mathcal{E}_p \mathcal{E}_s^* e^{-iz\Delta k}, \quad (2.34b)$$

$$\partial_z \mathcal{E}_p + \sum_{n=1}^{\infty} \frac{(-i)^{n+1}}{n!} k^{(n)} \partial_t^n \mathcal{E}_p = -i \chi_e^{(2)} \frac{\omega_p}{2n_p c} \mathcal{E}_s \mathcal{E}_i^* e^{iz\Delta k}. \quad (2.34c)$$

Here the so-called slowly-varying envelope approximation ($\partial_z \mathcal{E} \ll 2k \partial_z \mathcal{E}$) was used and we introduced the wave-vector mismatch

$$\Delta k = |\Delta \mathbf{k}| = |\mathbf{k}_p - \mathbf{k}_s - \mathbf{k}_i|; \quad (2.35)$$

in the ideal case, the nonlinear amplification process is perfectly phase-matched and hence $\Delta k = 0$. A complete analytical treatment of the coupled equations is mathematically challenging, but we can derive an

insightful expression for the small signal gain (i.e., the pump intensity $I_p \propto |\mathcal{E}_p|^2$ is assumed to be constant) under certain assumptions: If we neglect dispersion (the temporal derivations in Eq. (2.34)) and assume the initial absence of an idler beam, the signal intensity after travelling through a nonlinear medium of length L can be written as [57]:

$$I_{out} = I_{in} \cosh^2(gL) \quad (2.36)$$

with I_{in} being the initial intensity of the seed beam and:

$$g = \sqrt{\frac{\left(\chi_e^{(2)}\right)^2 \omega_s \omega_i}{2\epsilon_0 c^3 n_p n_s n_i} I_p - \left(\frac{\Delta k}{2}\right)^2}. \quad (2.37)$$

In the large gain approximation ($gL \gg 1$), the small signal gain factor $G_0 = I_{out}/I_{in}$ is:

$$G_0 \approx \frac{1}{4} e^{2gL}. \quad (2.38)$$

Because of the exponential scaling, gains in the order of 10^4 can be reached for pump intensities of a few GW/cm^2 and a few mm propagation in a nonlinear crystal with a high $\chi_e^{(2)}$ such as β -BaB₂O₄ (BBO).

In general, Δk is nonzero because of material dispersion, and the gain is reduced according to Eq. (2.37). However, by exploiting the birefringence of BBO and introducing a small finite angle between signal and pump beam, one can minimize Δk . By using this non-collinear optical parametric (NOPA) scheme, a bandwidth of a few hundred nanometers can be efficiently phase-matched [59].

In addition to limiting the achievable gain in the parametric amplification process, Δk also has a direct influence on the phase of the amplified signal beam. This is of particular importance when OPA is employed for amplifying frequency comb pulses as performed in this thesis. If we again neglect dispersion and rewrite the pulse envelopes in a polar form according to $\mathcal{E}_m(z, t) = \rho_m(z, t) e^{-i\phi_m(z, t)}$ ($m = s, p, i$), we can obtain the following coupled equations governing the phase evolution during the OPA process from the imaginary part of Eq. (2.34) [59]:

$$\partial_z \phi_s = -\chi_e^{(2)} \frac{\omega_s}{2n_s c} \frac{\rho_i \rho_p}{\rho_s} \cos(\zeta), \quad (2.39a)$$

$$\partial_z \phi_i = -\chi_e^{(2)} \frac{\omega_i}{2n_i c} \frac{\rho_s \rho_p}{\rho_i} \cos(\zeta), \quad (2.39b)$$

$$\partial_z \phi_p = -\chi_e^{(2)} \frac{\omega_p}{2n_p c} \frac{\rho_s \rho_i}{\rho_p} \cos(\zeta), \quad (2.39c)$$

with $\zeta = \Delta kz + \phi_p - \phi_s - \phi_i$. These equations can straightforwardly be solved by assuming an initially zero idler field and using the Manley-Rowe relation [59, 60]:

$$\phi_s = \phi_s(0) - \frac{\Delta k}{2} \int_0^L \frac{f_D}{f_D + \gamma^2} dz, \quad (2.40a)$$

$$\phi_i = \phi_p(0) - \phi_s(0) + \frac{\pi}{2} - \frac{L\Delta k}{2}, \quad (2.40b)$$

$$\phi_p = \phi_p(0) - \frac{\Delta k}{2} \int_0^L \frac{f_D}{1 - f_D} dz, \quad (2.40c)$$

where we introduced $\gamma^2 = \frac{\omega_p I_s(0)}{\omega_s I_p(0)}$ and the fractional pump depletion:

$$f_D = 1 - \frac{I_p(z)}{I_p(0)}. \quad (2.41)$$

A number of interesting conclusions can be drawn from Eq. (2.40). First of all, the phase of the signal pulse is independent of the phase of the pump pulse. In particular, this means that a coherent amplification of frequency comb pulses via OPA does not require a coherent pump pulse pair. However, what does influence the signal phase is the pump intensity via the fractional pump depletion f_D . Depending on the pump depletion level and thus depending on the propagated distance in the nonlinear crystal, the signal phase undergoes a phase shift proportional to the wave-vector mismatch Δk . Further discussion and quantization of the signal phase shifts cover a main part of Ch. 4 in this thesis.

Note that in order to obtain the analytical results for both the OPA gain and OPA phase influence, the dispersion terms in Eq. (2.34) were neglected. While there is no general analytical solution to the complete set of equations, further insight can be gained via numerical solutions which is discussed in the following section.

2.5.1 Numerical solutions to the coupled-wave equations

Most of the complexity of the time-domain Eq. (2.34) arises from the complicated dispersion terms $\sum_{n=1}^{\infty} \frac{(-i)^{n+1}}{n!} k^{(n)} \partial_t^n$. In the frequency domain, however, the dispersion simply manifests itself in the form of a spectral phase shift of $kz = n(\omega) \frac{\omega}{c}$ according to Eq. (2.12). Because the remaining part of Eq. (2.34) is preferably calculated in the time domain, this suggests the use of a Split-Step Fourier approach that changes

back and forth between the time and frequency domains with the use of Fourier transforms: First, the total crystal length L is divided into a number of subsections of length δL . For each section, one calculates *subsequently* either the accumulated dispersion in the *frequency domain* or the nonlinear interaction (the influence of the nonlinear polarization induced by the fields) in the *time domain*. For the time-domain step, this requires the simultaneous integration of the coupled integral equations, which can be done by employing a fourth-order Runge-Kutta integration routine [61]. If the number of sections $L/\delta L$ is chosen sufficiently large (which can be cross-checked by further increasing $L/\delta L$ without causing significant changes of the result), this step-by-step algorithm provides a good approximation to the analytical problem.

For this thesis, a program written by S. Witte [58] in Python [62] was adapted to model the parameters of the experimental setup. The results, in particular the influence of certain experimental parameters onto the amplified signal phase, are discussed in detail in the context of the experimental phase measurements of the amplified frequency comb pulses in Ch. 4.

2.6 Amplification in laser gain media

In the previous section, we discussed the physics of optical parametric amplification (OPA), which can be employed to phase-coherently amplify optical frequency combs. In order to drive the OPA process, high-energy pump pulses are required that need to be created via amplification in a laser amplifier. Therefore, we first briefly review the physical processes describing the amplification of a short (<1 ns) laser pulse as can be found in various textbooks (see, e.g., [46, 47, 63]). Subsequently, we apply the basic theory to the special case of grazing-incidence amplifiers, which are employed in the pre-amplifier for the laser system described in Ch. 3.

2.6.1 Gain and saturation in short-pulse amplification

In a four-level system, as it is, e.g., the case for the Nd-doped laser amplifier media used in the experimental setup, the change in the population inversion n due to a pulse of a certain photon density ξ (number of photons per volume) is [63]:

$$\partial_t n = -nc\sigma_e \xi, \quad (2.42)$$

where σ_e is the emission cross section of the laser medium and c is the speed of light. Thanks to the stimulated emission, ξ increases while travelling in the amplifier proportional to $cn\sigma_e\xi$. To calculate the net change in photon density, we have to subtract the photons flowing out of the considered amplifier region (while the pulse is travelling in positive z -direction):

$$\partial_t \xi = cn\sigma_e \xi - c\partial_z \xi. \quad (2.43)$$

This time-dependent transport equation can be solved for various types of input pulse shapes. For a square pulse of duration τ_p and an initial photon density ξ_0 , the solution as presented by Frantz and Nodvik is [64]:

$$\frac{\xi(z, t)}{\xi_0} = \frac{1}{1 - (1 - e^{-\sigma_e n z}) e^{-\sigma_e \xi_0 c(t-z/c)}}. \quad (2.44)$$

We can rewrite this equation with the help of more intuitive laser parameters: the fluence of the input (seed) laser pulse $F_{in} = c\tau_p\xi_0 h f_L$ and the saturation level of the medium $F_{sat} = h f_L / \sigma_e$; f_L is the frequency of the laser transition and h is Planck's constant. Writing further the small signal gain factor of a laser medium of length L as $G_0 = e^{n\sigma_e L}$, the amplifier gain G is obtained from Eq. (2.44) as [63]:

$$G = \frac{F_{sat}}{F_{in}} \ln \left[1 + \left(e^{F_{in}/F_{sat}} - 1 \right) G_0 \right], \quad (2.45)$$

from which the signal fluence after the amplifier can be calculated as $F_{out} = F_{in} G$. Equation (2.45) describes the gain from the laser medium including saturation effects, which become significant when the amplified signal fluence gets comparable to the saturation fluence of the medium, F_{sat} . In the case of low seed fluence ($G_0 F_{in} / F_{sat} \ll 1$), the gain depends exponentially on the amplifier length:

$$G \approx G_0 = e^{n\sigma_e L}, \quad (2.46)$$

while in the case of strong saturation ($F_{in} / F_{sat} \gg 1$) a linear dependence can be found:

$$G \approx 1 + F_{sat} / F_{in} n \sigma_e L. \quad (2.47)$$

Saturating the amplifier obviously results in a lower gain. This regime is nevertheless desirable for efficient energy extraction, i.e., converting

the majority of stored pump energy into signal pulse energy. In addition, a saturated amplifier also helps to reduce energy fluctuations of the amplified signal pulse energy. As shown in [43], this can be seen by differentiating $F_{out} = GF_{in}$ with respect to F_{in} and relating the relative fluctuations of the output ($\Delta F_{out}/F_{out}$) and input fluences ($\Delta F_{in}/F_{in}$) to define the damping factor:

$$D_F = \frac{\Delta F_{out}/F_{out}}{\Delta F_{in}/F_{in}} = \frac{G_0 e^{F_{in}/F_{sat}}}{1 + (e^{F_{in}/F_{out}} - 1) G_0} \cdot \frac{1}{G}. \quad (2.48)$$

In the case of strong saturation, $D_F \approx 1/G$ and hence the stability of the amplified pulse energy is enhanced accordingly. While the extraction efficiency and the stability benefit from operating the amplifier in the saturation regime, there are a range of other, less desired effects such as spectral and temporal gain shaping, which will be discussed in Ch. 3 together with the technical description of the amplifier system.

2.6.2 Grazing-incidence amplifiers

A special type of laser amplifiers are grazing-incidence (“bounce”) amplifiers, pioneered by Alcock et al. [65]. Because of their potential high gain, bounce amplifiers can be set up in compact single- or double-pass configurations enabling short optical paths in the amplifier. As opposed to regenerative or multipass amplifiers, which often exhibit long internal path lengths, this allows the amplification of short pulse sequences without interference of the pulses within the amplifier. This feature makes bounce amplifiers particularly attractive for Ramsey-comb spectroscopy, which requires equally amplified pulse sequences at variable delays. The geometry of such an amplifier is schematically depicted in Fig. 2.5(a). As the name suggests, the signal beam travels in the crystal under a shallow angle and undergoes a total internal reflection halfway on its path through the crystal. This geometry has two main advantages. First, the signal beam can travel very close to the side of the crystal facing the pump beam as seen in Fig. 2.5(a). Second, the effective gain in the plane of the pump and signal beams is averaged over the inhomogeneous pumping region caused by the one-sided pumping scheme. In order to gain further insights of the amplification process for this particular geometry, we introduce an analytic model based on the work of Agnesi et al. [66] to calculate the gain coefficient G .

The mathematical model is considerably simplified by making use of a local coordinate system (a, b) as defined in Fig. 2.5(b); for small

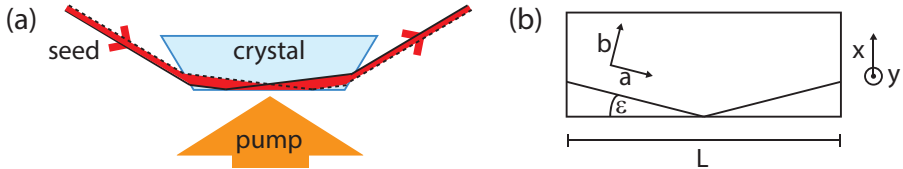


FIGURE 2.5: (a) Schematic of the side-pumped, grazing-incidence “bounce” amplifier geometry. (b) Sketch of the different coordinate systems used to model the propagation in the amplifier.

grazing angles, $\tan(\epsilon) \approx \epsilon$, and the x -coordinate can be expressed as $x(a, b) = \epsilon L/2 - a\epsilon + b$. In order to calculate the signal intensity after the amplifier I_{out} (the output fluence divided by its pulse duration, assuming a square pulse shape) analogously to Eq. (2.42), we write the population inversion density as:

$$n(x, y) = \frac{W_p(x, y)\tau}{1 + I_s(b, y)/I_{sat}}, \quad (2.49)$$

with the lifetime of the upper laser state τ , the saturation intensity $I_{sat} = F_{sat}/\tau$, and the pump rate:

$$W_p(x, y) = \eta \frac{\alpha_p}{HL} \frac{P e^{-\alpha_p x}}{h f_L} \Theta_H(y). \quad (2.50)$$

The pump rate is assumed to be constant in the vertical direction over the pump sheet of length L and height H ($\Theta_H(y) = 1$ for $|y| < H/2$, and 0 otherwise), and depends on the absorbed pump power P , the quantum efficiency $\eta = f_L/f_p$ (f_p is the center frequency of the pump light) and the saturated absorption coefficient:

$$\alpha_p = \frac{\alpha_{p,0}}{1 + I_p/I_{p,sat}}, \quad (2.51)$$

which in turn depends on the incident pump pulse intensity $I_p = P/(HL)$ and the pump pulse saturation intensity $I_{p,sat} = h f_p/(\sigma_a \tau)$; σ_a is the absorption cross section of the laser medium at f_p . We can calculate the amplifier gain from solving the differential propagation equation:

$$\partial_b I_{out}(b, y) = \sigma_e n(x, y) I_{out}(b, y) \quad (2.52)$$

to obtain [66]:

$$\ln \left[\frac{I_{out}(b, y)}{I_{in}(b, y)} \right] + \frac{I_{out}(b, y) - I_{in}(b, y)}{I_{sat}} = \eta \frac{\alpha_p P}{HL I_{sat}} \rho(b) \quad (2.53)$$

with:

$$\rho(b) = \frac{2}{\epsilon\alpha_p} \left[1 - \cosh(b\alpha_p) e^{-\alpha_p\epsilon L/2} \right]. \quad (2.54)$$

To further simplify this expression, we eliminate the b -dependence of Eq. (2.53) by assuming an average, constant gain over the horizontal diameter of the seed beam d_s :

$$\bar{\rho} = \frac{2}{d_s} \int_0^{d_s/2} \rho(b) db = \frac{2}{\epsilon\alpha_p} \left[1 - \frac{2}{d_s\alpha_p} \sinh(d_s\alpha_p/2) e^{-\alpha_p\epsilon L/2} \right]. \quad (2.55)$$

Assuming a finite duration of the pump pulse τ_{pump} (in the experiments, the amplifier was pumped quasi-continuously), we arrive at a compact expression for the amplified signal intensity:

$$\ln \left(\frac{I_{out}}{I_{in}} \right) + \frac{I_{out} - I_{in}}{I_{sat}} = \ln(G_0) \quad (2.56)$$

with:

$$\ln(G_0) = \eta \frac{\alpha_p P}{I_{sat} H L} \left(1 - e^{-\tau_{pump}/\tau} \right) \bar{\rho}. \quad (2.57)$$

The small signal gain coefficient G_0 can then be used in conjunction with Eq. (2.45) to estimate the output fluence after the grazing-incidence amplifier, which is employed in Sec. 3.2 to analyze the experimentally obtained gain from the developed pre-amplifier.

CHAPTER 3

THE DOUBLE-PULSE PUMP AMPLIFIER SYSTEM

The main experimental work in the course of this thesis consisted of the development of a new laser system capable of producing high-energetic frequency comb pulse pairs at different delays. In order to drive the parametric amplification process, this requires even higher-energy, picosecond *pump* pulse pairs, whose inter-pulse delay can be changed quickly on a time scale stretching from nano- to microseconds. In addition, the pump pulses of different delays should travel the same optical path in the amplifier to minimize wavefront deviations while the delay is changed. The outline of this technical chapter describing the development of the double-pulse pump laser system is sketched in Fig. 3.1. First, the home-built Nd:YVO₄ master oscillator is described in Sec. 3.1. After temporal selection using programmable pulse pickers, the pulse pairs are first amplified in a pre-amplifier based on ultrahigh-gain grazing-incidence Nd:YVO₄ slabs (Secs. 3.2 and 3.3), and then seeded into a Nd:YAG post-amplifier to further increase the energy of the pulse pairs to the 100 millijoule-level as described in Sec. 3.4.

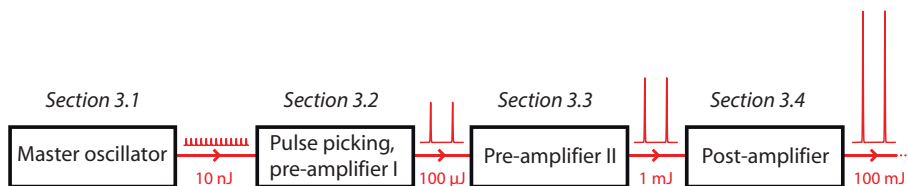


FIGURE 3.1: Outline of this chapter, indicating the different stages of the pump laser system and the characteristic pulse-energy levels.

3.1 The master oscillator of the pump laser

Passively mode-locked oscillators emitting picosecond pulses around a center wavelength of 1064 nm and multiple watts of average power are available from a range of companies (see, e.g., [67, 68]). However, these commercial products typically have a very limited tuning range of the cavity length and, therefore, do not allow for significant changes of the repetition rate f_{rep} . Therefore we chose to build the master pump oscillator ourselves, including convenient feedback mechanisms for short- and long-term stabilization of f_{rep} .

3.1.1 Laser gain material and diode pumping

Considering potential gain materials, the choice was limited to materials compatible to the 1064 nm emission line of Nd:YAG, the preferred material for the post-amplifier (see Sec. 3.4). This constraint and its high emission cross section as compared to Nd:YAG itself make Nd-doped vanadate (Nd:YVO₄) the preferred choice for the gain medium. While Nd:YVO₄ absorbs most strongly around 808 nm, pumping with 880 nm light had been identified already some time ago as an attractive alternative, because the somewhat lower absorption cross section is well-traded for a reduction of thermal issues in the crystal [69]. However, mainly due to the lack of suitable pump diodes, mode-locked vanadate oscillators pumped at 880 nm have only recently been reported [70]. The presented oscillator is pumped by a fiber-coupled pump diode from Jenoptik (JOLD-30-CPXF-1L), delivering up to 30 Watts of 880 nm pump light through a 400 μm core-diameter pump fiber. The pump-light imaging system is shown in Fig. 3.2. A one-to-one telescope comprising two 25 mm focal-length plano-convex lenses images the end face of the pump fiber a few mm deep into the laser crystal. Because the absorption in the Nd:YVO₄ crystal is polarization dependent, a quarter-wave plate and a half-wave plate are placed in the collimated beam section between the two lenses in order to adjust the pump light polarization for optimum absorption. All these pump delivery optics are mounted on a single translation stage together with the pump fiber ferrule so that the exact focus position in the crystal can conveniently be adjusted. The 3x3x8mm³ Nd:YVO₄ crystal (CASTECH Inc.) incorporated a 0.5 at.% Nd-dopant concentration so that the absorption length for the pump light is smaller than the crystal length. Both end faces of the crystal are anti-reflection coated for the 880 nm pump light and slightly wedged (1.5°) to suppress

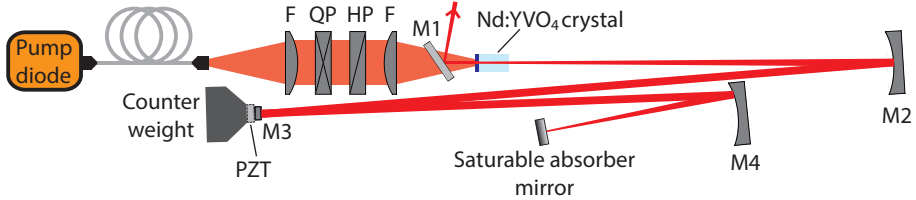


FIGURE 3.2: Schematic of the home-built Nd:YVO₄ master oscillator for the pump laser. F = 25 mm (focal length), QP: quarter-wave plate, HP: half-wave plate, PZT: single-stack piezo transducer, M1: dichroic plane mirror, M2 = -80 cm (radius of curvature), M3: thin, plane mirror, M4 = -100 cm (radius of curvature).

etalon effects. In addition, the end face of the crystal facing the pump beam is coated for partial reflection (90%) of the laser light at 1064 nm, thus acting as one of the cavity end mirrors and as the output coupler of the laser cavity; the opposite crystal end face is coated for maximum transmission at 1064 nm. The crystal is wrapped in indium foil and mounted in a water-cooled copper mount, temperature-stabilized to around 18°C.

3.1.2 The laser cavity

The laser cavity, as sketched in Fig. 3.2, effectively consists of a telescope between two plane end mirrors. One of the end mirrors is the partially reflection-coated face of the Nd:YVO₄ crystal, the other end mirror is the saturable absorber mirror (SAM) from BATOP GmbH with a modulation depth of 1.2% and a relaxation time of 10 ps. The SAM facilitates the passive mode-locking of the oscillator by providing higher losses for lower laser intensities (see, e.g., [46, 47] for further details concerning the operation principles of pulsed lasers). The size of the beam width* on these end mirrors can be estimated from so-called ABCD-matrix calculations [47], which enable to simulate the propagation of laser beams through optical elements. For the target value of $f_{rep} = 125$ MHz, a stable cavity configuration is suggested from these simulations (see Fig. 3.3) by choosing distances of 245 mm between the crystal face and mirror M2, 635 mm between M2 and M3, and 320 mm between M3 and the saturable

*The beam width w is defined as the radial distance for when the intensity of a Gaussian laser beam has dropped to $1/e^2$ of its peak value. It relates to the full width at half maximum (FWHM) according to $2\ln(2)w^2 = FWHM^2$.

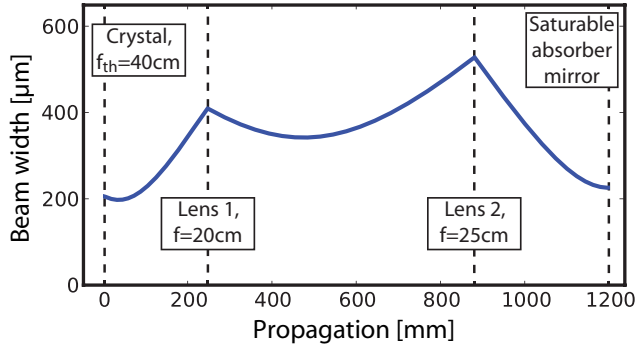


FIGURE 3.3: Simulation of the laser beam width through propagation in the oscillator. Starting from the plane crystal surface, first the thermal lensing ($f_{th} = 40$ cm) and subsequently the two curved cavity mirrors are modeled as lenses. The plane saturable absorber imposes again the constraint of a plane wavefront.

absorber end mirror. At the crystal end face, these distances lead to a plane wavefront with a full width at half maximum (FWHM) intensity width of $245 \mu\text{m}$, well within the pump beam with a diameter of about $400 \mu\text{m}$. At the position of the SAM, the FWHM of the beam is expected to be $265 \mu\text{m}$. For a typical intra-cavity power of 50 W and pulsed operation, the resulting peak fluence of $725 \mu\text{J}/\text{cm}^2$ is about an order of magnitude higher than the specified saturation fluence of the SAM of $70 \mu\text{J}/\text{cm}^2$ but remains well below its damage threshold of $3 \text{ mJ}/\text{cm}^2$.

Starting from these initial parameters, the aligned laser exhibits continuous-wave (CW) lasing for pump powers < 1 W. First mode-locking (with a Q-switch envelope) is typically seen starting from pump powers around 19 W, while for powers above 23 W stable CW mode-locking can be achieved. For a pump power of 25 W, the laser emits more than 5 W of average power with a pulse-to-pulse energy stability of about 0.6% rms measured over tens of minutes. Further details concerning the pulse duration, shape and spectrum are discussed in conjunction with the description of the pre-amplifier in Secs. 3.2 and 3.3.

3.1.3 Repetition-rate control

In order to coarsely adjust the repetition rate, the curved mirror before the SAM (i.e., mirror M4 in Fig. 3.2) is placed on a translation stage, which allows straightforward changes of f_{rep} of ± 3 MHz with minor

realignment of the cavity end mirrors. The stabilization of a certain repetition rate to a stable, radio-frequency local oscillator is performed via small cavity lengths adjustments (in the order of $1\ \mu\text{m}$) by cavity mirror M3 that is glued onto a single-stack piezo transducer (PZT, from Physik Instrumente GmbH). The PZT in turn is glued onto a heavy counterweight consisting of a copper cone filled with lead [71]. Because of the limited range of the PZT, thermal drifts of the cavity length require an additional coarse but not necessarily fast feedback mechanism of the cavity length. This is accomplished by applying feedback via the temperature of the water-cooled baseplate of the oscillator, which is adjusted automatically (via a small computer program) as soon as the continuously monitored voltage of the PZT approaches its lower or upper limit.

3.2 Tailored pulse sequences from an 880 nm pumped Nd:YVO₄ bounce amplifier

In this section, we discuss an 880 nm quasi-continuously pumped grazing-incidence Nd:YVO₄ “bounce” amplifier, operating at 300 Hz repetition rate. More than 70 dB small signal gain is achieved with a single crystal. Combined with fast programmable modulators, high-contrast and near-diffraction limited pulse sequences at the 100 μJ -level are produced that can be tailored in terms of pulse duration, amplitude, and a temporal spacing well into the microsecond range.

3.2.1 Introduction

A rising number of research groups have developed TW peak power, ultrafast optical parametric chirped-pulse amplifier systems given their considerable potential in fields such as attoscience and high-energy physics (see, e.g., [72–74]). Recently we have shown that such a system is also well suited to perform frequency comb metrology in the extreme ultraviolet by amplifying and upconverting two consecutive pulses from a near-infrared frequency comb laser [31]. This approach requires a carefully synchronized pump pulse for each frequency comb pulse that is amplified in the parametric amplifier. Up to now, these have been generated by applying beam splitters and a fixed delay line in the pump laser. Here we present a more versatile and general approach using an ultrahigh-gain amplifier combined with fast modulators. The system em-

employs a grazing-incidence “bounce” amplifier based on Nd³⁺-doped gain material (Nd:YVO₄), which benefits in particular from high-peak-power QCW diode pumping [65]. Hundreds of μJ of amplified pulse energies have been reported for picosecond pulses with small signal gains of around 40 dB and 60 dB for single- and double-slab modules, respectively [66]. To the best of our knowledge, all reported Nd³⁺-doped bounce amplifiers so far (see, e.g., [65, 66, 75–77]) have been pumped by 808 nm light, although direct pumping in the upperband laser level at 880 nm would lead to higher quantum efficiency and lower thermal distortion [69].

Here we present the first Nd:YVO₄ bounce amplifier that takes advantage of an 880 nm pumping scheme. Together with spectral clipping and the combination of fast electro-optical and high-contrast acousto-optical modulators, the system produces near-diffraction limited pulse sequences with widely tunable timings, intensities and pulse lengths.

3.2.2 Experimental setup

Figure 3.4 shows a simplified sketch of the experimental setup. The master oscillator is the home-built high-power Nd:YVO₄ laser described in Sec. 3.1, mode-locked with a semiconductor saturable absorber mirror and pumped with 24 W at 880 nm. It provides 0.25 nm spectral bandwidth in a 126 MHz pulse train with 5 W average output power.

A slit on a translation stage close to the Fourier plane of a 4f-grating system is used for spectral selection. Because of the high-power master oscillator and overall efficiency of 60% of the grating system, more than 90% of the spectral power can be clipped while still obtaining sufficient seeding energy ($\gtrsim 10$ pJ) for the amplifier. Hence a great flexibility in terms of amplified bandwidth and center wavelength is achieved, and the system supports Gaussian-shaped pulses as short as 12 ps (full bandwidth) to about 100 ps (10 pJ seeding energy). For the presented measurements, the spectral clipping is set to transmit $\Delta\lambda \lesssim 0.05$ nm (resolution-limited by the optical spectrum analyzer) at the peak of the amplifier emission spectrum. This results in a 59 ps Gaussian-shaped pulse, which is equal to the typical pump pulse length employed in our parametric amplifier system [31]. The returning beam is extracted via the rejection port of the optical isolator and coupled into a single-mode fiber.

In order to select individual pulses from the 126 MHz oscillator pulse train, a fast electro-optical switch is needed. Suitable bulk Pockels cells

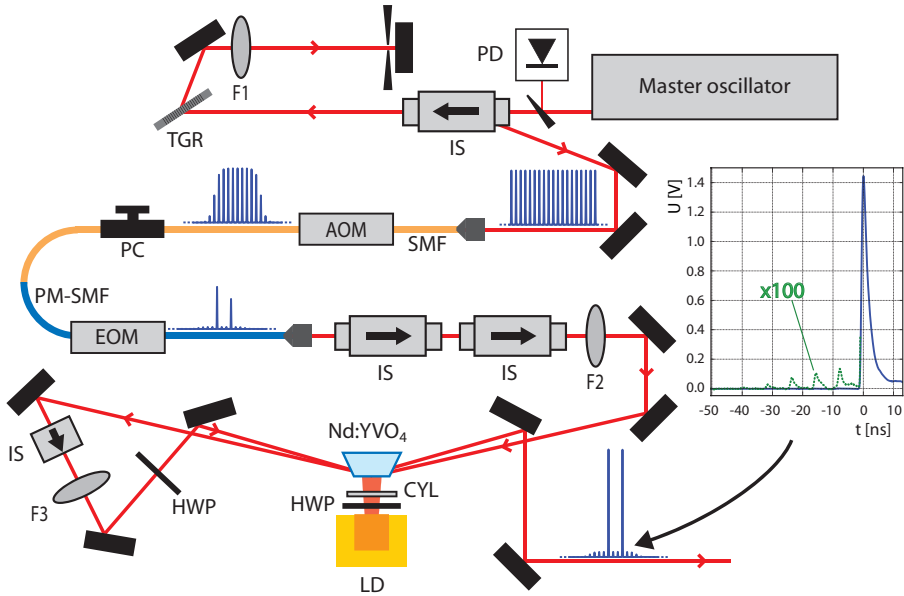


FIGURE 3.4: Schematic of the experimental setup. PD: photodiode, IS: optical isolator, TGR: transmission grating (1680 lines/mm), SMF: single-mode fiber, AOM: acousto-optical modulator, PC: polarization controller, PM-SMF: polarization-maintaining single-mode fiber, EOM: electro-optical modulator, F1 = 30 cm (focal length), F2 = 75 cm, F3 = 60 cm, HWP: half-wave plate, CYL: cylindrical lens, focal length $f = 25$ mm, LD: laser diode. The inset shows an oscilloscope trace illustrating the amplified pulse contrast.

require electrical pulses of a few kV and are limited to repetition rates at the kHz-level. For the implemented fiber-coupled EOM (AM 1060 HF, Jenoptik), less than 3 V is needed. Hence, it can be controlled by combining different output channels from a commercial delay generator (DG645, Stanford Research Systems) providing full and programmable control over the picked pulse sequences in terms of amplitude and timing. In order to improve the extinction ratio of 33 dB of the fast EOM, it is augmented with a slower, 30 ns rise time fiber-coupled AOM (T-M150-0.4, Gooch and Housego). This combination provides an extinction ratio of more than 90 dB for pulses outside of both picking gates and introduce losses of 10 dB.

The amplifier medium consists of a single 5°-wedged, 1 at.-%-doped 2x4x20 mm³ Nd:YVO₄ crystal. It is anti-reflection coated for 880 nm at the pump surface and for 1064 nm at the entrance and exit sides. The

crystal is pumped at a repetition rate of 300 Hz by 130 μs long pulses from a fast axis-collimated 170 W peak power QCW 880 nm linear diode array. A half-wave plate is used to rotate the polarization of the pump diode parallel to the c-axis of the Nd:YVO₄ crystal and a 25 mm focal length cylindrical lens is used to obtain a gain region height of 0.6 mm. The seed beam diameter and internal grazing angle of 0.34 mm and 2.8° are increased to 0.41 mm and 3.4° from the first to the second pass, respectively. The triangular-shaped delay arm between the passes allows the incorporation of a low-power isolator that prevents backwards selfseeding from the amplifier.

3.2.3 Amplifier performance and modeling

In Fig. 3.5(a), the extracted pulse energy for a single seed pulse is shown for single- and double-pass operation (including the losses of the isolator after the first pass). At 62 pJ seed energy, a maximum of 182 μJ could be extracted corresponding to a saturated gain of 65 dB. For low seed energy, the unsaturated small signal gain exceeded 70 dB. The unseeded average power of the ASE is less than 4% of the seeded output power.

We adapted the model developed by Agnesi et al. [78] to simulate the expected gain for our amplifier configuration. The model approximates the pump and signal beam geometry and calculates the gain according to the Franz-Nodvik amplifier theory [64]. As an extension, we incorporated the depletion of the gain of the individual amplifier stages due to ASE. According to [43], ASE reduces the small signal gain coefficient g_0 to:

$$g(L) = \frac{g_0}{L} \int_0^L \frac{F_p/F_{ASE}(0) - \exp[g(z)]}{F_p/F_{ASE}(0) + \exp[g(z)]} dz \quad (3.1)$$

where L is the length of the pumped region in the crystal and F_p is the pump fluence. The fluence of ASE at $L = 0$ is estimated as:

$$F_{ASE}(0) = \frac{\eta_F \Delta\Omega \hbar\omega_{ASE}}{4\sigma_{ASE}T} \quad (3.2)$$

and depends on the fluorescence quantum yield η_F , the solid angle $\Delta\Omega$ from the exit to the entrance area of the gain sheet and on the fluorescence lifetime and cross section, T and σ_{ASE} , respectively. The ratio $F_p/F_{ASE}(0)$ (~ 39 dB in the present setup) represents the ultimate limit of small signal gain for a single pass due to ASE depletion.

Apart from the assumed pump saturation intensity of the crystal of $I_{p,sat} = 5.2$ kW, which was derived from the absorption measurements

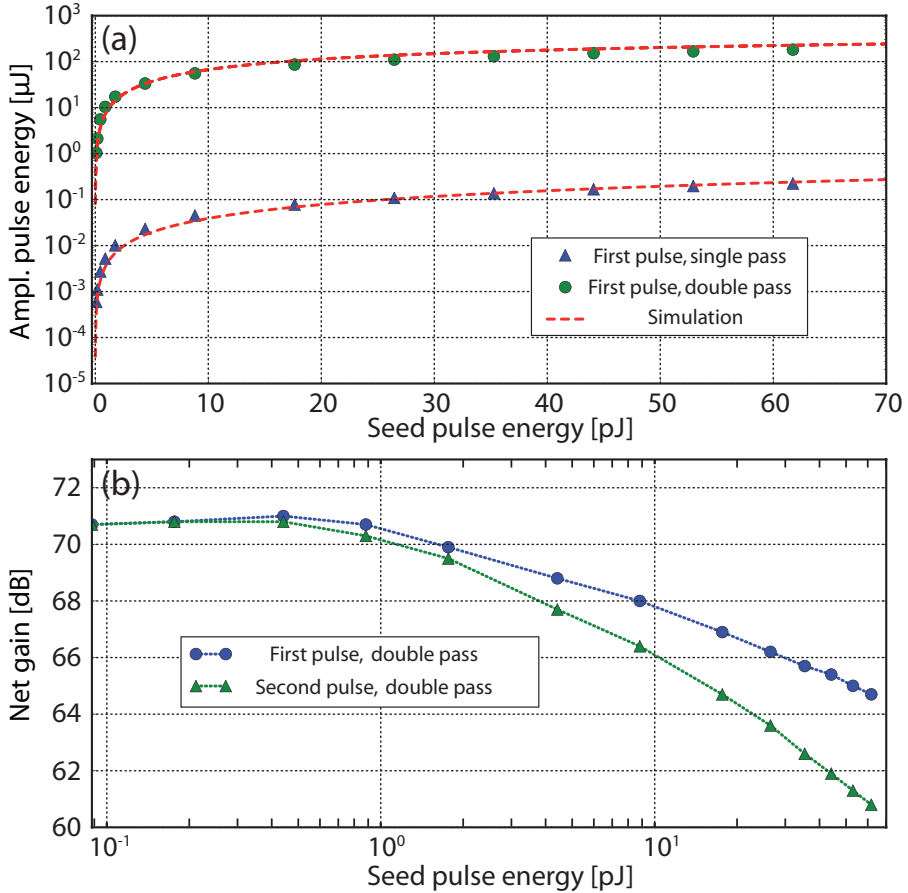


FIGURE 3.5: Extracted pulse energy from the amplifier versus seed energy. (a) Single pulse in single and double-pass configuration. (b) Achieved double-pass gain factors for a pulse pair (32 ns spacing).

at 880 nm in [79] and scaled by the emission bandwidth of the pump diode, the biggest uncertainty in the simulation results stems from the uncertainty of the stimulated emission cross section σ_e of Nd:YVO₄ at 1064 nm. Recently published values of σ_e range from $1.14 \times 10^{-20} \text{ cm}^2$ [80] to $1.44 \times 10^{-20} \text{ cm}^2$ [81]. A good agreement between our experimental data and the theoretical model was achieved for an emission cross section of $\sigma_e = 1.10 \times 10^{-20} \text{ cm}^2$. A slight underestimation of σ_e can be due to intrinsic model approximations and imperfect beam matching of pump and seed light. Excluding the ASE depletion of the gain in the model

results in an underestimation of σ_e of about 10% or an overestimation of the small signal gain by a factor of ten.

While Fig. 3.5(a) describes single pulse operation, Fig. 3.5(b) visualizes how the gain decreases for a second, slightly delayed pulse due to gain depletion of the first pulse. The pulse pair was created by combining two individual output channels from the delay generator as the input signal for the EOM. Hence the amplitude ratio of the two pulses can be freely adjusted and for seed energies of the first and second pulse of about 30 pJ and 60 pJ, respectively, two equally energetic pulses of about 100 μ J were obtained. The spacing between the two pulses can be changed by multiples of the pulse separation of the master oscillator as shown in Fig. 3.6(a-c) for different pulse delays. The energy of both pulses fluctuated by less than 1% rms due to saturation in the amplifier. The pulse train shown in Fig. 3.6(d) was realized by picking 5 pulses of

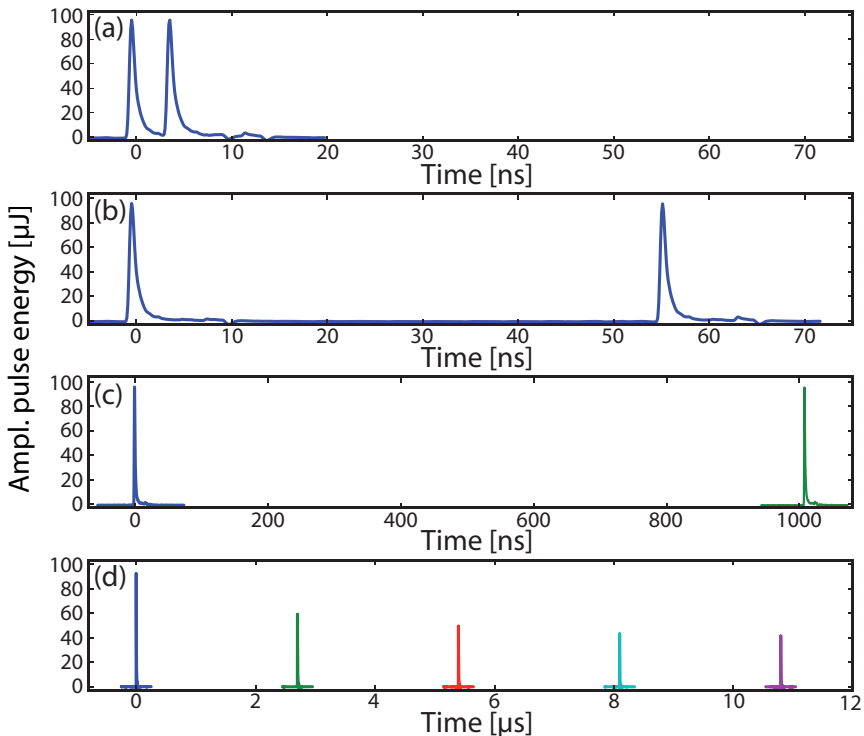


FIGURE 3.6: Oscilloscope traces of pre-compensated pulse pairs with spacing of (a) 8 ns, (b) 56 ns and (c) 1009 ns; (d) shows an uncompensated pulse train with 2.7 μ s spacing.

equal seeding energy of 23 pJ. By combining more individual outputs from the delay generator (or external modulation of the voltage pulse), one can straightforwardly tailor such sequences of MW peak power pulses in terms of spacing and amplitude.

Thanks to the low average thermal load on the amplifier crystal (owing to QCW pumping at 880 nm), the beam hardly deteriorates through the amplification process as can be seen in Fig. 3.7. The beam width measurement after focusing the amplified pulses with a 25 mm focal length lens indicates $M^2 < 1.2$ for both axis. The slight ellipticity of the beam is due to the non-circular gain sheet, which is imprinted on the amplified beam.

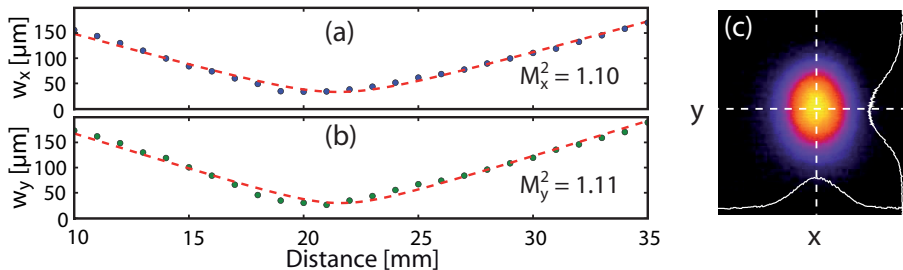


FIGURE 3.7: Beam width measurements and fits of (a) horizontal and (b) vertical axes of the amplified beam; (c) CCD image of the unfocused amplified beam 20 cm from the Nd:YVO₄ crystal.

3.2.4 Conclusion

We have demonstrated an 880 nm QCW pumped single-slab Nd:YVO₄ bounce-amplifier system with more than 70 dB small signal gain, which produces near-diffraction limited pulse sequences with an energy of up to 100 μJ per pulse and an intensity stability better than 1%. It provides an excellent front-end for post-amplification based on Nd:YVO₄ or Nd:YAG, and is capable of generating double-pulse sequences over a time scale of microseconds without a physical delay line. This is particularly interesting as a driver for parametric amplification and harmonic upconversion of frequency comb laser pulses, which could improve the accuracy of extreme ultraviolet frequency combs based on this principle [31] by several orders of magnitude.

3.3 A 1.8 mJ, picosecond Nd:YVO₄ bounce-amplifier pump front-end system for high-accuracy XUV-frequency comb spectroscopy

In this section, an extension of the previously described pre-amplifier stage (cf. Sec. 3.2) is presented. This results in an 880 nm quasi-continuously pumped, grazing-incidence “bounce” amplifier system capable of producing picosecond pulses (12 ps - 100 ps) and tailored pulse sequences at the mJ-level. More than 1.8 mJ of pulse energy was achieved for a 58 ps pulse using sub-100 pJ seeding energy (up to a repetition rate of 300 Hz). Owing to saturation effects, the pulse-to-pulse energy fluctuations were as low as 0.3% rms. The time delay between these pulses can be changed between 8 ns and $>1 \mu\text{s}$, providing a promising pump laser system for parametric amplification and subsequent upconversion of near-infrared frequency combs to the extreme ultraviolet (XUV).

3.3.1 Introduction

Bounce amplifiers have been used in a variety of configurations (see, e.g., [65, 66, 75–77]). By employing high peak power, QCW pump diodes, pulse energies up to 1 mJ have been reported for sub-nanosecond pulses with microjoule seeding energies [77, 82].

We already demonstrated the combination of a single bounce amplifier with a programmable pulse-picking unit capable of producing tailored pulse sequences at the 100 μJ -level [83] (see Sec. 3.2). Here we report on the extended version of that amplifier system delivering more than 1.8 mJ in 58 ps pulses using sub-100 pJ seeding energy. To the best of our knowledge, this presents both the highest gain and highest pulse energy that have been reported for amplifiers in a single-bounce geometry. With the help of spectral clipping and high-contrast modulators, the system supports pulse durations in the range of 12 ps to 100 ps and produces highly stable (0.3% rms), high-contrast millijoule pulse sequences.

3.3.2 Experimental setup

A simplified sketch of the experimental setup is shown in Fig. 3.8; the master oscillator is the home-built Nd:YVO₄ laser described in Sec. 3.1,

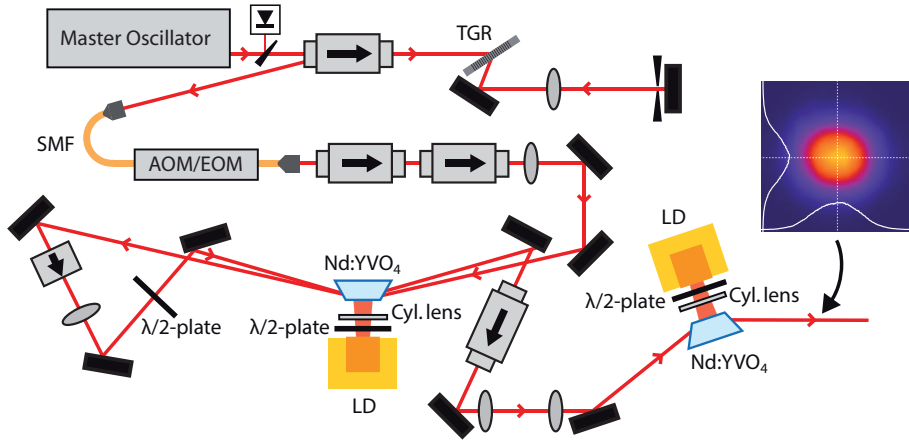


FIGURE 3.8: Schematic of the experimental setup illustrating spectral selection (TGR: transmission grating), temporal selection (SMF: single-mode fiber, AOM: acousto-optical modulator, EOM: electro-optical modulator) and the QCW-pumped Nd:YVO₄ amplifier (LD: laser diode). The inset shows the amplified beam profile.

providing Gaussian-shaped pulses of 0.25 nm spectral bandwidth in a 126 MHz pulse train with 5 W average output power.

3.3.2.1 Spectral clipping and pulse picking

Typical pump pulse durations required for our high-power optical parametric amplifier are in the order of a few tens of picoseconds. Therefore, the initial pulse duration of 12 ps was adjusted by spectral clipping via a movable slit close to the Fourier plane of a 4f-grating system. The high-energy pulses from the master oscillator (40 nJ) enable a considerable flexibility in terms of the amplified bandwidth and center wavelength and leave sufficient pulse energy for subsequent amplification in the saturated regime. The system supports Gaussian-shaped pulses from 12 ps to about 100 ps (10 pJ seeding energy for the first amplifier). For the reported experiments, the seed pulse duration was adjusted to ~ 60 ps (Fig. 3.9(a-d)) according to the requirement of our amplifier system [31]. The center wavelength was matched to the peak wavelength of the amplified spontaneous emission (ASE) spectrum of the amplifier for maximum gain.

The full pulse train was then coupled into a single-mode fiber in order to spatially filter the beam and mechanically decouple the oscillator from

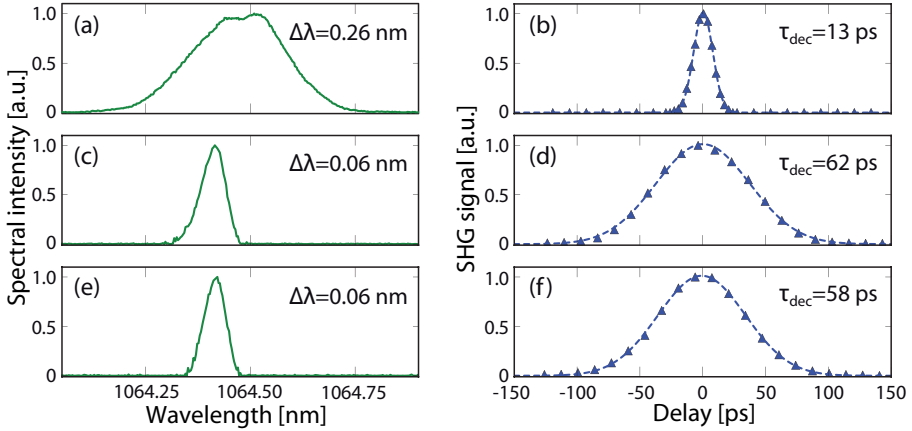


FIGURE 3.9: Optical spectra (left column) and second-harmonic, background-free autocorrelations (right column, τ_{dec} is the deconvolved pulse duration derived from the Gaussian fits indicated by the dashed lines) of the full bounce-amplifier bandwidth (a, b), the clipped seeding pulse (c, d) and the amplified pulse (e, f).

the amplifier. In addition, it allowed the implementation of a fast and programmable fiber-coupled pulse-picking system, which is described in detail in [83] (cf. Sec. 3.2).

3.3.2.2 Grazing-incidence amplifiers

After spectral and temporal selection, the pulse train passes a double, >80 dB isolation stage to prevent back reflections into the pulse-picking system. The pulses of sub-100 pJ energy are then amplified in a bounce-amplifier system comprising two Nd:YVO₄ crystals, both 5°-wedged and anti-reflection coated for pump and lasing wavelength. Among the range of Nd³⁺-doped gain materials, Nd:YVO₄ was chosen as gain material because of its large stimulated emission cross section ($\gtrsim 1.1 \times 10^{-18}$ cm² [80]) and the good spectral overlap with the Nd:YAG emission spectrum, which is commonly used for high-energy post-amplification because of its superior thermal properties. The first crystal (2x4x20 mm³, 1 at.-%-doped) was pumped with 135 μ s long pulses from a 180 W peak power QCW 880 nm linear diode array. The pump pulse duration was not increased any further to limit excess ASE in the first amplifier stage, which otherwise extracts a considerable part of the stored energy in the following amplifier sections.

In addition, a second, 4x6x20 mm³ crystal was implemented and pumped by a similar diode with 200 μ s long pulses of 250 W peak power. In order to increase the damage threshold for the pump light, a lower doping of 0.5 at.% was chosen for the second crystal [84]. In both cases, half-waveplates are used to rotate the polarization of the pump beam parallel to the c-axis of the crystal, and cylindrical lenses are used to adjust the beam height to about 0.6 mm (first crystal) and 0.9 mm (second crystal). The maximum repetition rate of the pump pulses for this experiment was 300 Hz due to the available diode driver but is in principle only limited by the maximum duty cycle of the QCW diodes of 10%.

The first crystal was double-passed by the seed beam with diameters and internal grazing angles of 0.3 mm and 2.8° (first pass), and 0.4 mm and 3.4° (second pass); the triangular-shaped delay arm allows the incorporation of a low-power, 30 dB isolator. After double-passing the first crystal, the seed beam diameter was increased to 0.9 mm and the beam sent through the second amplifier crystal at an internal grazing angle of 4.5°. Apart from suppressing dangerous back reflections of the amplified seed beam, the two isolators in between the amplifier stages also prevent backwards seeding of the individual stages, which otherwise significantly reduces the available stored energies in the crystals.

3.3.3 Results and discussion

3.3.3.1 Single pulse operation

At a repetition rate of 300 Hz, we obtained 1.83 mJ of pulse energy using 62 pJ seeding energy. To the best of our knowledge, this is the highest net gain (75 dB) and pulse energy achieved so far for this amplifier geometry. As can be seen in Fig. 3.9(e, f), spectrum and pulse duration remain basically unchanged during the amplification process indicating the absence of significant nonlinear effects and gain narrowing. Decreasing the repetition rate by a factor of ten revealed no apparent change of the amplified beam profile, hence no deterioration of the nearly-Gaussian beam (inset of Fig. 3.8) due to thermal effects could be observed.

The stability of the amplified pulse energy was measured with a photodiode and indicated fluctuations in the order of 0.3% rms within a timespan of 300 seconds (Fig. 3.10). The reasons for this high stability were twofold. First, the QCW pump pulse duration was chosen significantly longer than the upper-state lifetime of Nd:YVO₄ ($\lesssim 100 \mu$ s [80]),

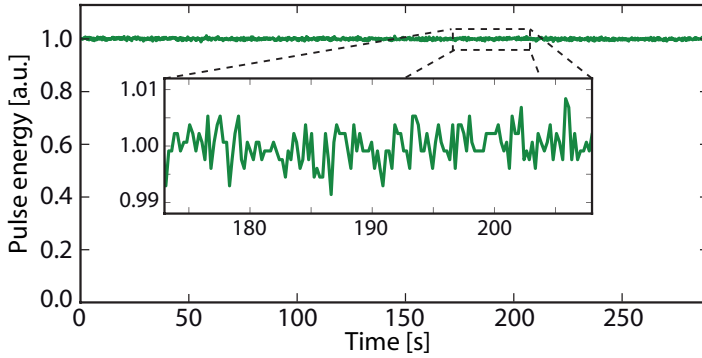


FIGURE 3.10: Measured pulse energy after the bounce amplifier in single-pulse operation (0.3% rms).

which completely saturates the inverted region in the amplifier crystal and, therefore, makes the system less prone to fluctuations of the QCW diode output power. Second, gain depletion damped the amplified pulse-energy fluctuations originating from amplitude noise of the master oscillator (0.6% rms within 300 seconds).

The oscilloscope trace depicted in Fig. 3.11 illustrates the effect of the gain depletion on the amplification of a second, slightly delayed pulse of equal seeding energy. The inset shows the amplified pulse-to-pulse

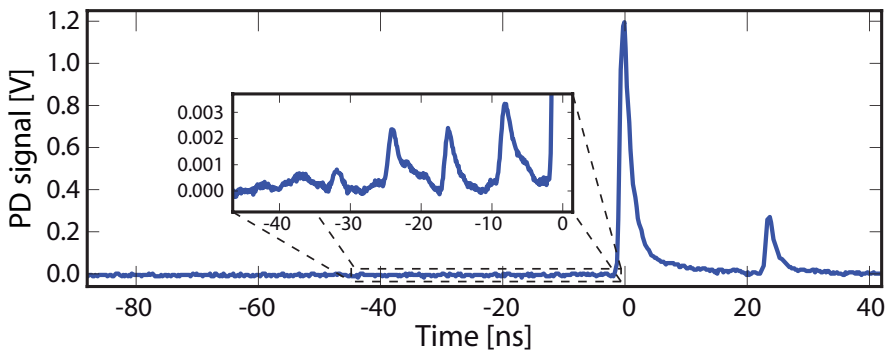


FIGURE 3.11: Time trace of an amplified pulse pair of equal seeding energy (24 ns spacing). The pulse energy of the second pulse is decreased by a factor of four due to gain depletion. The inset shows the amplified short-time contrast of $>400:1$.

contrast of 400:1, which due to saturation effects is slightly lower than the initial >1000:1 contrast after the pulse picking.

3.3.3.2 Double-pulse sequences

In addition to the described single-pulse operation, the system can also be used to produce adjustable pulse sequences as described in [83] but now producing equal pulses at the mJ-level as shown in Fig. 3.12. Because of the high level of gain depletion, the seed energy of the first pulse was adjusted to be $\lesssim 20\%$ of the seed energy of the second pulse.

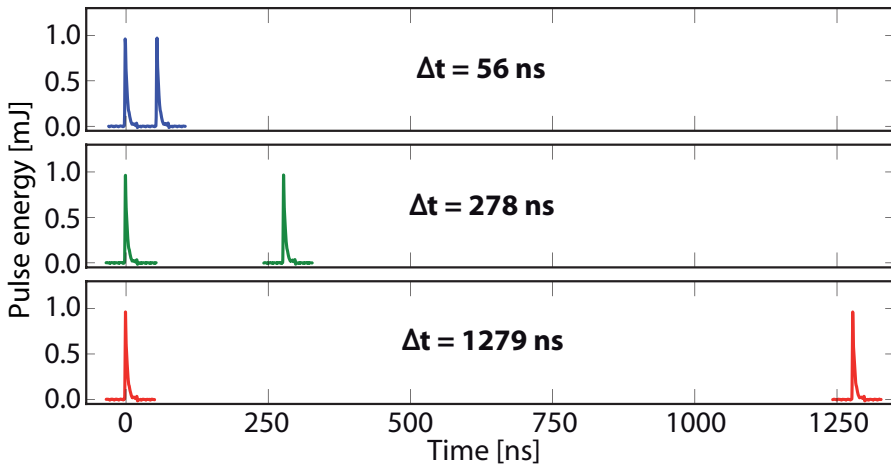


FIGURE 3.12: Time traces of amplified pulse pairs after the bounce amplifier for different temporal spacings (equal to multiples of the cavity round-trip time of the master oscillator).

3.3.4 Conclusion

We presented a pump front-end laser system based on two ultrahigh-gain grazing-incidence Nd:YVO₄ amplifier slabs, delivering highly stable (0.3% rms) picosecond pulses of more than 1.8 mJ at a repetition rate of 300 Hz. In addition, with the help of fast programmable modulators adjustable mJ pulse sequences were produced. The extended temporal delay between these pulse pairs will potentially enable kHz-level XUV frequency comb spectroscopy based on the two-pulse approach as demonstrated in [31].

3.4 Post-amplification to the 100 millijoule-level

In order to further increase the pulse energy from 1 millijoule to the 100 millijoule-level, two different post-amplifiers were employed. Both amplifiers are based on Nd:YAG gain media, which exhibits better thermal properties as opposed to Nd:YVO₄ used for the oscillator and pre-amplifier. In addition, Nd:YAG crystals can be produced in larger dimensions, thus allowing for larger beam diameters in the amplifier, which is beneficial for circumventing laser damage. The initially used post-amplifier was developed by S. Witte [58] and had been the “workhorse” for consecutive experiments (e.g., [31, 85]). Therefore, we will only briefly mention its basic principle in Sec. 3.4.1. However, before the spectroscopic measurements described in Ch. 5 were carried out, the post-amplifier was replaced with a new amplifier based on diode-pumped amplifier modules, which is described in more detail in Sec. 3.4.2.

3.4.1 Flashlamp-pumped amplifier in ring geometry

The initially used post-amplifier consisted of two flashlamp-pumped amplifier modules (EKSPLA) comprising two Nd:YAG rods of 10 cm length and 12 mm diameter. Because the small signal gain factor per module is only $\sim 4 - 6$, the two modules were passed twice in a ring geometry to obtain a net gain of more than 100, producing around 140 mJ of pulse energy. In the first round, the diameter of the Gaussian seed beam was only about half the diameter of the rod, while for the second round a telescope was employed to increase the beam diameter in order to slightly overfill the whole amplifier rod. This enabled the production of nearly flat-top pump beam profiles, which is beneficial for both avoiding laser damage and efficient pumping of the parametric amplifier.

While the large diameter rods allow for high energy extraction, the flashlamp pumping imposes two main limitations. First, because the flashlamp emission spectrum is very broad, pumping is not very efficient, which results in the rather low gain. As a consequence, the complex double-pass ring geometry was required for sufficient gain and after each periodic replacement of the flashlamps (after $\sim 10^7$ shots), a realignment of the amplifier was required. Second, the large amount of excess heat deposited in the amplifier modules causes strong thermal lensing, depolarization and aberrations. Although these effects can largely be compensated by using an active rotator between the amplifier modules, the thermal effects still compromise the obtainable beam quality. In ad-

dition, because of these effects and the high requirements for the pulsed driver of the amplifier units, the maximum repetition rate of the amplifier was limited to a few tens of Hz.

3.4.2 Amplification with diode-pumped modules

Primarily in order to facilitate higher repetition rates (up to 300 Hz) and reduce thermal effects in the amplifier, a new post-amplifier based on high-gain diode-pumped modules was developed. Figure 3.13 shows a sketch of the amplifier geometry starting from the collimated output of the pre-amplifier stage as described in Sec. 3.3. Close to the relay-imaging plane* in between the two passes through the amplifier, a Faraday rotator was employed to rotate the polarization by $2 \times 45^\circ$. This is done to compensate for thermally induced depolarization and also allows to couple out the back-coming beam with a thin-film polarizer in front of the module. The commercial amplifier module (Cutting Edge Optonics, REA6308-3P200H) is based on a 14.6 cm long and 6.4 mm diameter

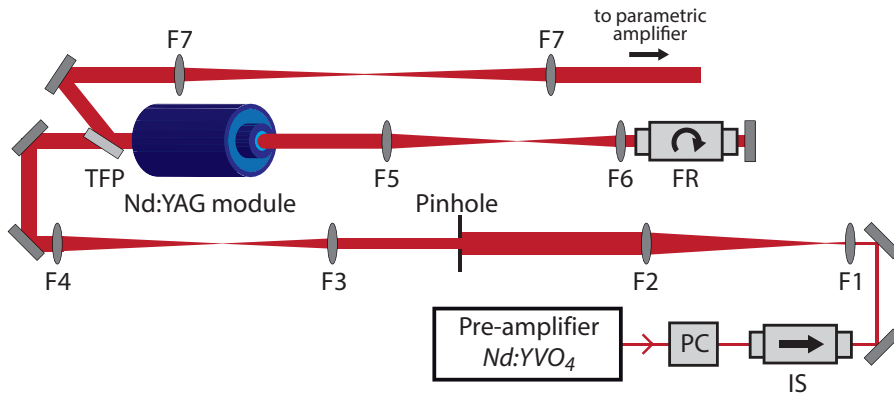


FIGURE 3.13: Schematic of the diode-pumped post-amplifier. The Pockels cell (PC) unit before the isolator (IS) is employed as a pulse picker to suppress amplified ASE from the pre-amplifier and to pre-compensate gain depletion in the post-amplifier. FR: faraday rotator, TFP: thin-film polarizer, F1 = 20 cm (focal length), F2 = 100 cm, F3 = 25 cm, F4 = 35 cm, F5 = 25 cm, F6 = 20 cm, F7 = 100 cm.

*A relay-imaging telescope consists of two focusing optics (e.g., lenses or curved mirrors) of focal lengths f_1 and f_2 , placed at a distance equal to $f_1 + f_2$. In this configuration, the beam at a distance of f_1 before the first optic is fully reconstructed, both in amplitude and spatial phase at a distance of f_2 after the second optic.

Nd:YAG rod, grooved along the pump sides to prevent self-lasing. It is pumped by 120 diode bars with a combined QCW peak power up to 24 kW. The diode bars are arranged in a fivefold pumping symmetry around the crystal rod. The effect of the resulting non-uniform inversion can be seen in Fig. 3.14(a), where a low energy Gaussian seed beam that filled the whole rod was amplified using 110 A current pulses. The amplified beam clearly mirrors the fivefold pumping geometry. In order to obtain a more uniform beam profile, the seed beam diameter in the amplifier rod was limited to 4.9 mm by relay-imaging a circular aperture close to the end face of the rod. This was done by first enlarging the seed beam to 6 mm diameter and subsequently cutting out its center part with a pinhole of 3.5 mm diameter, which was then projected into the amplifier unit by a relay-imaging 7:5 telescope. Relay-imaging is essential because the hard spatial cut made by the pinhole inevitably causes diffraction, which in this case would result in a sinc-like spatial distribution with local intensity maxima that can cause laser damage in the amplifier. Hence starting from the pinhole, the pump beam has

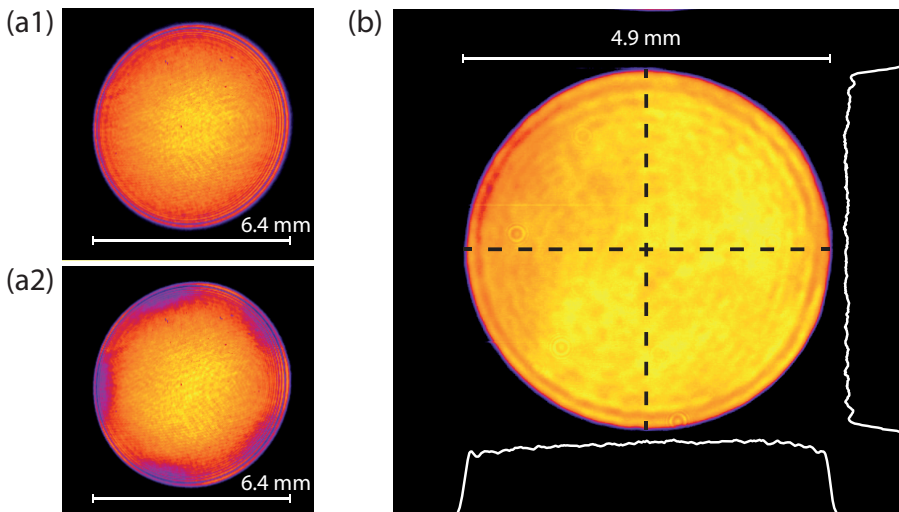


FIGURE 3.14: Amplified beam profiles after the diode-pumped post-amplifier. (a1) Low seed energy, non-amplified Gaussian beam filling the whole 6.4 mm diameter amplifier rod. (a2) Amplified beam profile, showing the fivefold pumping geometry. (b) Amplified beam profile for a maximum seed energy, limited to 4.9 mm diameter. Also shown are the beam cross sections indicated by the dashed lines.

to be relay-imaged throughout the whole amplifier and also later in the parametric amplifier. The result of using only the inner (4.9 mm diameter) part of the 6.4 mm diameter Nd:YAG rod is a much more uniform amplified beam profile as can be seen in Fig. 3.14(b) where the spatially cut seed beam was relay-imaged and amplified to ~ 35 mJ.

Because of the narrow bandwidth of a few nm, the high-power pump light from the diodes is efficiently absorbed in the Nd:YAG rod and facilitates a very high single pass amplification. Figure 3.15 shows the single pass gain for 250 μ s long diode current pulses with peak powers of up to 140 A; the input seed energy was attenuated to 12 μ J to avoid gain saturation effects in the amplifier. As can be seen from Fig. 3.13, the amplifier module was implemented in a double-pass configuration, which straightforwardly provides the required two orders of magnitude gain to amplify the signal pulses to about 40 mJ for moderate driving currents of 80 - 85 A. Indeed, the only reason the pump current was not increased further was because the pulse intensities in the amplifier (~ 3.5 GW/cm²) are getting close to the damage threshold of the amplifier crystal coatings.

While the output energy is currently limited to about 40 mJ pulse energy because of laser damage thresholds, this energy can be further increased by implementing a second amplifier stage using a 10 mm diameter rod in an analogous way. We have recently used this exact combination for a post-amplifier in a different experimental setup to produce 130 mJ pulses even at a much higher repetition rate of 300 Hz [86]. For the experiments described in Ch. 5, the obtained 40 mJ pulses at 28 Hz (same repetition as previously used with the flashlamp amplifier) was fully sufficient.

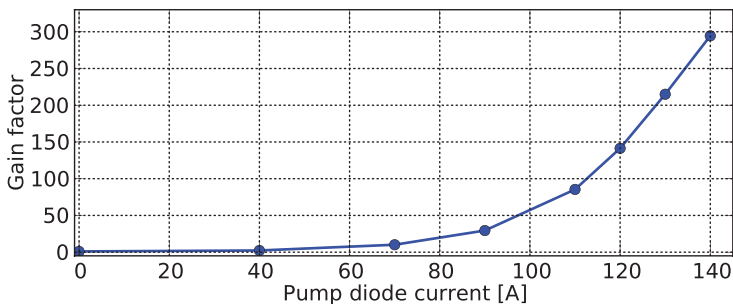


FIGURE 3.15: Gain factor of the diode-pumped Nd:YAG post-amplifier for different pump currents and a low input signal energy of 12 μ J.

CHAPTER 4

MULTI-DELAY, PHASE-COHERENT PULSE PAIR GENERATION FOR PRECISION RAMSEY-COMB SPECTROSCOPY

In this chapter, we demonstrate an experimental system capable of generating phase-stable mJ-pulse pairs at programmable inter-pulse delays up to hundreds of nanoseconds. A detailed investigation of potential sources for phase shifts during the parametric amplification of selected pulses from a Ti:sapphire frequency comb are presented, both numerically and experimentally. It is shown that within the statistical uncertainty of the phase measurement of 10 mrad, there is no dependence of the differential phase shift over the investigated inter-pulse delay range of more than 300 ns. In combination with nonlinear upconversion of the amplified pulses, the presented system will potentially enable short wavelength (<100 nm), multi-transition Ramsey-comb spectroscopy at the kHz-level.

4.1 Introduction

The realization of optical frequency combs (FC) based on mode-locked oscillators has enabled the production of phase-coherent optical pulse trains [14, 15] and the direct measurement of optical frequencies leading to various applications such as attoscience [22], quantum control [87] and precision metrology [25]. While for many purposes the output power of an unamplified FC is sufficient, there are many applications which require a higher peak power than an oscillator can deliver. One application in particular is nonlinear upconversion of FCs (which typically operate in the near-infrared) to the extreme ultraviolet (<100 nm) for ultrahigh-precision spectroscopy. In this wavelength region, simple atomic and

molecular systems such as He, He⁺ or H₂ have their principal transitions which can be used for highly-accurate tests of the theory of quantum electrodynamics [31, 88, 89].

One experimental approach to increase the FC pulse intensity uses an enhancement cavity for efficient high-harmonic generation [38, 39] and FC generation in the extreme ultraviolet [40]. As an alternative route, we demonstrated that pulse pairs from a Ti:sapphire FC can be amplified while maintaining their phase coherence; the amplified pulses can then be used to perform high-precision Ramsey-like FC spectroscopy [37, 90]. More recently, this principle was employed with an improved system based on an optical parametric chirped-pulse amplifier (OPCPA) and high-harmonic generation, which resulted in MHz-level FC-spectroscopy in Helium at 51 nm [31].

The parametric amplification of two FC pulses requires a pair of high-energy *pump* pulses, which in [31] were created by splitting a single pump pulse via an optical delay line. This method introduced two main limitations. First, the physical delay line limited the maximum possible temporal delay to about ten nanoseconds. This in turn limited the resolution of the Ramsey-like spectroscopy [2] and changes of the pulse delay at the nanosecond level required a physical change of the delay line and realignment of the amplifier system. Second, due to the additional optical path for the delayed second pump pulse, notable wavefront deviations were introduced, which resulted in phase shifts of the amplified FC pulses in the OPCPA. These amplifier phase shifts had to be monitored constantly with high accuracy (~ 20 mrad) to correct the spectroscopy signals.

In order to lift both these limitations, a new pump front-end system based on fast modulators and ultrahigh-gain Nd:YVO₄ grazing-incidence amplifier has been developed [83, 91]. In conjunction with a Nd:YAG post-amplifier and second-harmonic generation, 532 nm pulse pairs at the 100 mJ-level and programmable delays up to the microsecond range can be produced. These pump pulse pairs then amplify two pulses from a synchronously locked Ti:sapphire FC in an OPCPA similar to the one used in [31].

The upgraded system opens the new possibility to obtain Ramsey-like signals at different and much longer time delays (at multiples of the round-trip time of the oscillators) without any physical change in the setup. If the phase influence of the OPCPA system is constant at different time delays, then this OPCPA phase shift can be eliminated completely by comparing Ramsey signals at different time delays. This

is a fundamental difference to traditional Ramsey spectroscopy where the *absolute* phase shift determines potential frequency errors [92].

It is, however, of vital importance that a potential absolute phase shift between amplified FC pulse pairs does not depend on the inter-pulse delay Δt . A phase shift *difference* $\delta\phi$ between pulse pairs with inter-pulse delays that differ by Δt_{diff} would cause a systematic frequency error of:

$$\delta f = \frac{\delta\phi}{2\pi\Delta t_{diff}}. \quad (4.1)$$

For example, a phase shift difference of $\delta\phi = 5$ mrad for $\Delta t_{diff} = 8$ ns translates into a 100 kHz frequency error.

The systematic investigation of phase shifts caused by the OPCPA system, and in particular their dependence on the inter-pulse delays, constitute the main part of this chapter. First, the investigated experimental setup is outlined in Sec. 4.2. In order to estimate the phase sensitivity of the amplified FC pulses to experimental parameters such as the pump-pulse intensity and the phase-matching angle, simulations of the narrowband OPCPA were carried out and are discussed in Sec. 4.3. The outcome of the theoretical considerations then provides the roadmap for the experimental investigation of the pump pulse pairs for the OPCPA (Sec. 4.4). Finally, in Sec. 4.5, the results of the actual phase-shift measurements of the amplified FC pulses are presented and discussed.

4.2 Setup

4.2.1 Overview of the experimental system

Figure 4.1 shows a schematic overview of the setup used in the experiments. A Nd:YVO₄ pump front-end, quasi-continuously pumped at 28 Hz, delivers picosecond 1064 nm pulse pairs at the mJ-level and is described in detail in [83, 91] (see Secs. 3.1 to 3.3 of the previous chapter). The seed pulses for the pump-pulse amplifier are picked via fast modulators from a home-built, passively mode-locked Nd:YVO₄ oscillator. Two ultrahigh-gain grazing-incidence Nd:YVO₄ amplifier slabs are then employed to boost the pulse energy of the picked pulse pairs to the mJ-level. As opposed to creating the pump pulse pairs via an optical delay line as employed in [31], all pulses travel exactly the same optical path in order to reduce phase effects in the OPCPA due to wavefront differences of the pump pulses. In addition, the inter-pulse delay Δt within one pump pulse pair can be changed by multiples of the cavity

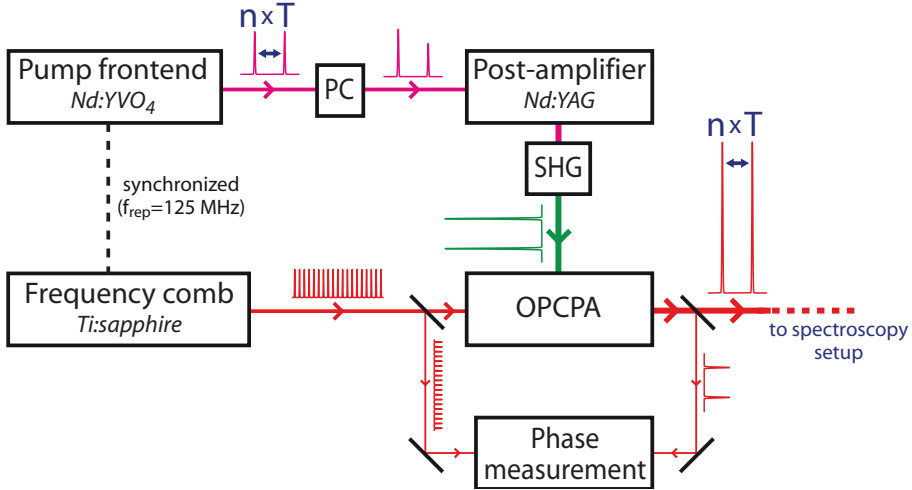


FIGURE 4.1: Schematic of the experimental setup including a Pockels-cell pulse picker (PC), second-harmonic generation (SHG) and the optical parametric chirped-pulse amplifier (OPCPA). A reference fraction of the non-amplified frequency comb pulses is compared with the amplified pulses via spectral interference in the phase-measurement setup. The programmable inter-pulse delay can be changed in steps of the cavity round-trip time ($T = 8$ ns, n is an integer number).

round-trip time of the pump oscillator ($T = 8$ ns) via a programmable delay generator.

A flashlamp-pumped Nd:YAG post-amplifier (see Sec. 3.4 of the previous chapter) further boosts the pulse energy to 140 mJ, and after frequency doubling two 532 nm pulses at the 100 mJ-level are available. In between the pre- and post-amplifier, a Pockels-cell pulse picker can be used for additional pulse shaping by adjusting the intermediate energies of the amplified pulses.

Figure 4.1 also shows the implementation of the phase measurement. In order to measure additional phase shifts induced by the OPCPA, the phases of the two amplified FC pulses are compared with the technique of linear spectral interferometry using 25% of the FC seed power split off before the OPCPA as a reference [55, 93]. By comparing the spectral interference patterns of the two FC pulses, the differential spectral phase induced by the OPCPA can then be determined via a Fourier-transform method [94]. As we will see later, the OPCPA phase shift of the amplified FC pulses crucially depends on the pump pulses used

for the parametric amplification. Therefore, potential pump-pulse differences were investigated by optically gating either the first or the second pulse of the frequency-doubled pump pulse pair. A Shack-Hartmann wavefront sensor and a CCD camera were then used to record the differential wavefronts and different intensity profiles, respectively. However, before we start analyzing the performance of the OPCPA output, we will first introduce further experimental details of the FC seeding source, the electronic synchronization scheme and the amplifier geometry.

4.2.2 The Ti:sapphire frequency comb

The seed pulses for the OPCPA are derived from a home-built Ti:sapphire FC, adapted from the design by A. Wolf [95] and schematically depicted in Fig. 4.2. The Ti:sapphire crystal is placed at Brewster's angle in the focus between two curved mirrors with radii of curvature of 100 mm. A commercial single-mode laser (Verdi V-10, Coherent) is employed to provide 5 W of 532 nm pump light. The particular set of dispersion-adjusted cavity mirrors was chosen to facilitate a ~ 40 nm wide spectrum centered at 770 nm with an average power of 700 mW. For coarse adjustment of the carrier-envelope phase (see Sec. 2.4), a pair of wedges is placed inside the cavity so that the intra-cavity dispersion can be changed by translating one of them. Figure 4.2 also shows the f-2f-detection setup, which allows to stabilize the carrier-envelope phase

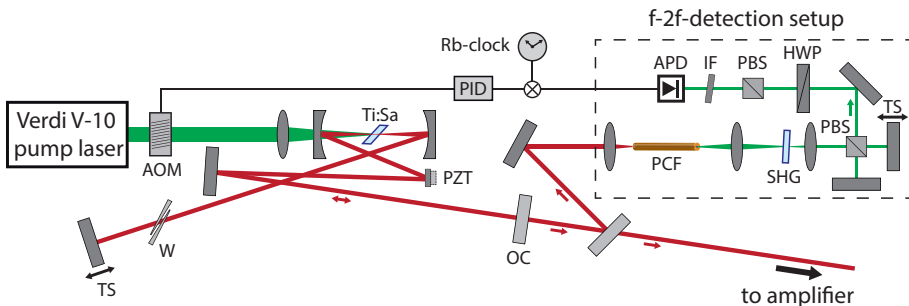


FIGURE 4.2: Schematic of the Ti:sapphire frequency comb functioning as the seed laser for the OPCPA. AOM: acousto-optic modulator, TS: translation stage, W: wedges, PZT: single-stack piezo transducer, OC: output coupler, PCF: photonic crystal fiber, SHG: second-harmonic crystal (BBO), PBS: polarizing beam splitter, HWP: half-wave plate, IF: interference filter, APD: avalanche photodiode, PID: proportional-integral-derivative controller

by referencing it to a radio-frequency standard provided by an atomic Rb-clock (PRS10, Stanford Research Systems). For the f-2f-detection, 25% of the FC output is tapped off and spectrally broadened to an octave-spanning spectrum in 16 cm long photonic crystal fiber (Menlo Systems). From the interference of the short-wavelength part and the frequency-doubled long-wavelength part of the spectrum, the carrier-envelope frequency can be measured as described in Sec. 2.4.1. This frequency can then be mixed with the stable reference frequency from the Rb-clock to provide the error signal for the acousto-optic amplitude modulator that modulates the pump power (see Fig. 4.2).

4.2.3 Electronic synchronization scheme

The repetition rate of the Ti:sapphire FC is locked to a stable radio-frequency reference synchronously with the Nd:YVO₄ pump oscillator. Figure 4.3 shows the electronic scheme providing the feedback signals for the piezo transducers employed to stabilize the length of both laser cavities. The repetition rates of both oscillators are monitored with fast photodiodes (Electro-Optics Technology, Inc.) such that the 76th harmonic* of the repetition rates can be mixed with a ~ 10 GHz stable reference frequency provided by a frequency generator (PSG-L E8241A, Agilent). By adjusting the frequency output of the 10 GHz-frequency generator, the resulting mixing frequency is set to ~ 30 MHz. This mixing product is then mixed again but this time with the ~ 30 MHz output from a direct digital synthesizer (DDS) board (AD9912, Analog Devices) to provide the final error signals for the cavity-length stabilization. In order to adjust the repetition rate of the lasers, the DDS output is scanned in small steps while the GHz-generator frequency output remains constant. The combined locking scheme allows to benefit from both the frequency stability of the GHz-generator and the fast switching and small step size ($\sim \mu\text{Hz}$) of the DDS.

Locking the repetition rate of both oscillators to the same reference frequency is, however, not sufficient for assuring their temporal overlap in the OPCPA since there is in general a constant time offset between the pulses from the two oscillators. A sufficient adjustment of the reference phase at the 76th harmonic is technically challenging. Therefore, a

*Locking to the 76th harmonic instead of, e.g., to the fundamental repetition rate provides an increased “lever arm” (the timing jitter of the laser pulses increases linearly with the harmonic number) and hence enables a tighter lock of the repetition rate.

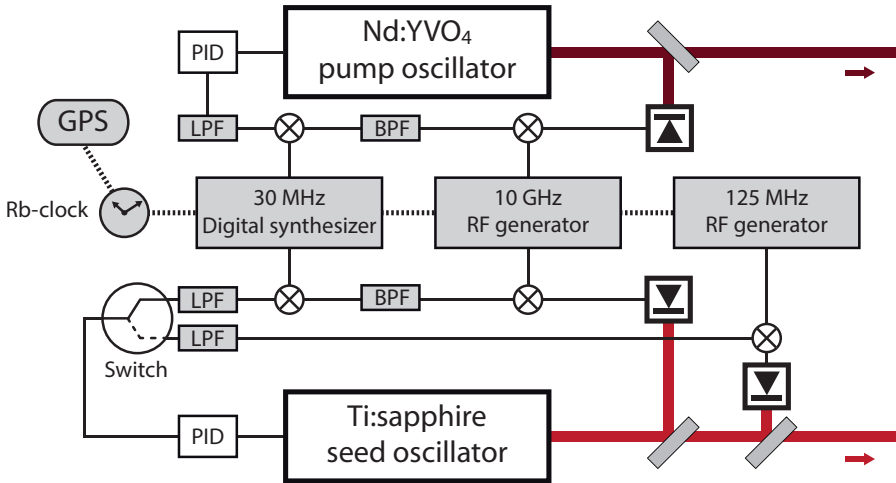


FIGURE 4.3: Electronic locking scheme of the repetition rates of the Ti:sapphire frequency comb seed oscillator and the Nd:YVO₄ pump oscillator. GPS: global Positioning System, BPF: 30 MHz bandpass filter, LPF: 1.9 MHz lowpass filter, PID: proportional-integral-derivative controller. The frequency generators and synthesizer are referenced to a GPS-disciplined atomic Rb-clock.

second, intermediate repetition-rate lock of the FC laser is implemented as shown in Fig. 4.3. Initially, the FC laser is referenced to the MHz-generator (adjusted to exactly $1/76$ of the combined locking frequency of the DDS board and the GHz-generator) whose phase can straightforwardly be changed by a few π so that the temporal overlap between FC and pump pulses can always be obtained. After gradually changing from the MHz- to the GHz-lock (via the “switch” shown in Fig. 4.3), the temporal overlap between pump and seed can be fine-tuned via a physical translation stage of a few centimeters in the OPCPA.

4.2.4 The parametric amplifier

The three-stage (two crystals), narrowband OPCPA system consists of an unsaturated first pass followed by two saturated passes and produces amplified Ti:sapphire FC pulses of more than 5 mJ of pulse energy. The system, as shown in Fig. 4.4, is based on the design in [31]. First, part of the seed spectrum is selected via a movable slit in the Fourier plane of a 4f-grating stretcher. The combination of chirp and spectral clipping broadens the FC seed pulses to about 10 ps pulse duration. The seed

pulses are then amplified via a double pass (slightly displaced vertically) in a first, 5 mm thick BBO crystal to the $100 \mu\text{J}$ -level. Afterward the beam is blown up and further amplified to the mJ-level in a second, power amplifier BBO crystal of equal thickness. A grating compressor is used to recompress the pulses to a pulse duration of a few 100 fs.

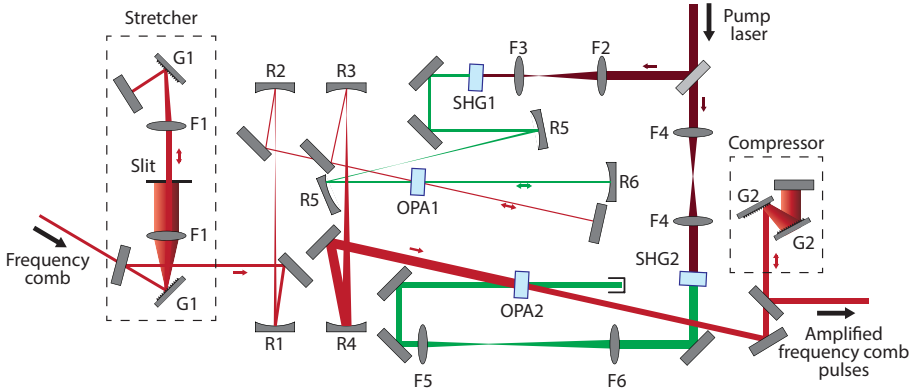


FIGURE 4.4: Schematic of the OPCPA system used to amplify the Ti:sapphire frequency comb pulses to the mJ-level. SHG: second-harmonic generation (KDP crystal), OPA: optical parametric amplification (BBO crystal), G1, G2: 1200 lines/mm grating, F1 = 20 cm (focal length), F2 = 55 cm, F3 = 15 cm, F4 = 75 cm, F5 = 40 cm, F6 = 60 cm, R1 = -60 cm (radius of curvature), R2 = -25 cm, R3 = -10 cm, R4 = -100 cm, R5 = -75 cm, R6 = -50 cm.

4.2.5 The phase-measurement setup

For measuring the phase influence of the parametric amplification process, the technique of linear interferometry is used in a Mach-Zehnder scheme as depicted in Fig. 4.1. To serve as a reference for the amplified FC pulses, 25% of the seed light of the FC oscillator is tapped off before the OPA and combined with a small fraction of the amplified pulses after the OPA; the path length for the reference pulses is adjusted so that they are delayed by about ~ 1 ps with respect to the amplified pulses. Figure 4.5 shows a more detailed overview of the phase-measurement setup which is based on the design described in [55, 93]. Before both the amplified and reference pulses are coupled into a large mode area fiber to assure spatial overlap, they are temporally broadened to about 400 fs by passing through 18 cm of F2 glass in order to reduce nonlin-

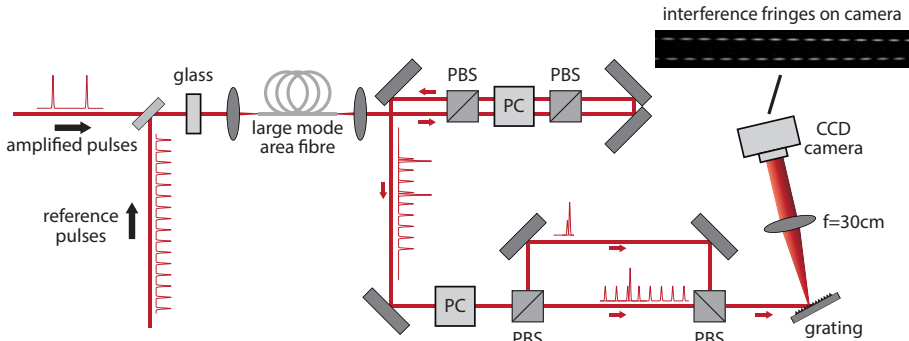


FIGURE 4.5: Schematic of the phase-measurement setup for measuring the phase influence of the parametric amplification process. The inset shows two experimentally obtained horizontal spectral interference patterns; for more details see the text. PBS: polarizing beam splitter cube, PC: Pockels cell.

ear effects in the fiber. For the suppression of unnecessary background light, a double-passed Pockels cell between two polarizers is employed to provide a high-contrast gate ($>10^4:1$) from before the first amplified pulse until the maximum delay time for which the phase shift is measured. A second Pockels cell followed by a polarizing beam splitter cube is then used to redirect part of the gated pulses to a small delay arm as visualized in Fig. 4.5. This way a small vertical offset can be introduced between the beams belonging to the first and the second amplified pulse, which are subsequently dispersed and focused on a CCD camera to obtain two vertically displaced spectral interference patterns (see the inset of Fig. 4.5). For each pattern, the average spectral phase is determined using a Fourier-transform based method [94]. Because of the different beam paths after the second Pockels cell, an additional phase shift is introduced. This issue, however, can be solved by adjusting the temporal gate of the second Pockels cell so that the beam paths for the first and second amplified pulses are swapped. As a result, the two interference pattern will exchange positions every time the Pockels cell is changed. In Fig. 4.6, a typical differential phase signal resulting from this alternating switching scheme is shown. By subtracting the measured differential phase of one switching state from the other (and dividing the result by two), the differential phase shift of the parametric amplifier is obtained.

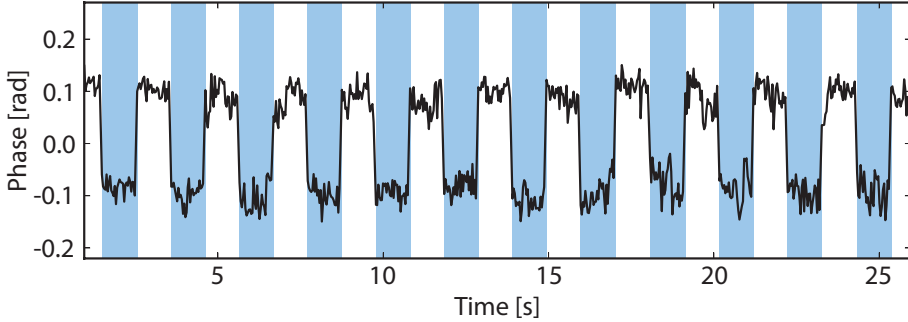


FIGURE 4.6: Typical measurement of the differential phase influence of the parametric amplifier. About once per second the optical paths of first and second pulses are alternated as highlighted by the shaded background.

4.3 Numerical simulations of a narrowband OPCPA system

Prior to quantitatively analyzing the amount of phase shift on the (FC) seed pulses in the OPCPA and the possible causes, it is instructive to investigate the influence of certain experimental parameters via numerical simulations. Therefore, a split-step method was used to numerically solve the coupled equations for the parametric amplification similar to the one described in [96] (see Sec. 2.5.1 for more details on the algorithm). In order to extract only the nonlinear phase caused by the parametric interaction, the linear phase originating from material dispersion was subtracted from the presented simulation results.

The parameters used in the simulation represent a typical operational condition of our three-stage OPCPA system. The signal (seed) beam was modeled as an initially 10 fs transform-limited Gaussian pulse, clipped to 6 nm bandwidth and centered around 780 nm. This pulse is stretched to about 10 ps duration by applying $690,000 \text{ fs}^2$ of group delay dispersion; the seed intensity was taken as 450 W/cm^2 . The pump pulses were assumed to be 58 ps Gaussian-shaped pulses with an intensity of 5.5 GW/cm^2 in the first two stages and 40% less in the third stage, respectively.

In Fig. 4.7(a), the spectral output intensity and phase is presented for four different pump intensities in steps of 0.1 GW/cm^2 . The characteristic peaks of the spectral intensity at the edges of the spectra are due to a combination of saturation effects in the parametric amplification

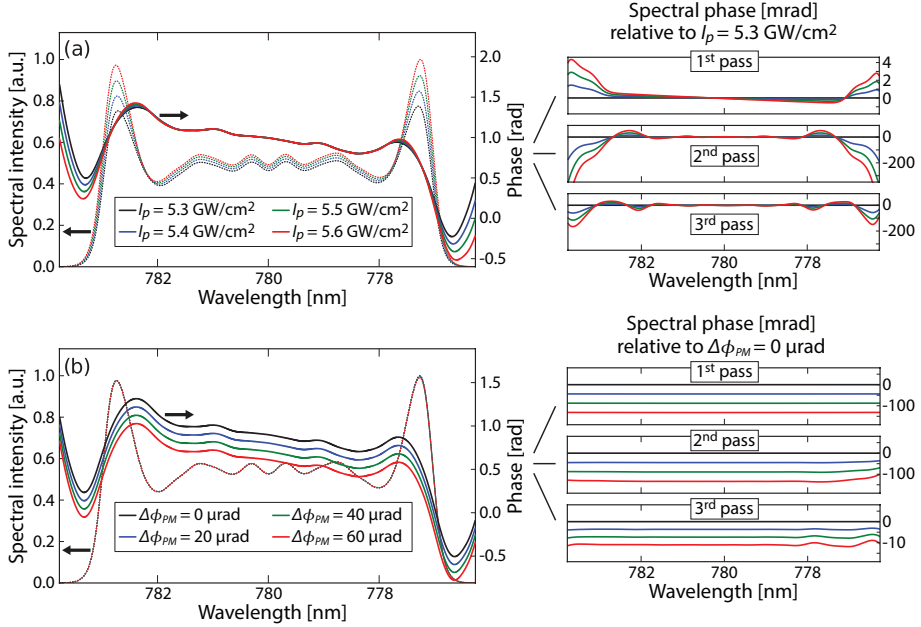


FIGURE 4.7: Simulation results for the investigated narrowband OPCPA system. (a) Resulting changes of the amplified spectra and the nonlinear phase due to variations in pump intensity. (b) Similarly for detuning the phase-matching angle from its initial value $\phi_{PM,0} = 2.30000^\circ$ while keeping the pump intensity fixed at $I_p = 5.5$ GW/cm². In the right column of the figure, the corresponding differential phase contributions from the individual OPCPA passes are shown.

process and the hard spectral clipping of the seed spectrum. It can be seen that although the intensity undergoes notable changes, the effect on the spectral phase is much less pronounced. Only in the spectral wing regions, the signal phases differ by more than several tens of milliradians. It should be noted that the spectral phases in the left column plots of Fig. 4.7 are simply the sum of the individually acquired spectral phases in the different OPCPA passes. The contributions from the individual passes are shown in the right column of the figure, where the spectral phase changes (relative to the obtained spectral phase for the lowest simulated pump intensity of $I_p = 5.3$ GW/cm²) have been plotted.

It is apparent from Fig. 4.7(a) that the applied changes in pump intensity hardly have any effect on the spectral phase after the unsaturated first pass (note the different y-axis scales). This effect can be understood by looking at the analytical expression for the change in

signal phase after parametric amplification in a crystal of length L [59]:

$$\Delta\phi_s(L) = \frac{\Delta k}{2} \int_0^L \frac{f_D(z)}{f_D(z) + \gamma_s^2} dz, \quad (4.2)$$

which depends on the detuning Δk from the ideal phase-matching condition, the pump depletion $f_D = 1 - I_p(z)/I_p(z=0)$ and the initial ratio of pump and seed intensity $\gamma_s^2 = \lambda_s I_s(z=0)/\lambda_p I_p(z=0)$; λ_s , I_s and λ_p , I_p are the intensities and center wavelengths of the signal and pump beams, respectively. In the unsaturated regime $\gamma_s^2 \ll f_D$, hence the integrand in Eq. (4.2) is close to unity and changes in the pump intensity have little effect on the amplified signal phase.

The influence of the initial signal (seed) intensity on the amplified spectra was found to be even significantly smaller than the influence of changes in pump intensity. A change of 5% in seed intensity caused a phase shift difference of ~ 1 mrad, hence phase shifts and phase jitter due to seed intensity fluctuations from the Ti:sapphire FC are typically not of a concern.

Equation (4.2) also suggests a linear dependence of the induced phase shift with changes of the phase mismatch Δk . Therefore, simulations were performed for different detunings of the phase matching relative to $\phi_{PM,0} = 2.30000^\circ$. As apparent from Fig. 4.7(b), changes on the order of a few tens of microradians can already cause significant (hundreds of milliradians) phase shifts over the entire spectrum, although the spectral intensity remains basically unaltered. Note that in the simulations the phase mismatch for the third pass was reduced by a factor of five with respect to the first two passes according to the five times larger pump beam and hence five times smaller wavefront deviations expected in the third pass of the OPCPA. This explains the smaller relative phase shifts in the third pass as seen from the individual contribution plots (right column of Fig. 4.7).

4.3.1 Cross- and self-phase modulation

Not included in the above simulations are the effects of self-phase modulation (SPM) and cross-phase modulation (XPM) between signal, pump and idler beams. These phase shifts can be estimated by calculating the

B-integral (type 1 phase-matching) in a crystal of length L [44]:

$$B_{tot} = B_{ss} + B_{ps} + B_{is} = \frac{2\pi}{\lambda_s} \int_0^L n_2 \left(I_s(z) + \frac{2}{3}I_p(z) + 2I_i(z) \right) dz. \quad (4.3)$$

In order to investigate their relative impact, the total value of the B-integral (B_{tot}) was split up into the contributions from the signal beam itself due to SPM (B_{ss}) and from the coupling of the pump and idler intensities with the signal beam via XPM (B_{ps} and B_{is} , respectively). Assuming a nonlinear coefficient of $n_2 = 4 \times 10^{-16} \text{cm}^2/\text{W}$ for BBO around the signal wavelength of 780 nm [97], this resulted in the phase shifts depicted in Fig. 4.8.

It can be seen that most of the phase shift is caused by XPM between the signal and pump beam where a change of 5% in pump intensity causes an additional phase shift of about 10 mrad of the amplified signal phase. Similar relative changes of the seeding intensity result in a two orders of magnitude lower phase shift and can therefore be neglected.

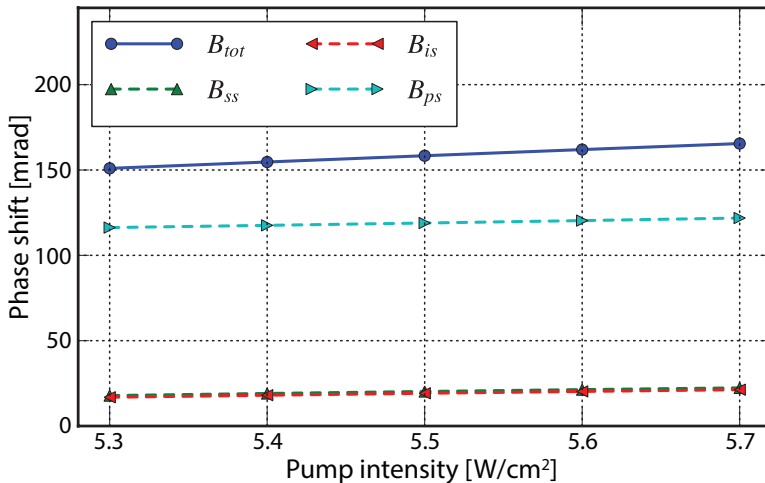


FIGURE 4.8: Calculated B-integral values of the three stage OPCPA for different pump intensities. Shown are the total value (B_{tot}) and the individual contributions from SPM of the signal beam (B_{ss}) and XPM between pump and signal (B_{ps}) and idler and signal beams (B_{is}).

4.4 Analysis of the pump pulse pair

As mentioned in Sec. 4.2, one of the main reasons for the development of the new pump frontend was to assure that all amplified pulses travel exactly the same optical path, which enables the production of pump pulse pairs with almost equal wavefronts. However, the high saturation level of the ultrahigh-gain pre-amplifier (net gain >70 dB) introduces the issue of temporal and spatial gain shaping. In this section, we discuss the influence of these shaping mechanisms as well as the direct measurement of the wavefront deviations within one pump pulse pair.

4.4.1 Temporal gain shaping

Because the first seed pulse takes out a significant part of the stored energy in the amplifier crystals, the gain of the amplifier becomes a function of time. The instantaneous gain $G(t)$ can be modeled as [47]:

$$G(t) = \frac{G_0}{G_0 - (G_0 - 1)\exp[-F_{in}(t)/F_{sat}]} \quad (4.4)$$

and depends on the undepleted gain factor G_0 , the saturation fluence of the amplifier crystal F_{sat} and the integrated input intensity I_{in} from a starting time t_0 up to the time t :

$$F_{in}(t) = \int_{t_0}^t I_{in}(t')dt'. \quad (4.5)$$

Figure 4.9 shows the calculated pulse shapes after the Nd:YVO₄ pre-amplifier ($F_{sat} = 170$ mJ/cm² and a total undepleted gain factor of $G_{0,tot} = 90$ dB) and after the double-pass flashlamp-pumped Nd:YAG post-amplifier ($F_{sat} = 650$ mJ/cm² and $G_{0,tot} = 25$ dB) for seeding energies at the pJ-level for the first stage. For simplification, a flat-top spatial distribution was assumed for the laser pulses and losses in the amplifier were neglected.

The effect of gain saturation is most apparent in the case of equal seeding energy into the pre-amplifier as seen in Fig. 4.9(a) where the amplified pulses differ greatly in intensity and shape. The most straightforward way to achieve equal peak intensities is to adjust the seeding energy (Fig. 4.9(b)), but the different gain dynamics result in a ~ 9 ps shift of the intensity maximum of the pulse. Since the repetition rate of the pump oscillator is synchronized to the Ti:sapphire FC, this shift

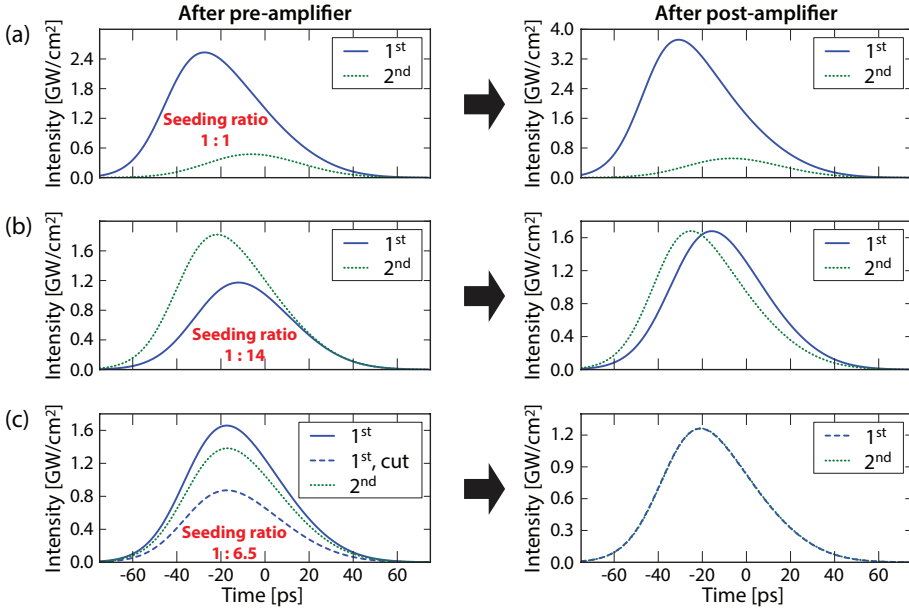


FIGURE 4.9: Calculated amplified pulse shapes for different seeding ratios (first : second) of the two pump pulses to obtain equal pulses after the post-amplifier. Each row shows the pulse shapes upon exiting the pre-amplifier (left column) and post-amplifier (right column). (a) Seeding pulses of equal energy. (b) 14 times higher seed energy for the second pulse. (c) 6.5 higher seed energy for the second pulse. In addition, the energy of the first pulse was reduced by 47% between the pre- and post-amplifier, which in the experiment is performed by a Pockels-cell pulse picker.

would cause the FC pulses to see different growth parts of the pump pulses in the OPCPA, thus experiencing different amplification.

However, the simulations indicate that this issue can be addressed by cutting away about half the energy of the first pulse after the pre-amplifier as seen in Fig. 4.9(c). This additional pulse shaping, in combination with adjustment of the seeding energies, allows the production of two almost identical amplified pulses despite the strong gain saturation. In the experimental setup, a fast Pockels-cell pulse picker is employed to reduce the pulse energy of the first pulse after the pre-amplifier (see Fig. 4.1).

4.4.2 Spatial gain shaping

The seed pulses for the pre-amplifier have a Gaussian-like spatial intensity distribution, hence the saturation of the amplifier will also cause spatial gain shaping. This means that the spatial profile will be distorted after amplification. Furthermore, since the first pulse takes out a significant part of the stored energy in the amplifier, the second pulse will be distorted differently due to a different spatial distribution of the remaining stored energy. The result can be seen in Fig. 4.10 where beam profiles of the first and second pulses after the post-amplifier (with different time delays of 40 ns and 400 ns) are shown.

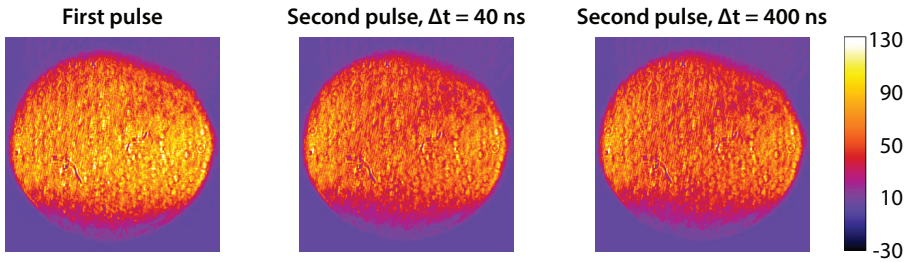


FIGURE 4.10: Amplified beam profiles of the first pulse and two second pulses with different time delays of 40 ns and 400 ns, respectively.

It is apparent that although the overall shape of the beam profiles are very similar (as expected since the pulses travel the same optical path in the amplifier), the intensity profiles of the first and second pulses can still differ significantly over the beam. Different pump intensities influence the phase of the amplified FC pulses as described in Sec. 4.3, thus the spatial gain shaping will cause a spatially dependent amplifier phase shift. However, Fig. 4.10 also shows that the spatial differences (and hence the induced spatially dependent phase shifts) basically remain constant with different time delays because the gain distribution after the first pulse hardly changes on a timescale less than one microsecond.

4.4.3 Wavefront differences

While relevant differences in spatial intensity distributions on the percent-level can be measured straightforwardly with a CCD-camera, it is experimentally challenging to measure wavefront deviations on the microradian-level. A Shack-Hartmann wavefront sensor was used in order to establish relative wavefront deviations between the first and a

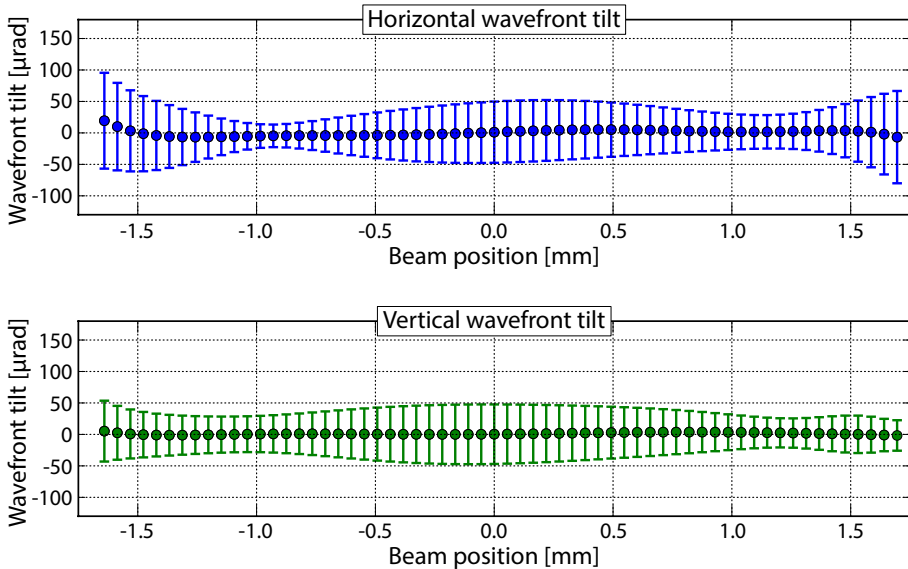


FIGURE 4.11: Relative horizontal and vertical wavefront tilts between the first and a second pump pulse at 40 ns inter-pulse delay based on an average of 40 acquisitions.

second pulse at a 40 ns inter-pulse delay. Figure 4.11 shows the obtained wavefront tilts in the horizontal and vertical direction across the beam as a result of an average of 40 single-shot acquisitions. It is apparent that the differential wavefront tilt is zero within the measurement uncertainty of about $50 \mu\text{rad}$. However, the measurement cannot detect wavefront tilts below tens of microradians, which can still influence the phase of the amplified FC pulses (see Sec. 4.3). In the next section, the phase shift is therefore quantified based on direct measurements using spectral interferometry.

4.5 Phase-measurements of the amplified frequency comb pulses

4.5.1 Phase shifts at different pulse delays

The ultimate test of the system is a direct measurement of the *differential* phase shift of the amplified FC comb pulse pairs after the OPCPA. Therefore, the spectral phase-measurement setup (see Sec. 4.2.5) was

used to determine this phase shift and its dependence on the inter-pulse delay. Figure 4.12 shows two of these measurements performed on different days and states of alignment of the OPCPA. During the phase measurement, the inter-pulse delay of the pump pulses was changed in steps of 80 ns and Fig. 4.12(b) shows the average differential phase shifts per pulse delay; the statistical uncertainty of the averaged value of ~ 10 mrad is mainly due to noise from the phase-measurement procedure itself. It can be seen that independent of the absolute differential phase shift, which is alignment-dependent and can be as big as a few hundred milliradians, the differential phase shift effectively remains the same for different inter-pulse delays. Together with the numerical simulations discussed in Sec. 4.3, this indicates that the average wavefront tilt between the first and the second pump pulse remains equal on a microradian-level, independent on the inter-pulse delay. Furthermore, if one assumes a linear relation between differential phase shift and inter-pulse delay, the statistical uncertainty of the phase measurement together with the maximum investigated pulse delay can be used to obtain an upper bound on the inter-pulse delay-dependent phase shift. According to Eq. (4.1), this potential systematic phase shift of ~ 10 mrad would correspond to a frequency error of less than 5 kHz at the fundamental laser frequency.

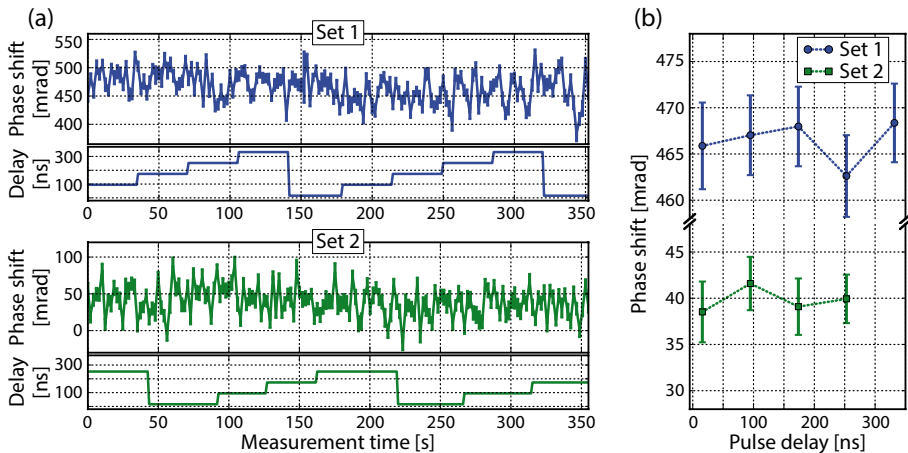


FIGURE 4.12: (a) Differential phase-shift measurements between two amplified FC comb pulses for two states of alignment of the OPCPA system (Set 1 and Set 2, respectively). During one measurement the inter-pulse delay was changed in steps of 80 ns. (b) Average phase shifts for each inter-pulse delay of these two measurement sets together with their statistical uncertainties.

However, if the same 10 mrad can be attained over a longer delay, then the corresponding uncertainty reduces even further with this delay. In order to investigate significantly longer pulse delays than the 336 ns presented in this paper, a rebuild of the phase-measurement setup is required, incorporating an additional Pockels cell to suppress the intermediate reference pulses. While not producing a spectral interference pattern, these pulses still contribute to the measurement noise by adding a constant background level to the interference signal and thus limiting the investigated delays to a few hundred nanoseconds.

4.5.2 Phase-shift scaling with amplified pulse ratio

From the simulations discussed in Sec. 4.3 it is clear that for a constant differential phase shift of the amplified FC pulses a stable intensity ratio of the pump pulse pair is essential. Therefore, the pump-pulse-intensity ratio (and hence the ratio of the amplified FC pulses) was changed while measuring the differential amplifier phase shift for a constant inter-pulse delay as before. Figure 4.13 shows such a measurement for a certain amplifier alignment stage together with a linear fit of the experimental data points. In general, the linear scaling coefficient is typically on the order of a few mrad per 1% pulse-energy difference. Thus for minimizing phase-shift deviations below 10 mrad rms, the amplified pulse-energy ratio needs to be actively stabilized. Experimentally, this is achieved by using the Pockels-cell unit in between the pre- and post-amplifier (see Sec. 4.2) in a simple feedback loop, performing small adjustments on the seed energy ratio for the post-amplifier.

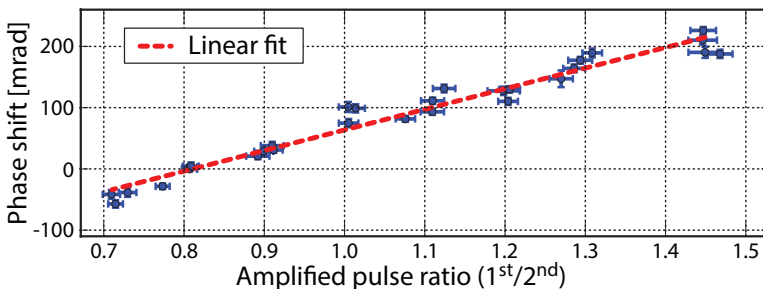


FIGURE 4.13: Differential phase shift of the FC pulses in the OPCPA versus amplified pulse-energy ratio. The scaling coefficient of the phase shift based on the linear fit is 3.3 mrad / 1% energy-ratio difference.

4.5.3 Spatial dependence of the phase shift

In order to examine the spatial dependence of the measured phase shifts, a pinhole was used to select different spatial parts of the amplified FC pulses (see Fig. 4.14, inset). For each subsection, a short phase measurement was then carried out while switching the inter-pulse delay. As can be seen from Fig. 4.14, the phase shift can differ by ~ 100 mrad for different parts of the amplified FC pulses. These deviations are mainly attributed to the different spatial intensity profiles of the first and second pump pulses (see Fig. 4.10). In addition, nonlinear effects such as SPM can already have an influence in the last stages of the pre- and post-amplifier of the pump laser. This can potentially cause slight (few μrad) wavefront differences between the first and second pump pulses due to different intensity profiles, which in turn could lead to phase shifts in the amplified FC pulses. However, when the amplified pulses

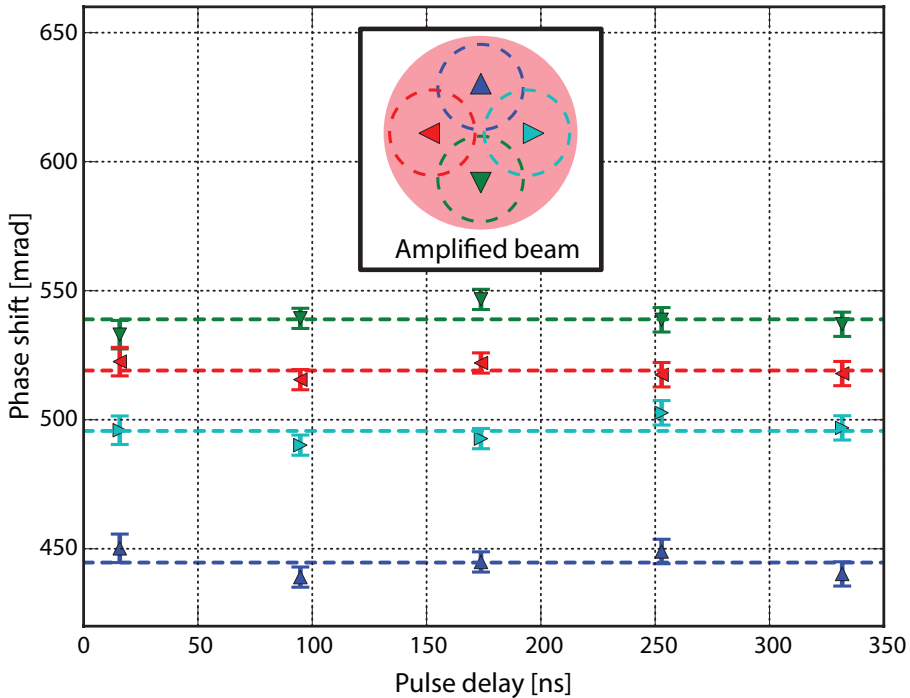


FIGURE 4.14: Phase-shift measurements of different spatial subsections of the amplified FC pulses as schematically depicted in the inset. The dashed lines represent the average phase shift per subsection.

are used for a spectroscopic experiment, typically only the average spatial phase shift matters so that the measured spatial variations will at most cause a slight reduction in contrast of the measured Ramsey-like signals. More important, Fig. 4.14 also shows that for the individual subsections there is again no observed dependence (within the measurement uncertainty of 10 mrad) between the measured phase shift at different time delays, which is the most important prerequisite for precision Ramsey-comb spectroscopy.

4.6 Conclusion

The presented OPCPA system produces FC pulse pairs of more than 5 millijoule pulse energy and with a programmable inter-pulse delay of multiples of the cavity round-trip time of the master oscillators (currently 8 ns). We have investigated the phase coherence of these pulse pairs up to hundreds of nanoseconds, but an extension to even tens of microseconds seems feasible. With the help of numerical simulations and an experimental investigation it was established that despite absolute differential phase shifts of up to a few hundred milliradians (depending on the amplifier alignment), the differential phase shift remains constant within at least 10 mrad given a straightforward active stabilization of the pulse-intensity ratio. In addition, within the measurement uncertainty of about 10 mrad, no dependence of the differential phase shifts on the inter-pulse delay could be observed. Given this uncertainty as an upper bound for a potential phase shift, we estimate a maximum frequency error of 5 kHz in a Ramsey-type measurement (at the fundamental wavelength of the Ti:sapphire FC). However, this upper bound was derived from a noise-limited measurement over a maximum inter-pulse delay of 336 ns. A phase measurement over longer pulse delays (such as microseconds) could potentially reduce this value proportionally to the delay time.

Furthermore, the new possibility to obtain Ramsey-like signals at programmable delays could also be used to measure multiple transitions at the same time. Similar to the well-known technique of Fourier-transform spectroscopy [98, 99], complex excitation spectra can be retrieved from the combined Ramsey signals via a Fourier transform. Together with nonlinear upconversion of the amplified FC comb pulses, the combined Ramsey signals will potentially enable multi-transition Ramsey-like spectroscopy in the extreme ultraviolet at the kHz-level.

CHAPTER 5

RAMSEY-COMB SPECTROSCOPY WITH INTENSE ULTRASHORT LASER PULSES

5.1 Introduction

Optical frequency combs (FCs) based on mode-locked lasers have revolutionized the field of metrology and precision spectroscopy by providing precisely calibrated optical frequencies and coherent pulse trains [24, 29]. Amplification of the pulsed output from these lasers is very desirable as nonlinear processes can then be employed to cover a much wider range of transitions and wavelengths for ultrahigh precision, direct FC spectroscopy [27, 100]. Therefore, full repetition rate laser amplifiers [35, 36] and enhancement resonators [38, 39] have been employed to produce up to microjoule-level pulse energies [40]. Here we present a spectroscopy method to obtain FC accuracy and resolution by using only two FC pulses amplified to the millijoule pulse-energy level, orders of magnitude more energetic than what has previously been possible. The new properties of this approach, such as cancellation of optical light-shift effects, are demonstrated on weak two-photon transitions in atomic rubidium and cesium thereby improving the frequency accuracy up to thirty times. As an alternative to full repetition rate amplification and cavity enhancement of FCs, direct amplification of selected FC pulses allows for much higher pulse energies and wavelength tunability. By amplifying two FC pulses and subsequent harmonic upconversion, precision spectroscopy in the extreme ultraviolet near 51 nm has been demonstrated [31]. However, in [31] the FC resolution was sacrificed because only two consecutive FC pulses could be amplified, and phase shift effects during the amplification process compromised the FC accuracy. To realize both FC resolution and accuracy in conjunction with mJ pulse energies, we developed the method of Ramsey-comb spectroscopy. This method is based

on a series of excitations with two selectively amplified FC laser pulses, which can be varied in delay over a wide range without affecting the optical phase. The result is a form of spectroscopy that is related yet fundamentally different to normal FC spectroscopy as we will discuss in the following chapter.

5.2 Principle of Ramsey-comb spectroscopy

Traditionally, excitation of atoms or molecules with two short and phase-coherent laser pulses is known as Ramsey spectroscopy [2, 37]. The pulses induce two excitation contributions that interfere depending on the delay time (Δt) and a possible additional phase shift between the pulses ($\Delta\phi$, e.g. from a pulse-amplification process). For a two-level atom with transition frequency f_k , the excited state population will exhibit an oscillatory behavior when Δt is changed, proportional to $1 + \cos(2\pi f_k \Delta t + \Delta\phi)$ (see Fig. 5.1(a) and Fig. 5.4 in the Supplementary information Sec. 5.6). If this signal is measured over a few oscillation periods as a function of Δt (a Ramsey scan), then the transition frequency can be determined very precisely provided that Δt and $\Delta\phi$ are known. A larger Δt leads to a more accurate determination of the transition frequency f_k . However, Ramsey spectroscopy based on a single scan can only measure one isolated transition at a time, and is sensitive to errors in $\Delta\phi$ [31].

Instead, in Ramsey-comb spectroscopy, a series of individual Ramsey scans are performed using coherently-amplified pulse pairs derived from a FC laser. The coarse delay of the pulse pairs can be changed in steps of the FC repetition time T . At each macro-delay step, the delay is fine-tuned to record a short Ramsey scan. As a result, we obtain a “comb” of Ramsey signals with three fundamental properties. First, the FC provides a precisely calibrated absolute time axis and phase control over a wide range of pulse delays ($>$ microseconds), thus enabling a very precise frequency determination. Second, if a constant phase shift $\Delta\phi$ affects the Ramsey signals, then it can be identified as a common effect in all the signals recorded at different time delays. It therefore drops out of the analysis and the full FC accuracy is recovered. Note that this includes light-induced phase shifts due to AC-Stark and similar effects [101], which often lead to frequency errors in (FC) spectroscopy. Third, by probing the excited state population over longer periods, multiple transitions can be measured simultaneously by observing a beating between the individual cosine contributions from each resonance at fre-

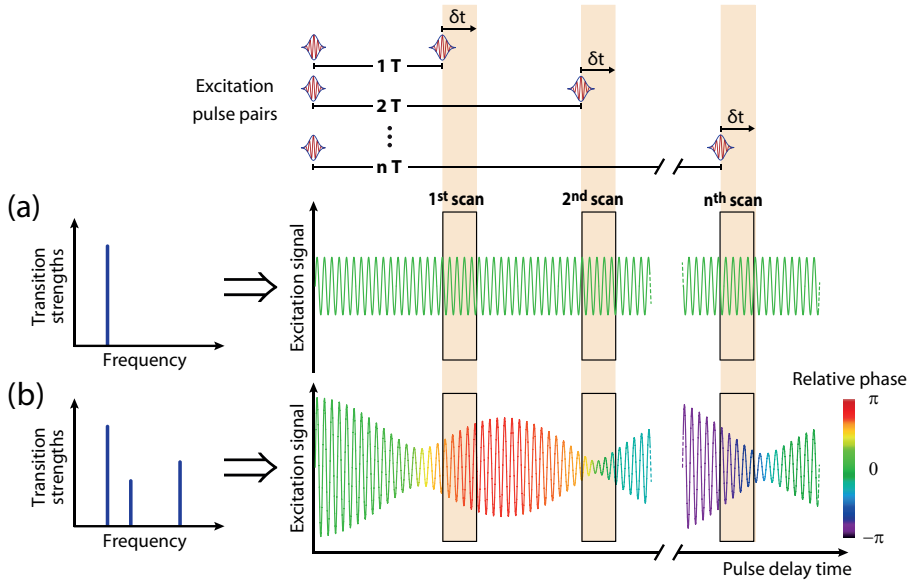


FIGURE 5.1: The principle of Ramsey-comb spectroscopy. An atomic system is excited with two coherent laser pulses at a widely tunable and accurate delay provided by a frequency comb. The laser pulses sample the excited population signal by a short Ramsey scan over δt at macro delays that are an integer (n) multiple of the comb repetition time T . From these scans the transition frequencies and strengths can be reconstructed with high precision. (a) In the case of only one resonance, the excitation signal undergoes a single cosine modulation of constant amplitude known as Ramsey fringes. (b) If multiple transitions are excited simultaneously, the resulting signal will exhibit complex amplitude and phase patterns. The phase evolution is visualized in color relative to the single transition in part (a).

quency f_k with transition strength A_k . The multi-transition signal will be proportional to:

$$S = \sum_k A_k [1 + \cos(2\pi f_k \Delta t + \Delta\phi)] \quad (5.1)$$

As an example, the expected upper-state population signal for three transitions as a function of the inter-pulse delay is schematically depicted in Fig. 5.1(b). It can be seen that analogous to the superposition of sound waves from slightly detuned tuning forks, the excitation signal exhibits a characteristic beating pattern. The excitation oscillations are related to those observed in traditional Fourier-transform spectroscopy [99], or similar methods with pulsed lasers based on physical optical

delay lines [102, 103]. However, in Ramsey-comb spectroscopy the FC source provides an absolute time axis for the pulse delay Δt , and this for time scales many orders of magnitude larger than any physical delay line can provide. Moreover, the individually acquired Ramsey scans result in accurate information on the phase of the complex delay-dependent signal as visualized by the color gradient of the signal trace in Fig. 5.1(b). This phase information is robust against fluctuations of signal strength and encodes both the transition frequencies and strengths. The underlying resonances can therefore be obtained very accurately from a straightforward fit of the phase according to Eq. (5.1) without complications introduced by line shapes in the frequency domain (more details on the fitting procedure is found in the Supplementary information Sec. 5.6). The frequency-domain spectrum can be calculated as well from the Ramsey scans by a discrete Fourier transform over all measured delay zones. These spectra are subtly different from normal FC spectroscopy but enable straightforward identification of the transitions and provide good starting values for the phase fit performed on Ramsey signals in the time domain (see Supplementary information Sec. 5.6).

5.3 Overview of the experimental setup

Experimentally, we obtain Ramsey-comb pulse pairs from a fully referenced Ti:sapphire FC laser, operating near 760 nm with a repetition rate of $f_{rep} \approx 128$ MHz. Two pulses from this comb laser are parametrically amplified more than a million times up to 5 mJ. The parametric amplifier supports broadband operation [72], but for this experiment only a 5 nm wide part of the spectrum is selected. The pulse delay of the amplified FC pulses is determined by the pump laser as visualized in Fig. 5.2. Only the FC pulses overlapping temporally with the high-energy pump pulses are amplified in the parametric amplifier. We verified that there is no delay-dependent phase shift introduced in the amplification process within an accuracy of $<1/1000$ of an optical cycle, based on spectral interferometry with the original FC pulses [104].

To demonstrate the capabilities of Ramsey-comb spectroscopy, the amplified FC pulse pairs are used to perform non-resonant two-photon spectroscopy in an atomic vapor cell (Fig. 5.2). Although the investigated transitions are very weak, no focusing of the laser beam (which has a diameter of 3 - 6 mm depending on experimental conditions) is required because of the high pulse energy. At every macro-delay step n ,

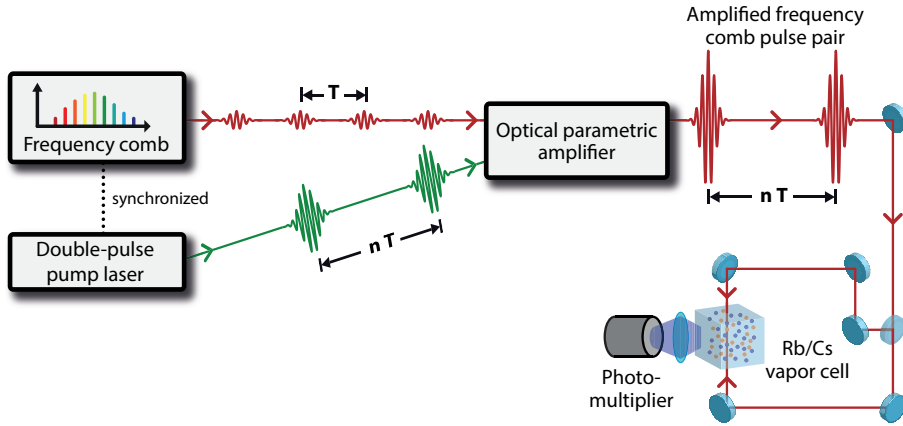


FIGURE 5.2: Schematic of the experimental setup. A high-energy pump pulse pair selectively amplifies two pulses from a frequency comb laser pulse train. The macro delay between the pump pulses and hence the amplified frequency comb pulses can be changed in steps of the cavity round-trip time $T = 7.8$ ns (where n is an integer number). The amplified pulse pairs are then split into counter-propagating copies to perform Doppler-reduced two-photon spectroscopy in a cell containing a mixture of atomic rubidium and cesium vapor. The signal is detected by monitoring fluorescence decay of excited atoms with a photo-multiplier tube.

the inter-pulse delay between the two amplified FC pulses is scanned in steps of a few hundred attoseconds. This results in Ramsey scans consisting of a few oscillations of the fluorescence signal, which is recorded with a photomultiplier. Further experimental details can be found in the Method Sec. 5.5.

5.4 Two-photon Ramsey-comb signals from rubidium and cesium

A typical measurement for rubidium and cesium is shown in Fig. 5.3; the signals are corrected for a constant background in the vertical direction. The change in Ramsey-signal amplitude between the macro-delay steps ($T = 7.8$ ns) is a direct result of the beating of the individual fluorescence signals from simultaneously excited transitions. Because these contrast changes appear on a nanosecond time scale, there is only a negligible effect on the signal amplitude within one Ramsey scan of ~ 3 fs length. For longer delays (higher n), there is an additional, general reduction in

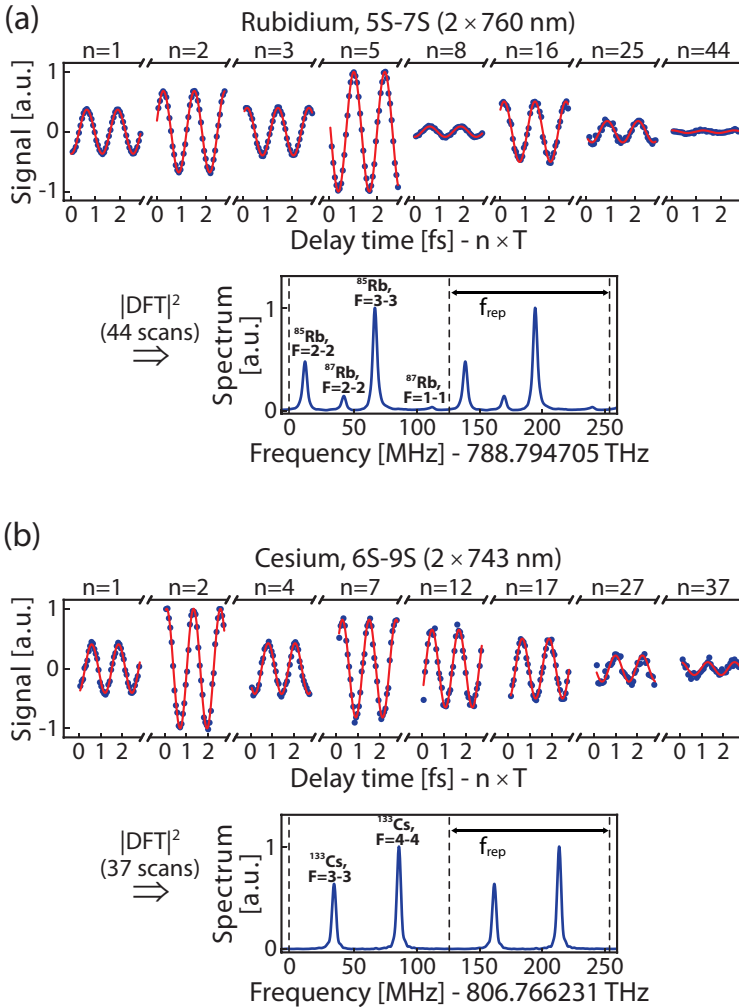


FIGURE 5.3: Experimental demonstration of Ramsey-comb spectroscopy. (a) Upper part: Selection of measured Ramsey-comb signals of the two-photon 5S-7S transitions in atomic ^{85}Rb and ^{87}Rb at macro delays of nT ($T = 7.837146$ ns). For each delay step n , the inter-pulse delay Δt was fine-adjusted over a range of $\delta t \approx 3$ fs to record a few oscillations of the signal beating pattern, such that $\Delta t = nT + \delta t$. The solid lines represent sinusoidal fits. Lower part: Calculated spectra based on the discrete Fourier transform (DFT) of the time-domain signal from a total of 44 Ramsey scans. (b) Similarly for the two-photon 6S-9S transition in ^{133}Cs ; the lower part shows the calculated spectra based on 37 Ramsey scans.

contrast due to the residual Doppler effect and spontaneous decay of the excited states. In the case of, e.g., rubidium, this limits the useable delay to about 345 ns ($n = 44$) due to the upper-state lifetime of 88 ns [105]. Note that the experimental system can produce pulse pairs with significantly longer delays well into the microsecond range, which enables much higher accuracy measurements given sufficiently narrow transitions (longer lifetimes); the increasing timing jitter of the FC seed oscillator for longer delays can efficiently be suppressed by directly locking the oscillator to a stable Hz-level reference laser [106].

Regarding the 5S-7S transition in ^{85}Rb , we arrive at the transition frequency before hyperfine splitting (“center of gravity frequencies”, f_{cog}) and hyperfine A constants of $f_{cog} = 788,796,960,604(5)$ kHz and $A_{7S} = 94,684(2)$ kHz (based on 28 datasets). For the same transition in ^{87}Rb we find $f_{cog} = 788,797,092,129(7)$ kHz and $A_{7S} = 319,762(6)$ kHz. The uncertainties are a combination of statistical and systematic errors (see Supplementary information Sec. 5.6 for more details). Because of small laser power drifts up to a few percent during the measurements, the AC-Stark (light) shift effect was not perfectly cancelled. However, still an effective ~ 50 times suppression was accomplished leading to only small residual AC-Stark shift corrections of a few kHz.

The measurements presented here are in good agreement with previous experiments [107, 108], and also of the same accuracy as the best determination recently obtained with full repetition rate comb excitation, employing strong focusing of the nJ-level laser pulses and coherent control [108]. This confirms that Ramsey-comb spectroscopy can be at least as accurate as full repetition rate FC spectroscopy but at many orders of magnitude higher pulse energy.

The advantage of having high pulse energies becomes apparent when Ramsey-comb spectroscopy is applied on much weaker transitions such as the investigated 6S-9S two-photon transition in ^{133}Cs . As can be seen in Fig. 5.3, a strong signal is obtained without any need for resonant enhancement by an intermediate level. From the analysis, we find $f_{cog} = 806,761,363,429(7)$ kHz and $A_{9S} = 109,999(3)$ kHz, which is thirty times more accurate than the best previous measurement on this transition [109], which was based on FC spectroscopy. The Ramsey-comb method, therefore, outperforms traditional forms of continuous-wave or FC laser spectroscopy on transitions that are too weak to be easily excited with unamplified FC pulses.

Based on parametric amplification, Ramsey-comb spectroscopy combines high frequency precision with wide wavelength coverage at mJ-level

pulse energy. Because of the high peak energy, the frequency range of this method can straightforwardly and efficiently be extended via nonlinear crystals to the ultraviolet, or with high-harmonic generation in a gas jet to the extreme ultraviolet [85] (taking $\Delta t > 100$ ns to avoid phase shifts from ionization in the gas jet). Therefore, there are many interesting targets for the Ramsey-comb method such as the 1S-2S two-photon transition in He^+ to provide new information on the proton-size puzzle [32, 110], or the two-photon X-EF transition in molecular hydrogen to put tighter constraints on speculative 5th forces beyond the Standard Model [30].

5.5 Methods: Further experimental details

The FC laser providing the seed pulses for the parametric amplifier is a home-built, Kerr-lens mode-locked Ti:sapphire oscillator. Both its repetition rate and carrier-envelope phase are locked to an atomic Rb-clock disciplined by the Global Positioning system (fractional inaccuracy better than 2×10^{-12} for averaging times larger than 100 s). The oscillator emits pulses of 6 nJ energy at a repetition time of 7.8 ns and with a spectral bandwidth of ~ 40 nm centered at 760 nm. Before amplification, the pulses are stretched to 10 ps by the combined effect of clipping the spectrum to about 5 nm around the desired wavelength and the application of $\sim 690,000$ fs² of group delay dispersion. The stretched FC pulses are selectively amplified in an optical parametric amplifier to the mJ-level by a high-energy 532 nm pump-pulse pair. The pump pulses originate from a separate, passively mode-locked Nd:YVO₄ oscillator, which is electronically synchronized to the Ti:sapphire FC oscillator at the same $f_{rep} \approx 128$ MHz. Via programmable pulse-pickers, two pulses are selected from the pump oscillator pulse train. These pulses are amplified to 40 mJ with an ultrahigh-gain Nd:YVO₄ pre-amplifier system [83, 91] and a Nd:YAG post amplifier, and subsequently frequency-doubled to 24 mJ at 532 nm. The parametric amplifier then produces amplified FC pulse pairs up to 5 mJ energy at a repetition frequency of 28 Hz, which therefore determines the repetition rate of the total experiment. During the amplification process, both pump pulses travel exactly the same optical path, assuring that their wavefronts are equal on a sub-milliradian level. This is essential because the parametric amplification is a highly-nonlinear process and the amplified signal phase is very sensitive to differences in wavefronts [104].

The Doppler-reduced two-photon spectroscopy is performed in a cell containing a mixture of rubidium and cesium vapor heated to $\sim 50^\circ\text{C}$. Because of the relatively broad excitation spectrum, the Doppler effect is not suppressed completely [108]. Background signal originating from single-sided excitation is strongly suppressed because of the chirp of the amplified FC pulses [111] combined with the use of quarter-wave plates to generate circular polarized light. The signal is proportional to the number of excited atoms as a function of inter-pulse delay and is recorded by monitoring the fluorescence decay (420 nm - 459 nm) to the ground state after the second excitation pulse.

5.6 Supplementary information

5.6.1 The atomic phase evolution

The time-domain analysis of Ramsey-comb spectroscopy relies on tracking the phase evolution of the recorded upper-state population signal. It is instructive to construct the multi-transition situation starting from the single resonance case, which simply exhibits a linear phase evolution (Fig. 5.4, first column). The second column of Fig. 5.4 depicts the situation when an equally strong second resonance is added. Now the superimposed signal exhibits a beating pattern, which results in phase jumps every time the signal envelope goes to zero. This phenomena is well-known from the field of acoustics, where the superposition of two similar acoustic frequencies (e.g., two slightly detuned tuning forks) produce a modulation of the sound amplitude according to the frequency difference of the involved sound waves. While in the special case of two transitions of equal amplitude the relative phase is still constant (apart from the periodic phase jumps), the situation changes when the spectral amplitudes are unequal (Fig. 5.4, third column). Finally, adding further transitions leads to a complex phase-evolution pattern as depicted in the last column of Fig. 5.4. In this characteristic phase trace, however, the full time-domain information of the signal is encoded. Thus measuring the phase evolution of the signal provides sufficient information for the synthesis of the spectral content.

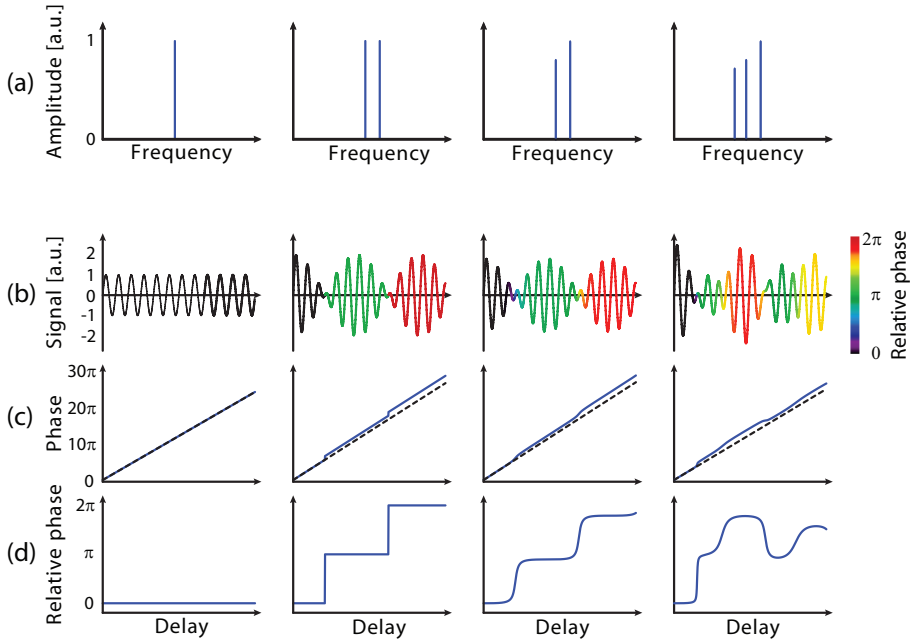


FIGURE 5.4: Visualization of the phase evolution of different beating patterns. Each column describes a different set of parameters. (a) Spectral amplitudes and frequencies of the atomic transitions. (b) Time-domain Ramsey signals for different delays of the excitation pulse pair. (c) Signal phase. The dashed line represents a linear reference phase. (d) Phase evolution relative to the reference phase.

5.6.2 Fitting the data: Time domain versus frequency domain

Most spectroscopic methods are based on data analysis in the frequency domain, which means that an optical excitation or absorption spectrum is fitted to obtain the transition frequencies of the excited resonances. In general, the spectral domain has the advantage that the individual resonances are, at least to some extent, decoupled if the spectral resolution is high enough. Also in Ramsey-comb spectroscopy the spectrum, as calculated from the time-domain Ramsey signals via a discrete Fourier-transform (DFT), can be used to extract the underlying resonances. However, the analytical description of the spectrum and hence the complexity of the fitting model greatly increases if more than one resonance is excited. This can be understood by looking at the analytical descrip-

tion for the calculated spectrum that can be derived with the help of basic signal processing theory [112]. For two resonances with transition frequencies f_1 , f_2 and amplitudes A_1 , A_2 , the analytical spectrum can be expressed as (for simplification, we neglect here the negative frequency components as well as the influence of the finite scanning length of the individual Ramsey zones):

$$|DFT(S)|^2 \propto ss_1^2 + ss_2^2 + \cos[(f_1 - f_2)(N + 1)\pi T] ss_1 ss_2 \quad (5.2)$$

with:

$$ss_k = A_k \frac{\sin[N\pi T(f - f_k)]}{\sin[\pi T(f - f_k)]}, \quad k = 1, 2. \quad (5.3)$$

The last term on the right side of Eq. (5.2) is due to the interference of the two transitions and depends on the maximum number of Ramsey zones N and the macro-delay step T . This additional interference term makes Ramsey-comb spectroscopy fundamentally different to, e.g., full repetition rate FC spectroscopy, which relies on the superposition of excitation amplitudes instead of the upper-state populations (proportional to the excitation amplitude squared) as for Ramsey-comb spectroscopy. In practice, spectral line-shaping mechanism such as a finite laser linewidth, lifetime and Doppler broadening further increase the complexity of these spectral interferences. For a more elaborate discussion of the analytical description see Ch. 6.

However, since both the transition frequencies and amplitudes are fully encoded in the phase evolution of the temporal signal, the fitting can be performed purely in the time domain without converting to the frequency domain. Note that the time-domain fit does not rely on amplitude information of the Ramsey signals but only on the experimentally more robust phase information. The fitting procedure is illustrated in Fig. 5.5. First, an arbitrary frequency f_{ref} is chosen as a reference close to the expected value of the measured resonances. The phase of each individual Ramsey zone is determined relative to the linear reference phase $2\pi f_{ref}\Delta t$ by sinusoidal fits of the experimentally obtained signals (Fig. 5.5).

These relative phases as a function of macro-delay steps are then fitted based on the phase of the analytical time-domain signal:

$$\begin{aligned} & \Phi_{fit}(\Delta t; A_1, A_2, \dots; f_1, f_2, \dots; \Delta\phi) \\ & = \arg \left\{ \sum_k A_k \exp(-i2\pi f_k \Delta t) \right\} + \Delta\phi - 2\pi f_{ref} \Delta t, \quad (5.4) \end{aligned}$$

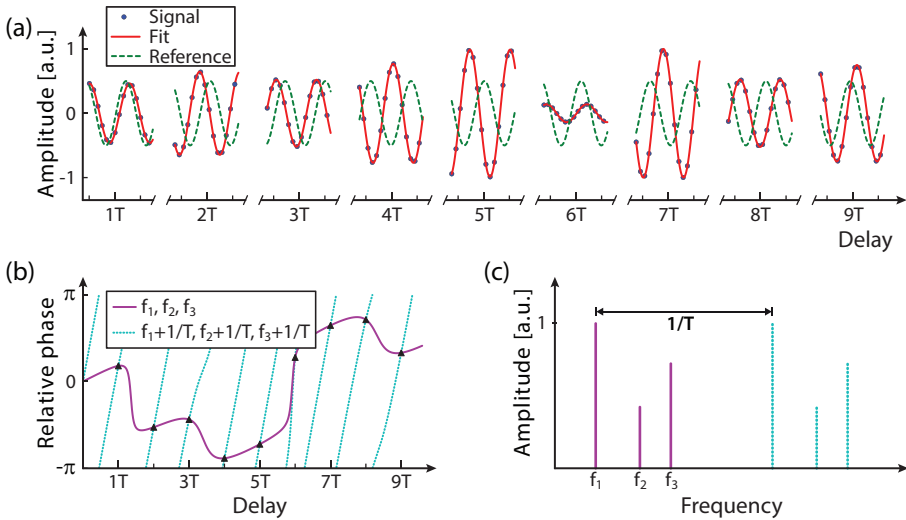


FIGURE 5.5: Visualization of the temporal-phase-fitting procedure. (a) Simulated signal (dots) together with a sinusoidal fit (solid line) and the fixed frequency reference trace (dashed line); T is the macro-delay step between the Ramsey zones. (b) Relative phase between the signal and the reference trace. Two possible fits for frequencies off by $1/T$ are shown. (c) Frequency-domain representation of the two possible outcomes from the phase fit.

including a potential, constant phase shift $\Delta\phi$ as an additional parameter. In the experiment, $\Delta\phi$ incorporates constant phase shifts that might occur during the parametric amplification (which can be as big as a few hundred mrad depending on the amplifier alignment) of the FC pulses. However, in Ramsey-comb spectroscopy even a common light shift (due to the AC-Stark effect) simply adds to $\Delta\phi$ and is therefore decoupled from the determination of the transition frequencies. This is a crucial feature since typically the light shift has to be quantized by repeating the measurement at different power levels and extrapolation to zero excitation power. Because the phase trace is not fully recorded but only sampled at certain inter-pulse delay steps spaced by T , the frequency can only be determined modulo $1/T$. As an example, Fig. 5.5(b) shows two groups of frequencies that fit the data equally well but differ by $1/T$ as depicted in Fig. 5.5(c). In general, this inherent ambiguity can always be solved by repeating the measurement at slightly different delay steps in case no previous measurements are available with sufficient accuracy.

5.6.3 Discussion of the spectroscopic results

The spectroscopic measurements were performed using two-photon excitation with counter-propagating lasers pulses of typically 5 nm bandwidth, chirped to 10 ps pulse duration. For most of the measurements, the originally mJ-level pulses were attenuated to a few 100 μJ of pulse energy using neutral grey filters as this was already sufficient and limited the residual AC-Stark effect. Because of the high energy, intensities of a few 100 MW/cm^2 were obtained despite the rather large beam diameters of 3 - 6 mm in the interaction region. A set of quarter-wave plates was used to adjust the polarization of both beams to be circular for a suppression of the one-sided excitation (in addition to the suppression effect from the pulse chirp). The spectroscopic target consisted of rubidium and cesium vapor in a cell (Toptica) heated to $\sim 50^\circ\text{C}$. The cell was not shielded against magnetic fields and was manufactured without the use of a buffer gas. In the presented experiment, three different atomic systems were investigated. Figure 5.6 schematically depicts their relevant energy levels. All examined transitions are electric-dipole forbidden between two S-states ($\Delta L = \Delta F = \Delta M_F = 0$), and are excited non-resonantly via two-photon excitation. The upper and lower energy levels are split up due to the hyperfine interaction and the transitions occur between hyperfine levels of the same F-number.

The obtained values for the investigated transitions are the result of averaging over 28 measurement sets (typical recording time for one set: 10 - 15 min). Within one measurement set, Ramsey fringes of at least 25 different macro-delays are recorded and the transition frequencies of rubidium or cesium are determined with the help of the previously

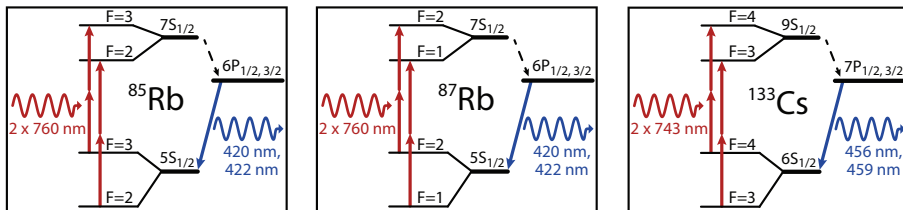


FIGURE 5.6: Level diagrams of the investigated transitions. The schematics show the relevant levels for the two rubidium isotopes (^{85}Rb and ^{87}Rb) and cesium (only one isotope, ^{133}Cs). Indicated are the excitation paths and the fluorescence light used for detection.

described time-domain fitting procedure. In Fig. 5.7, a typical example of such a phase fit is shown.

With the results from the time-domain phase fit we can simulate the expected Ramsey-signal traces, calculate the spectrum via a discrete Fourier transform and compare this simulated spectrum to the “experimental” spectrum calculated directly from the experimental Ramsey-signal traces. The time-domain fit discards amplitude information and, therefore, does not incorporate spectral line broadening effects as explained in the previous section. In the spectral domain, however, these effects need to be included to compare the “experimental” with the simulated spectra. Figure 5.8 shows such a comparison where a lifetime of 75 ns and a Doppler width of 2.3 MHz were assumed, both incorporated via a convolution of the simulated spectrum with the corresponding Lorentzian and Gaussian functions describing lifetime and Doppler

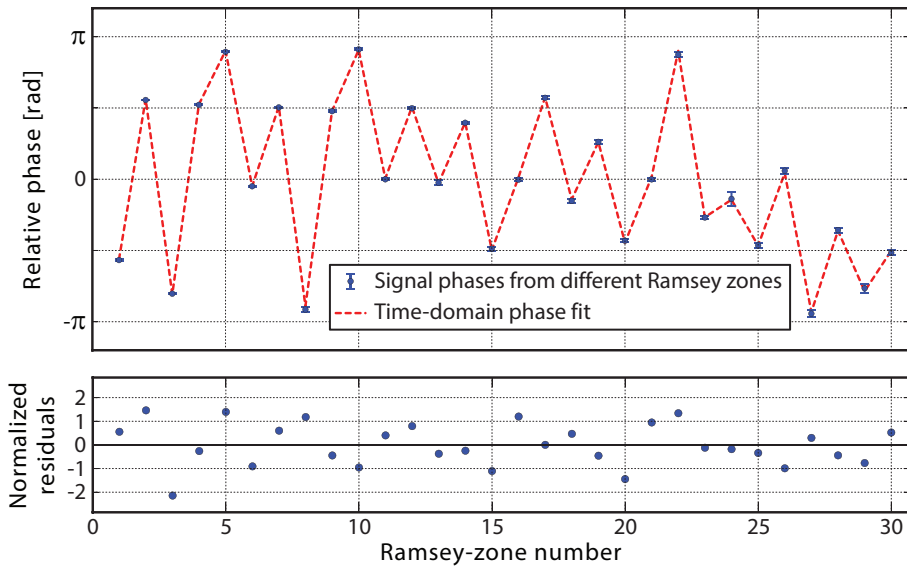


FIGURE 5.7: Example of a fitted phase trace from the rubidium measurement. The individual signal phases from different Ramsey zones are fitted simultaneously according to Eq. (5.4) as described in the text; the individual signal-phase uncertainties in particular for small zone numbers are too small to be seen on the graph’s scale. Note that the fit function is discrete and only defined for integer zone numbers, the dashed line is only drawn for visualization purposes. Also shown are the phase fit residuals, normalized to the signal-phase uncertainties.

broadening, respectively; the dataset is the same as used for Fig. 5.7. Note that the assumed values for the upper-state lifetime and Doppler width deviate from their real values as additional line-broadening mechanism as, e.g., the linewidth of the comb laser were not incorporated in the model. Nevertheless, the calculated spectrum shown in Fig. 5.8 provides a straightforward coarse check of the less intuitive graphical outcome of the temporal phase fit as shown in Fig. 5.7.

The resulting statistical uncertainties of the transition frequencies (from the time-domain phase fit) of each set are combined with a statistical uncertainty of 20 - 35 kHz, which accounts for random statistical phase shifts due to power fluctuations of the amplifier system. In order to give an example of the reproducibility of the measurement, Fig. 5.9 shows the individual measurement results for one of the rubidium transitions with datasets taken on four different measurement days. From a combined fit of these individual measurements, the final result (before

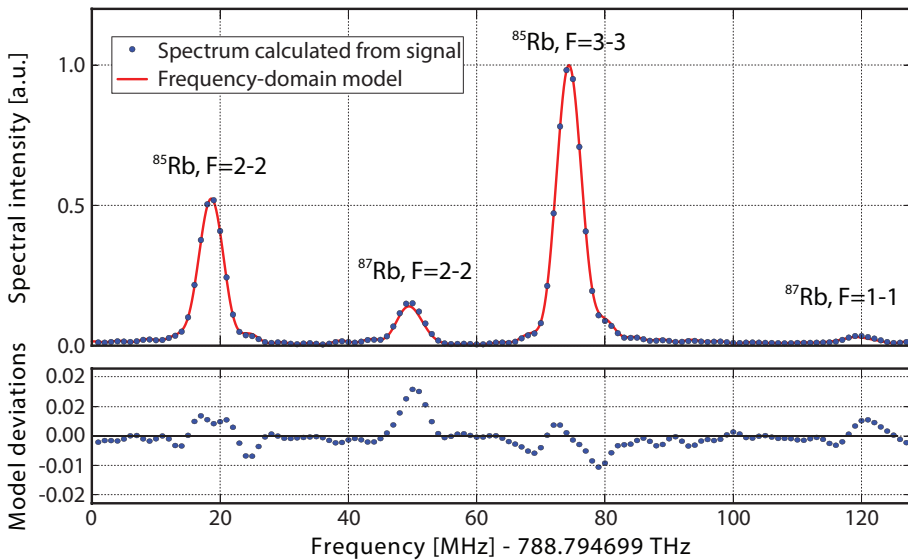


FIGURE 5.8: Comparison of the calculated signal spectrum with a simple spectral model. The model uses the transition frequency and amplitude results from the time-domain fit together with an assumed upper-state lifetime of 75 ns and Doppler width of 2.3 MHz to better match the calculated “experimental” spectrum (see the text for more details). Note that this spectral model was not used for the frequency determination, which was performed purely in the time domain.

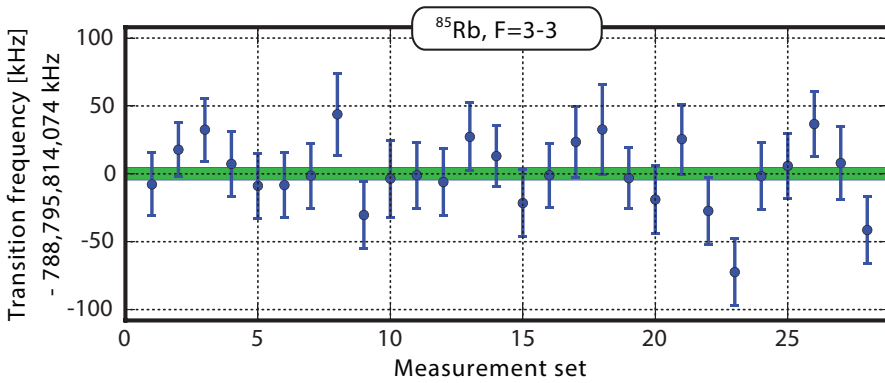


FIGURE 5.9: Individual frequency results for the ^{85}Rb F=3-3 transition. The values are given relative to the fitted average of the individual measurements and the shaded area represents the $1\text{-}\sigma$ confidence interval of this determination; the χ^2 divided by the number of degrees of freedom is 1.05.

correcting for systematic shifts) was obtained as well as an estimation of its statistical significance.

Similarly, all other measured transition frequencies were determined, leading to the results as shown in Tab. 5.1 (including the correction for systematic shifts). Also quoted in Tab. 5.1 are the commonly used transition frequencies before hyperfine interaction (“center-of-gravity frequency”) and the hyperfine splitting (A) constants, which are both calculated from the measured transition frequencies between the different F-states [113]. For rubidium, the isotope shift is derived as the difference of the center-of-gravity frequencies of the two isotopes.

5.6.3.1 Analysis of systematic effects

A range of systematic effects have been analyzed and taken into account. Table 5.2 summarizes the relevant systematic effects, which lead to the corrected results and systematic uncertainties that are shown in Tab. 5.1. In the following, we briefly discuss the characterization of the individual systematic effects.

Blackbody radiation. Dynamic Stark shifts due to blackbody radiation are estimated from extrapolating the calculations by Farley and Wing [114] to the measured temperature of the atomic vapor of $50(5)^\circ\text{C}$.

Frequency description		Final result [kHz]
⁸⁵ Rb, 5S _{1/2} - 7S _{1/2}	F=2 - F=2	788,798,565,751(6) _{stat} (4) _{sys}
	F=3 - F=3	788,795,814,071(5) _{stat} (4) _{sys}
	Centre of gravity	788,796,960,604(4) _{stat} (4) _{sys}
	Hyperfine A _{7S}	94,684(2) _{stat} (1) _{sys}
⁸⁷ Rb, 5S _{1/2} - 7S _{1/2}	F=1 - F=1	788,800,964,104(9) _{stat} (4) _{sys}
	F=2 - F=2	788,794,768,945(7) _{stat} (4) _{sys}
	Centre of gravity	788,797,092,129(6) _{stat} (4) _{sys}
	Hyperfine A _{7S}	319,762(6) _{stat} (1) _{sys}
	Isotope shift	131,525(7) _{stat} (3) _{sys}
¹³³ Cs, 6S _{1/2} - 9S _{1/2}	F=3 - F=3	806,766,286,786(8) _{stat} (4) _{sys}
	F=4 - F=4	806,757,534,152(7) _{stat} (4) _{sys}
	Centre of gravity	806,761,363,429(5) _{stat} (4) _{sys}
	Hyperfine A _{9S}	109,999(3) _{stat} (0) _{sys}

TABLE 5.1: Final spectroscopic results including the corrections for systematic shifts. The statistical and systematic uncertainties are shown in brackets (denoting the standard 68% confidence interval). Note that most of the systematic errors cancel when calculating the Hyperfine A constants resulting in small systematic uncertainties (<0.5 kHz for ¹³³Cs).

	⁸⁵ Rb		⁸⁷ Rb		¹³³ Cs	
	F2-2	F3-3	F1-1	F2-2	F3-3	F4-4
Blackbody radiation	-0.6(0.0)				-0.4(0.0)	
1st order Doppler effect	0.7(0.5)	0.1(0.5)	-0.4(0.5)	-1.8(0.5)	no effect	
2nd order Doppler shift	-0.4(0.0)				-0.2(0.0)	
2nd order Zeeman shift	-3.5(0.8)	2.5(0.6)	-1.7(0.4)	1.0(0.2)	-2.3(0.5)	1.8(0.4)
Pressure shift	1.5(2.7)				-0.6(3.0)	
Amplifier phase shift	0.0(2.5)				0.0(2.5)	
Residual AC-Stark	(1.0)*				(2.0)*	
Total	-2.2(3.9)	3.2(3.9)	-1.4(3.9)	-0.1(3.9)	-3.5(4.4)	0.5(4.4)

TABLE 5.2: Overview of the systematic shifts and uncertainties. All quoted values are in kHz. *For the AC-Stark shift effect only the uncertainty is given; each individual measurement set was corrected separately for the residual AC-Stark shift (see the explanation in the text).

Doppler shift. Because of the relatively broad excitation spectrum of about 5 nm bandwidth, the spectral line broadening due to the Doppler effect is not completely suppressed by the counter-propagating excitation scheme but only reduced to a few MHz. Nevertheless, because the spectroscopy was performed in a vapor cell with an isotropic atom-velocity distribution, the first-order Doppler shift still averages out. The second-order Doppler shift of the transition frequency f_k is calculated as $\delta f_k = f_k v^2 / 2c^2$ [115], where c is the speed of light and v is the average speed of the atoms (284(2) m/s for ^{85}Rb , 281(2) m/s for ^{87}Rb and 227(2) m/s for ^{133}Cs), based on the Boltzmann distribution for rubidium and cesium vapor at a temperature of 50(5) $^\circ\text{C}$. Although a common spectral line shape has no influence on the results, a difference in residual Doppler width can indirectly cause some small systematic shifts. This is the case for the two rubidium isotopes, which have a residual 1st order Doppler width that differs by about 1%. We simulated this effect taking into account the measurement conditions and the resulting shifts (on average <1 kHz) are shown in Tab. 5.2.

Magnetic (Zeeman) shift. The investigated S-S transitions are inherently insensitive to first-order magnetic shifts. The second-order magnetic shift depends on the hyperfine quantum number F and can be calculated using second-order perturbation theory [116, 117]. The shifts shown in Tab. 5.2 are based on a measured magnetic field of 0.85(0.10) G in the interaction zone of the gas cell. Because the accuracy of this calibration was sufficient as compared to the other systematic error sources, no attempt was made to suppress the magnetic field via shielding or external compensation.

Pressure shifts. The atomic vapor cell used in this experiment was manufactured without buffer gas. Nevertheless, in order to estimate potential frequency errors that depend on the atomic vapor pressure such as collisions between Rb and Cs atoms, potential background gases or impurities, the cell was temporarily heated to >110 $^\circ\text{C}$ resulting in a more than 100 times higher vapor pressures than typically used during the experiment. Based on frequency measurements at these high pressures (with reduced accuracy due to detrimental effects from the high vapor pressure), the potential frequency error was linearly extrapolated to the typical vapor pressure during the experiments according to a vapor temperature of 50(5) $^\circ\text{C}$.

Amplifier phase-shift error. In a separate measurement, we measured the potential delay dependency of the amplifier phase shift using spectral interferometry analogous to [104]. With the help of an improved measurement over $\Delta t_{max} = 625$ ns of inter-pulse delay (in [104] only pulse delays of ~ 330 ns were investigated), the amplifier phase shift was found to be constant within the accuracy of the phase measurement of $\delta\phi = 5$ mrad ($< 1/1000$ of an optical cycle). Assuming a linear relation between phase shift and delay, an upper bound for the potential frequency error can be calculated as $2\delta\phi/(2\pi\Delta t_{max}) = 2.5$ kHz; the additional factor 2 is because of the two-photon excitation. In case this potential frequency error becomes the limiting factor (e.g., when measuring much narrower transitions with longer upper-state lifetimes than the investigated cesium and rubidium transitions), the phase measurement can straightforwardly be extended with a small technical upgrade enabling longer pulse delays Δt_{max} well into the microsecond range [104].

Residual AC-Stark shift. Ramsey-comb spectroscopy is inherently insensitive to constant phase shifts, which also includes transition-independent AC-Stark shifts caused by the excitation pulses. However, if during one measurement set the absolute pulse energy of the excitation pulses systematically drifts, this can cause a small residual phase change and hence frequency errors. Therefore, we measured the phase shift a priori as a function of excitation pulse-energy for both rubidium and cesium. Together with the pulse-energy drift, which was obtained from a linear fit of the recorded pulse energies during the measurement, the individual fit results could then be corrected. The applied corrections were typically < 3 kHz for rubidium and < 6 kHz for cesium. We estimate the uncertainty of this residual AC-Stark shift correction to be 1.0 kHz in the case of rubidium and 2.0 kHz for cesium.

CHAPTER 6

RAMSEY-COMB SPECTROSCOPY: THEORY AND SIGNAL ANALYSIS

In the previous chapter, we demonstrated that the spectroscopic accuracy and resolution of optical frequency combs (FCs) can be obtained from a series of Ramsey-like measurements using only two amplified FC pulses at variable delays. In this chapter, we present a comprehensive analytical framework of this “Ramsey-comb” method, both in the time and frequency domains. It is shown that as opposed to traditional forms of spectroscopy, the signal analysis can be performed purely in the time domain based on the temporal phases of the individual Ramsey signals. We give a detailed description of the robust fitting algorithm relying solely on this phase information and discuss special features such as an insensitivity to (transition-independent) spectral line-broadening mechanisms and constant phase shifts due to, e.g., the AC-Stark effect from the excitation pulses themselves. The precision and resolution of the Ramsey-comb fitting method is assessed via numerical simulations, including cases of transition-dependent broadening mechanisms and phase shifts.

6.1 Introduction

Optical FCs based on mode-locked lasers have become an indispensable tool in many laboratories performing ultrahigh-precision frequency measurements [14, 15, 24, 29]. Because of their ability to link optical frequencies with radio frequencies from atomic clocks, FCs enable precise calibration of narrowband spectroscopy lasers leading to frequency measurements with up to 17 digit accuracy [25, 26]. Moreover, FCs themselves can be employed to perform direct FC spectroscopy [27, 28, 100, 118, 119]. Amplification of the pulsed output of

FCs is very desirable as it allows one to perform spectroscopy on weak (multi-photon) transitions and the deployment of nonlinear processes such as wavelength conversion to explore frequency ranges inaccessible to continuous-wave lasers. Full repetition rate amplifiers have been used to increase the pulse energy of, e.g., Ti:sapphire FC lasers [35] and Yb-fiber FCs [36]. Additionally, enhancement cavities can be employed to further increase the power level [38, 39] and pulse energies at the 10 μJ -level have recently been achieved with this method [40]. Producing higher energy FC pulses remains very challenging because of average power limitations and dispersion in the enhancement cavities. One way to circumvent this problem is the phase-coherent amplification of (two) selected pulses derived from a FC oscillator. We demonstrated amplification of such pulse pairs to the mJ-level, which allowed for efficient frequency conversion via high-harmonic generation in a gas jet and enabled precision spectroscopy in the extreme ultraviolet wavelength region at 51 nm [31]. However, with the experimental system in [31] only two consecutive FC pulses could be amplified. As a consequence, the Ramsey-type measurement could only record single isolated transitions and the accuracy was limited by phase shifts during the amplification and in the harmonic upconversion. We therefore developed a new system capable of producing amplified FC pulses at the mJ-level with inter-pulse delays that can be changed over a wide range (in steps of the cavity round-trip time of the FC) without affecting the optical phase [83, 91, 104]. The system provides the new possibility to record a *series* of Ramsey signals at different macro delays. This enables Ramsey-comb spectroscopy [120], which is related to yet fundamentally different from traditional Ramsey or standard direct FC spectroscopy.

In this chapter, we present an analytical framework of the Ramsey-comb method and introduce fitting models for both the spectral and time domains; the latter was used to obtain the high-accuracy frequency results in [120]. First, we recall the principle of quantum-interference excitation with laser pulse pairs in order to establish the basic concept for describing the multi-delay Ramsey-like signals. This concept is then extended to multiple transitions, and effects such as constant and time-dependent phase shifts as well as spectral line-broadening mechanisms are included. With the help of the developed framework, we then briefly introduce an approach to fit the spectrum as calculated from the Ramsey signals. Subsequently, we describe in detail the significantly more robust time-domain fitting procedure based on the combined fit of the individ-

ual Ramsey-signal phases. Finally, the performance of this phase-fitting procedure is evaluated on a range of simulated data series.

6.2 Analytical framework

6.2.1 Quantum-interference excitation with laser pulse pairs

Ramsey-comb spectroscopy is based on Ramsey’s method of separated oscillating fields [1, 2]. In the optical domain, it is performed by looking at the quantum-mechanical interference of atomic amplitudes created by excitation with resonant laser pulses (see, e.g., [8, 37]). Figure 6.1 shows a schematic visualization for an atomic system with an isolated transition. When a resonant laser pulse interacts with such a system, it creates a quantum-mechanical superposition of the lower and the upper state (with energies E_l and E_u , respectively). While the initial phase of the atomic superposition is determined by the laser-pulse carrier, it subsequently evolves with an angular frequency of $2\pi f_k = (E_u - E_l)/\hbar$, where \hbar is the reduced Planck constant. If after a certain delay time a second atomic superposition is created by another laser pulse, both superpositions will interfere depending on their relative phase resulting

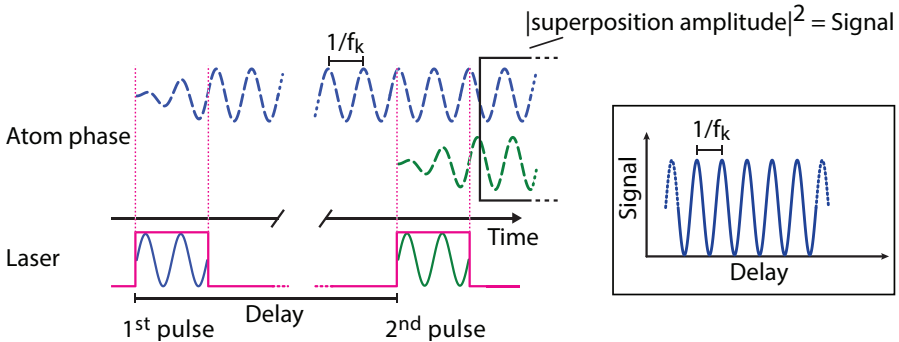


FIGURE 6.1: Visualization of the principle of quantum-interference excitation with laser pulses in the time domain. If a laser pulse resonantly excites an atomic transition, the quantum-mechanical phase of the excited atoms evolves according to the transition frequency of the atomic resonance $2\pi f_k$. If this process is repeated after a certain delay with a second laser pulse, the two atomic amplitudes will interfere. This results in a sinusoidal signal pattern (with a period of $1/f_k$; see the inset) as a function of the inter-pulse delay.

in an enhanced or decreased net amplitude of the atomic excitation. The squared absolute value of the resulting amplitude is proportional to the upper-state population of the atom and forms the experimental signal in Ramsey-type measurements. Based on the definitions used in [2], we take the excitation field as square light pulses with an electric field according to $\mathcal{E}(e^{i2\pi f_L t} + e^{-i2\pi f_L t})$, which act as an external dipole perturbation to a two-level system. An analytical description for the upper-state population \mathcal{P} after the second excitation pulse can be derived as [2, 121]:

$$\mathcal{P} = \frac{4\Omega_R^2}{b^2} \sin^2(b\tau_p) \left\{ \cos(b\tau_p) \cos \left[\frac{2\pi(f_k - f_L)t_{free} - \delta_{ex}}{2} \right] - \frac{\pi(f_k - f_L)}{b} \sin(b\tau_p) \sin \left[\frac{2\pi(f_k - f_L)t_{free} - \delta_{ex}}{2} \right] \right\}^2, \quad (6.1)$$

where τ_p is the duration of the square excitation pulses, t_{free} is the duration of the field-free evolution in between the two pulsed excitations, $\Omega_R = \mathbf{d} \cdot \mathcal{E}/\hbar$ is the so-called Rabi frequency (which in turn depends on the electric dipole operator \mathbf{d}),

$$b = \sqrt{\Omega_R^2 + \pi^2(f_k - f_L)^2} \quad (6.2)$$

is known as the Rabi flopping frequency, and δ_{ex} is a possible phase shift between the two excitation fields [3]. We now want to cast Eq. (6.1) in a form more convenient for describing Ramsey signals from laser-pulse excitation. In Ramsey's original derivation, t_{free} denotes the time in between the two excitation zones, while for laser excitation typically the time interval (pulse delay) Δt from the center of the first to the center of the second laser pulse is used, hence $\Delta t = t_{free} + \tau_p$ (see Fig. 6.2 for a visualization of Δt , t_{free} and τ_p). This substitution causes an additional phase term of $\pi(f_k - f_L)\tau_p$. Furthermore, traditionally, the detuning $f_k - f_L$ is changed to obtain Ramsey signals. In contrast, for pulsed laser excitation typically the (effective) relative phase δ_{ex} of the excitation pulses is changed. The latter can be done, e.g., by varying the pulse delay Δt via small adjustments of the laser repetition rate f_{rep} (while keeping the carrier-envelope phase offset fixed). This induces an effective phase change between the excitation zones according to $\delta_{ex} = -2\pi f_L \Delta t$ as visualized in Fig. 6.2. With the help of some basic trigonometric relations, we can now transform Eq. (6.1) into a compact form describing the optical Ramsey signal (at frequency $2\pi f_k$, see Fig. 6.1) as a function of the pulse-to-pulse delay time Δt as:

$$\mathcal{P} = A [1 + \cos(2\pi f_k \Delta t + \theta)], \quad (6.3)$$

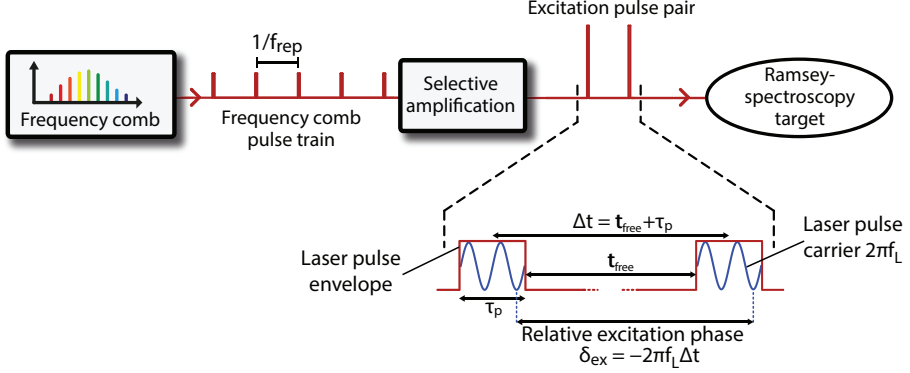


FIGURE 6.2: Optical Ramsey spectroscopy requires a laser pulse pair with a controlled inter-pulse delay and carrier-envelope phase, which can be achieved by selectively amplifying two pulses from a frequency comb laser. To measure Ramsey-like signals, the time delay Δt , and therefore the effective relative phase of the two amplified pulses δ_{ex} can be adjusted via small changes of the frequency comb repetition rate f_{rep} .

with the amplitude:

$$A = \frac{2\Omega_R^2}{b^2} \sin^2(b\tau_p) \left\{ \cos^2(b\tau_p) + \left[\frac{\pi(f_k - f_L)}{b} \right]^2 \sin^2(b\tau_p) \right\} \quad (6.4)$$

and the constant (delay-independent) phase term:

$$\theta = -2\pi\tau_p(f_k - f_L) + 2 \tan^{-1} \left[\frac{\pi(f_k - f_L)}{b} \tan(b\tau_p) \right]. \quad (6.5)$$

For zero detuning between laser and transition frequency ($f_k = f_L$) it can be seen that $\theta = 0$. For non-zero detuning and in the low-power regime ($\Omega_R \ll |f_k - f_L|$) one can approximate $b \approx \pi(f_k - f_L)$, which also leads to $\theta = 0$. For these cases, one obtains the well-known expression describing optical ‘‘Ramsey fringes’’ (see, e.g., [8]):

$$\mathcal{P} = A_k [1 + \cos(2\pi f_k \Delta t)] = \frac{A_k}{2} \cos^2(\pi f_k \Delta t), \quad (6.6)$$

with:

$$A_k := 2 \sin^2(\Omega_R \tau_p) \cos^2(\Omega_R \tau_p). \quad (6.7)$$

However, $\Omega_R \ll |f_k - f_L|$ does not hold in general, in particular when a sizable excitation probability is involved. Therefore, we perform a Taylor-expansion of θ around $\tau_p = 0$:

$$\theta = \frac{2\pi}{3} \Omega_R^2 (f_k - f_L) \tau_p^3 + O(\tau_p^5). \quad (6.8)$$

We can expect the maximum possible detuning to be of the order of the spectral bandwidth of the pulse $\sim 1/\tau_p$, thus from the leading term in the Taylor-expansion we obtain:

$$|\theta| < \frac{2\pi}{3} (\tau_p \Omega_R)^2. \quad (6.9)$$

The phase shift θ is therefore small as long as $\tau_p \Omega_R \ll 1$ holds, which translates into a low fractional excitation rate from the lower to the upper state. However, $|f_k - f_L|$ is typically minimized when optimizing for the highest Ramsey-fringe amplitude A_k , resulting in a further suppression of the phase shift by the factor $\tau_p/|f_k - f_L|$ as compared to Eq. (6.9). Since θ scales with the intensity of the excitation pulses ($\propto \Omega_R^2$), the influence of θ is in practice usually included in the AC-Stark shift calibration of the coupling from additional, non-resonant levels. In fact, θ can be regarded as an AC-Stark shift on the resonant transition due to an asymmetric excitation spectrum.

In the discussed optical form of Ramsey spectroscopy based on excitations with coherent laser pulse pairs, usually only a few periods of the Ramsey signal \mathcal{P} are recorded. The transition frequency f_k can nevertheless be determined with high precision from Eq. (6.6) provided both the delay time Δt and θ (and additional potential phase shifts such as the previously mentioned AC-Stark shift) are known. It is the accuracy of these two parameters that often represents the limiting factor for the achievable accuracy of the frequency determination.

6.2.2 Combining Ramsey signals from different macro delays: Ramsey-comb spectroscopy

In traditional Ramsey spectroscopy as described previously, the transition frequency is determined via an effective extrapolation to zero delay and correction for potential phase shifts. However, the situation becomes fundamentally different if not one but multiple Ramsey-signal traces can be measured by changing the delay between the excitation pulses in macro-delay steps. In the following we will describe the relation

between the combined time-domain Ramsey signals and the resulting spectral features in the frequency domain. As shown in Fig. 6.3, combining the signal from N scans at regular intervals in steps of T leads (after Fourier transformation) to spectral features whose widths are similar to the width as obtained from a continuous signal trace of length NT . However, due to the subsampling, the spectral pattern repeats at positions equal to the inverse sampling steps $1/T = \langle f_{rep} \rangle$, where $\langle f_{rep} \rangle$ is the average value of f_{rep} during the Ramsey scans. In addition, the finite length δt of the individual scans gives rise to a further overall amplitude modulation of the spectrum. In order to analytically describe the combined Ramsey signals as sketched in Fig. 6.3, it is convenient to decompose the time-domain signal into two parts:

$$S_t = S_{t,k} \cdot W_t. \quad (6.10a)$$

The first part of Eq. (6.10a), $S_{t,k} = S_{t,k}(A_k, f_k, f_{rep}, \Delta t)$, describes the rapid oscillations at the optical transition frequency $2\pi f_k$, while the second part, $W_t = W_t(\delta t, N, T, \Delta t)$, is a macro window function, which depends on the Ramsey-scan interval δt , the time step between the scans T and the total delay span from the first to the last scan at a macro delay of NT , where N is the number of individual scans (see Fig. 6.3). The frequency-domain representation of the signal S_f can then be derived

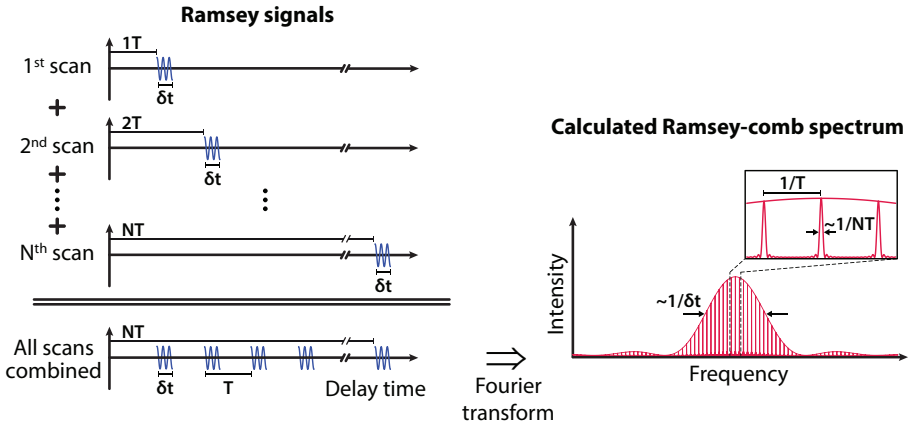


FIGURE 6.3: Individual Ramsey signals and the derived Ramsey-comb spectrum, which is calculated as the absolute value squared of the discrete Fourier transform of the combined time-domain signal. δt : individual scanning interval, T : macro-delay step between two Ramsey scans, N : number of scans.

via a convolution of the Fourier transformations of the two individual terms:

$$S_f = S_{f,k} \star W_f. \quad (6.10b)$$

In the time domain, the window function W_t consists of a series of rectangular envelopes ($\text{rect}(x) = 1$ for $|x| < 1/2$, and 0 otherwise), which can be converted to the frequency-domain representation W_f with the help of basic Fourier transformations:

$$W_t = \sum_{n=1}^N \text{rect} \left(\frac{\Delta t - nT}{\delta t} \right), \quad (6.11a)$$

$$W_f = \delta t \cdot \text{sinc}(f\delta t) \cdot \exp[-i(N+1)\pi T f] \cdot \frac{\sin(N\pi T f)}{\sin(\pi T f)}, \quad (6.11b)$$

with $\text{sinc}(x) = \sin(\pi x)/(\pi x)$. These window functions are combined with the part that depends on the transition frequency f_k , which in the case of a single resonance with a transition amplitude A_k can be written as (see Eq. (6.3)):

$$S_{t,k} = A_k \cos(2\pi f_k \Delta t), \quad (6.12a)$$

$$S_{f,k} = \frac{A_k}{2} [\delta(f - f_k) + \delta(f + f_k)]. \quad (6.12b)$$

Note that because in practice the constant offset of the measured Ramsey signals (see Eq. (6.3)) is typically removed by centering the signals around zero, we neglected it in Eq. (6.12b) and will continue so in the following derivations. In addition, we initially also refrain from including potential phase shifts between the excitation pulses such as θ .

Discarding negative frequencies*, we can define $S_{f,k}^+ := \frac{A}{2} \delta(f - f_k)$. We can then rewrite the expression for the spectrum as a superposition

*While in general the “leakage” of the negative frequencies diminishes with scanning longer individual Ramsey scans (longer δt), the influence of negative frequency components can also be minimized by an appropriate choice of the individual scanning interval δt . In order to make the overall envelope from the negative frequency components zero around the positive transition frequency, one has to ensure that $\sin(2f_k \delta t) \stackrel{!}{=} 0 \Leftrightarrow \delta t = u/(2f_k)$, with u being an integer. This translates into scanning a multiple of half-cycle Ramsey fringes at each macro-delay step.

of cosines of different harmonic orders:

$$\begin{aligned} |S_f^+|^2 &= |S_{f,k}^+ \star W_f|^2 \\ &= \left(\frac{A_k \delta t}{2}\right)^2 \text{sinc}^2[(f - f_k)\delta t] \\ &\quad \cdot \sum_{n=1}^N \{2(N - n)\cos[n2\pi T(f - f_k)] + 1\}, \end{aligned} \quad (6.13)$$

which resembles the spectra from FC pulse trains. However, note that in Ramsey-comb spectroscopy the temporal signal S_t is comprised of individual Ramsey-like measurements of the upper-state population of the atom. In contrast, the frequency-domain signal in traditional, full repetition rate FC spectroscopy is based on the coherent superposition of the upper-state amplitudes accumulated over many excitation pulses. This fundamental difference between these two techniques will become more apparent in the following section.

6.2.3 Extension to multiple transitions

Up to now we have considered only the case of a single resonant transition. When extended to M simultaneously excited transitions of amplitudes A_k and frequencies f_k , Eqs. (6.12a) and (6.12b) become:

$$S_{t,k} = \sum_{k=1}^M A_k \cos(2\pi f_k \Delta t), \quad (6.14a)$$

$$S_{f,k} = \sum_{k=1}^M \frac{A_k}{2} [\delta(f - f_k) + \delta(f + f_k)]. \quad (6.14b)$$

This assumes that coherent effects can be neglected in the measurement of the excited populations (e.g., by suppressing quantum beats in fluorescence detection by averaging the signal over long times compared to the beating period, or by ionization detection of the excited states).

The full expression for the spectral signal amplitude (restricted to positive frequencies) can then be written as:

$$\begin{aligned} S_f^+ &= \sum_{k=1}^M \frac{A_k \delta t}{2} \text{sinc}[(f - f_k)\delta t] \cdot \frac{\sin[N\pi T(f - f_k)]}{\sin[\pi T(f - f_k)]} \\ &\quad \cdot \exp[-i(N + 1)\pi T(f - f_k)]. \end{aligned} \quad (6.15)$$

Because of the transition-dependent phase terms, the spectrum (proportional to the absolute value squared of Eq. (6.15)) exhibits complex interferences. In order to see this more clearly, we limit ourselves to two transitions ($M = 2$), introduce the shorthand notation:

$$ss_{N,k}(f_k) := \frac{A_k \delta t \sin [N\pi T(f - f_k)]}{2 \sin [\pi T(f - f_k)]}, \quad (6.16)$$

and approximate:

$$\text{sinc} [(f - f_k)\delta t] \approx 1 \quad (6.17)$$

for $(f - f_k)\delta t \ll 1$. We can then write the positive-frequency spectrum in the compact form of:

$$\left| S_f^+ \right|^2 = ss_{N,1}^2 + ss_{N,2}^2 + 2\cos [(N + 1)\pi T(f_2 - f_1)] ss_{N,1} ss_{N,2}. \quad (6.18)$$

Apart from the linear superposition term $ss_{N,1}^2 + ss_{N,2}^2$, which would also be seen in traditional FC spectroscopy, there is an additional interference term that depends on $f_2 - f_1$, N and T . It is these interferences that complicate the frequency-domain analysis as will be shown in Sec. 6.3.1.

6.2.4 Constant phase shifts

We will now discuss the so far neglected possibility of additional phase shifts between the Ramsey scans of different macro delays. At first we consider the case of a potential constant (transition-independent) phase shift ϕ_c . With the inclusion of ϕ_c , Eqs. (6.14a) and (6.14b) become:

$$S_{t,k} = \sum_{k=1}^M A_k \cos (2\pi f_k \Delta t + \phi_c), \quad (6.19a)$$

$$S_{f,k} = \sum_{k=1}^M \frac{A_k}{2} [e^{i\phi_c} \delta(f - f_k) + e^{-i\phi_c} \delta(f + f_k)]. \quad (6.19b)$$

It is apparent that in the time domain a constant phase shift simply causes a global shift of all Ramsey scans together. However, this common shift does not influence the frequency of the Ramsey-fringes. This is even more obvious from the frequency-domain representation where the constant phase shift only produces an additional phase factor. When the (positive-frequency) spectrum is calculated, this phase factor simply

drops out as visualized in Fig. 6.4(a). The insensitivity to constant phase shifts fundamentally distinguishes Ramsey-comb spectroscopy from traditional Ramsey-type experiments where phase shifts of all kinds can cause frequency errors. This feature was particularly important for the high-accuracy Ramsey-comb spectroscopy based on amplified FC pulses in [120]; because the differential phase shift during the amplification process was constant (independent of the delay time), it did not affect the measurement accuracy in a significant way. Furthermore, in Ramsey-comb spectroscopy also the well-known light shift due to the AC-Stark effect from the excitation pulses themselves simply manifests itself as a constant phase shift of the Ramsey signal (as long as the energy of the excitation pulses is constant with respect to the delay time). Since in many practical cases such as the hyperfine transitions in cesium and rubidium measured in [120], this constant phase shift is common for the investigated transitions, it simply drops out in the analysis. Note that the same holds for shifts based on quantum-mechanical interference from off-resonance states, which do not scale with the power of the excitation

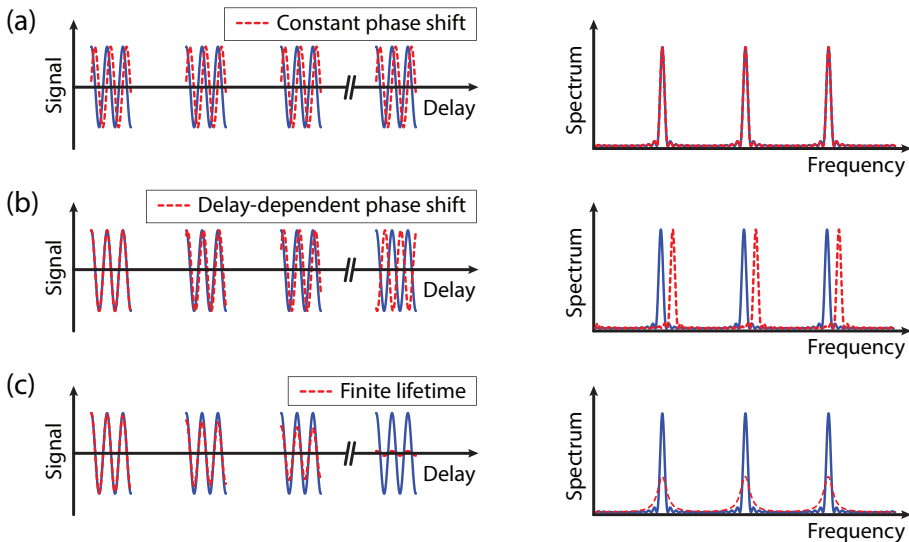


FIGURE 6.4: Influence of lifetime and phase-shift effects on the Ramsey-comb signals (single transition) and the corresponding spectra. (a) Constant phase shifts have no influence on the spectrum. (b) Delay-dependent phase shifts are translated into frequency shifts. (c) Exponential decay due to the finite upper-state lifetime leads to spectral line-broadening but does not shift the line positions.

pulses and therefore cannot be determined in the traditional way by repeated measurements at different power levels [101].

6.2.5 Time-dependent phase shifts

Although Ramsey-comb spectroscopy is insensitive to common constant phase shifts as discussed previously, the observed frequencies are altered by phase shifts that depend on the delay time between the two excitation pulses. The most simple case comprises a phase shift that is linear in time and can be described as (ϕ_T denotes a delay-independent constant):

$$\phi_t = \Delta t \frac{\phi_T}{T}. \quad (6.20)$$

Setting $\phi_c = 0$ for simplicity, Eqs. (6.14a) and (6.14b) then become:

$$\begin{aligned} S_{t,k} &= \sum_{k=1}^M A_k \cos(2\pi f_k \Delta t + \phi_t) \\ &= \sum_{k=1}^M A_k \cos \left[2\pi \left(f_k + \frac{\phi_T}{2\pi T} \right) \Delta t \right], \end{aligned} \quad (6.21a)$$

$$\begin{aligned} S_{f,k} &= \sum_{k=1}^M \frac{A_k}{2} \left\{ \delta \left[f - \left(f_k + \frac{\phi_T}{2\pi T} \right) \right] \right. \\ &\quad \left. + \delta \left[f + \left(f_k + \frac{\phi_T}{2\pi T} \right) \right] \right\}. \end{aligned} \quad (6.21b)$$

The result is an effective frequency shift of $\phi_T/(2\pi T)$, which is schematically depicted in Fig. 6.4(b). For a correct interpretation of the Ramsey-comb frequency results it is therefore of vital importance to accurately characterize potential delay-dependent phase shifts. One candidate of such a phase shift typical for spectroscopy relying on FCs is the carrier-envelope phase slip between consecutive laser pulses, which is straightforwardly measured in a self-referencing f-2f-setup and stabilized via a feedback loop [14, 15].

6.2.6 Spectral line-broadening mechanisms

In practice, the spectral line shapes of the transitions will often be affected by various broadening mechanisms due to, e.g., the Doppler effect or a finite upper-state lifetime of the excited transitions. In the case

of the latter, spontaneous emission causes the upper state population induced by the first pulse to decay over time so that the achievable Ramsey-fringe contrast after the second excitation will decrease accordingly. In the time domain, this effect is incorporated into the model via a multiplication of the Ramsey signals with an exponential decay function (τ is the lifetime of the upper state):

$$S_t \rightarrow S_t \cdot e^{-\frac{\Delta t}{2\tau}}. \quad (6.22)$$

In the single-transition case, the corresponding spectral shape is obtained via a convolution with a Lorentz-function with a linewidth of $1/(2\pi\tau)$:

$$|S_f^+|^2 \rightarrow |S_f|^2 \star \left[\frac{4\tau}{1 + (4\pi f\tau)^2} \right]. \quad (6.23)$$

As visualized in Fig. 6.4(c), this results in a broadening but not a shift of the spectral line positions. Similar to the inclusion of lifetime effects, other line-broadening mechanisms such as Doppler broadening or a finite laser linewidth can be incorporated via the appropriate multiplications and convolutions in the time and frequency domains.

However, for more than one simultaneously excited transition, the effect of the spectral-broadening mechanisms has to be incorporated into the complex spectral amplitudes described by Eq. (6.15). It will therefore also affect the spectral interference terms (see Eq. (6.18)) and thus cause slight systematic shifts of the spectral line positions. Hence in the multi-transition frequency-domain analysis of Ramsey-comb spectroscopy, all line-shaping effects have to be carefully taken into account for a correct interpretation of the spectral data.

6.3 Fitting of the Ramsey-comb signals

The main motivation for the development of the analytical Ramsey-comb model is to enable the fitting of the experimentally obtained signals so that the properties of the excited resonances can be extracted. In this section, we will first briefly discuss the more intuitive frequency-domain fitting approach. Afterward we will focus on an alternative fitting method used to analyze the experimental signals in [120], based purely in the time domain and found to be significantly more robust than the spectral fit approach.

6.3.1 Frequency-domain approach

For a single isolated transition, the spectral analysis is as straightforward as in traditional direct FC spectroscopy. However, for multiple transitions, the previously discussed interference terms (see Eq. (6.18)) complicate the spectral fitting procedure. In order to increase the robustness of the fitting algorithm, an iterative approach can be applied. For that we split up the absolute squared value of Eq. (6.15):

$$\mathcal{S}_f := \left| S_f^+ \right|^2 = \left| \sum_{k=1}^M s_k \right|^2, \quad (6.24)$$

with:

$$s_k := \left(\frac{A_k \delta t}{2} \right) \sin [(f - f_k) \delta t] \cdot \frac{\sin [N \pi T (f - f_k)]}{\sin [\pi T (f - f_k)]} \cdot \exp [-i(N + 1) \pi T (f - f_k)], \quad (6.25)$$

into a part without cross terms (note the different order of summing and taking the absolute value):

$$\mathcal{S}_f^0 := \sum_{k=1}^M |s_k|^2 \quad (6.26)$$

and the cross term (“interference term”) itself:

$$\mathcal{S}_f^{int} = \mathcal{S}_f - \mathcal{S}_f^0 = \sum_{k=1}^M \sum_{k'=1}^M (1 - \delta_{kk'}) s_k (s_{k'})_{c.c.}, \quad (6.27)$$

where *c.c.* denotes the complex conjugate and the Kronecker delta is defined as $\delta_{kk'} = 1$ for $k = k'$ and 0 otherwise. The iterative fitting procedure then consists of the following steps:

- (i) Fit \mathcal{S}_f^0 to the experimental spectrum, which is corrected for the interferences \mathcal{S}_f^{int} based on the initial parameter guesses.
- (ii) From the obtained fit results, (re)calculate \mathcal{S}_f^{int} .
- (iii) Again, fit the spectrum corrected for the most current \mathcal{S}_f^{int} and continue with the second step until the fit has converged.

An example of this fitting approach is depicted in Fig. 6.5 based on simulated data from two transitions 40 MHz apart with an amplitude ratio of $A_2/A_1 = 0.8$, $N = 25$ and $T = 8$ ns (see Eq. (6.15)). Given initial parameter guesses 500 kHz away from the modeled transition frequencies, the correct interference term \mathcal{S}_f^{int} is obtained within ~ 100 iterations; the final fit results match the modeled frequencies within 1 - 2 kHz. In general, however, experimental noise and the incorporation of line shapes as discussed in Sec. 6.2.6 severely affect the convergence of the spectral fit approach. Furthermore, it is in practice very challenging to fully include all line-shape mechanisms because apart from Doppler and lifetime broadening, there are various other physical and experimental effects that also contribute to the actual spectral line shape. The obtained fitting results are therefore prone to (small) systematic deviations. Because of these issues, we developed an alternative fitting approach,

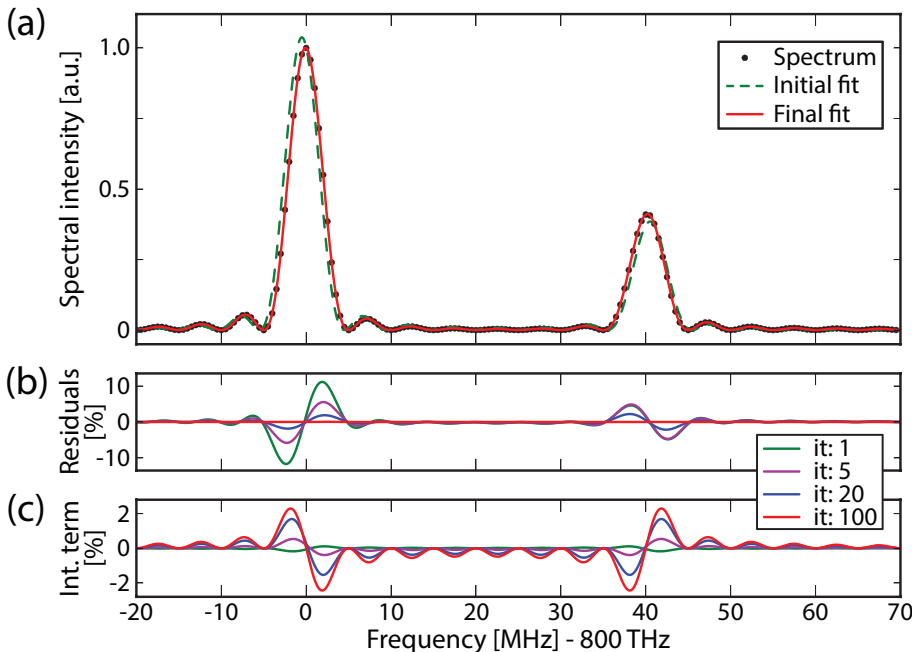


FIGURE 6.5: Example of the iterative spectral-domain fitting procedure for two unequal transitions 40 MHz apart; for more details see the text. (a) Simulated spectrum \mathcal{S}_f together with the initial and the final fit. (b) Fitting residuals for certain iterations steps (it). (c) Corresponding interference term \mathcal{S}_f^{int} of the most current fit result.

which is based purely in the time domain and is described in detail in the following section.

6.3.2 Time-domain approach

In the time domain, the signal from multiple resonances consists of a complex beating pattern with a time-dependent amplitude, carrier and phase. While it is possible to simultaneously fit all Ramsey scans on a global time axis using Eq. (6.10a), typically the fitting process is not very robust because of the periodicity of the fit function and the strong coupling between the different fit parameters. In addition, analogous to the frequency-domain approach described in the previous section, the inclusion of line-broadening effects further compromises the robustness of the fitting procedure. Therefore, we developed a fitting model based solely on the phases of the individual Ramsey fringes. This is possible because both the amplitudes and transition frequencies are fully encoded in the phase evolution of the complex beating pattern as visualized in Fig. 6.6; when multiple transitions are excited simultaneously, the phase of the Ramsey signals becomes a complex but characteristic function of the delay time. It is this phase trace that is sampled in Ramsey-comb spectroscopy and used for the frequency determination.

For analytical convenience, we introduce the complex quantity

$$\hat{S}_t := \sum_{k=1}^M A_k \exp[-i(2\pi f_k \Delta t + \phi_c)], \quad (6.28)$$

with the real part of \hat{S}_t corresponding to $S_{t,k}$ as defined in Eq. (6.19a). The argument (angle) of \hat{S}_t :

$$\begin{aligned} \arg(\hat{S}_t) &= : \Phi_{(A_1, \dots, A_M, f_1, \dots, f_M, \phi_c)}(\Delta t) \\ &= \Phi_{(A_1, \dots, A_M, f_1, \dots, f_M, \phi_c=0)}(\Delta t) - \phi_c \end{aligned} \quad (6.29)$$

describes the phase of the Ramsey signals and contains both transition amplitudes and frequencies as parameters as well as the common constant phase shift ϕ_c . While this phase shift no longer simply drops out as in the spectral-domain approach, it is still decoupled from the transition frequencies.

Figure 6.7 visualizes how Eq. (6.29) is used to perform the time-domain fitting. At first, the phase of the signal carrier at different macro

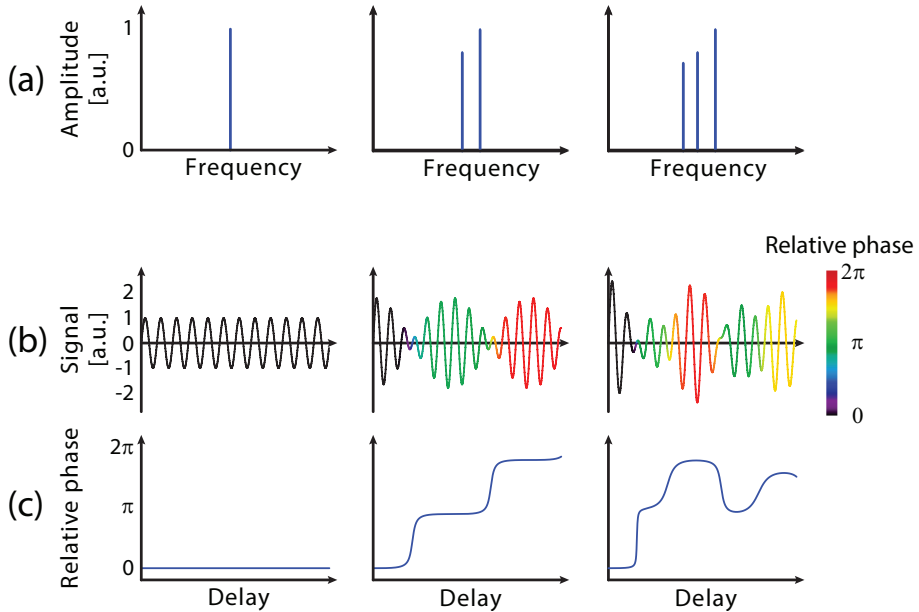


FIGURE 6.6: Schematic visualization of the phase evolution of Ramsey signals; each column describes a different set of transition frequencies. (a) Amplitudes of the resonant transitions. (b) Corresponding time-domain Ramsey signals with the instantaneous phase encoded in the color gradient (relative to the average carrier frequency). (c) Relative phase evolution as a function of delay.

delays is determined relative to a fixed reference frequency f_{ref} by fitting each individual Ramsey scan with

$$g(\Delta t, \Delta\phi, a) = a \cdot \cos(2\pi f_{ref} \Delta t + \Delta\phi). \quad (6.30)$$

While the exact value of f_{ref} is not important as it is only used for comparison, it is conveniently chosen close to the average signal carrier to facilitate straightforward fitting of the individual Ramsey signals. The obtained relative phases $\Delta\phi_n$ ($n = 1, 2, \dots, N$, where N is the number of measured Ramsey scans) can then be compared to

$$\Phi_{fit} := \Phi_{(A_1, \dots, A_M, f_1, \dots, f_M, \phi_c=0)}(\Delta t) - \phi_c - 2\pi f_{ref} \Delta t, \quad (6.31)$$

as visualized in Fig. 6.7(b). The minimization of $|\Phi_{fit}(\Delta t) - \Delta\phi_n|$ for $\Delta t = nT$ ($n = 1, \dots, N$) represents an N -dimensional χ^2 -problem. As long as the number of Ramsey scans is greater than or equal to the

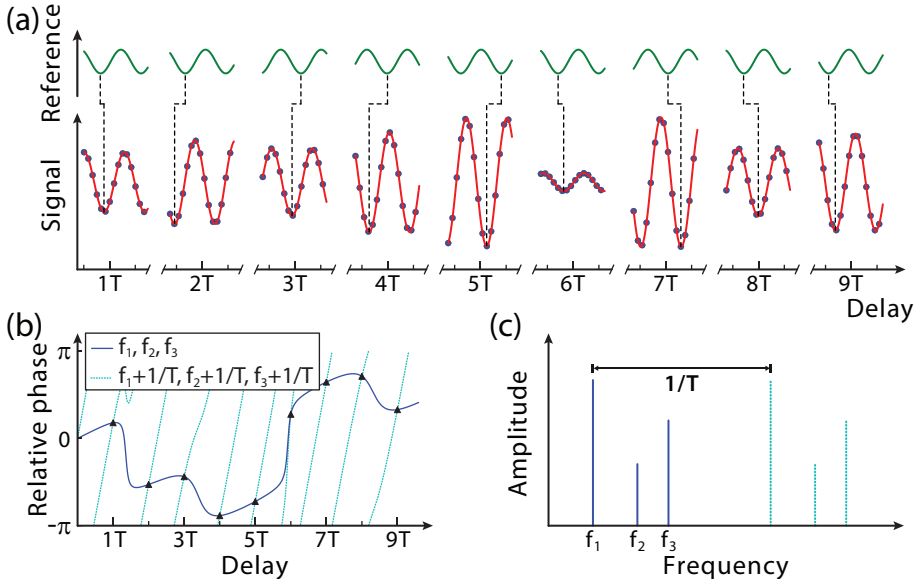


FIGURE 6.7: Schematic visualization of the time-domain fitting procedure. (a) Signal phases are determined relative to a fixed reference frequency. (b) Obtained relative phases as a function of delay (one value per individual Ramsey scan) are subsequently fitted with Φ_{fit} to obtain both the transition frequencies and amplitudes. The solid trace corresponds to the first (denoted by f_1, f_2, f_3) set of frequencies shown in part (c) and the dotted trace to the second set, $1/T$ off from the first one. (c) Due to the subsampling of the Ramsey signal in steps of T , the frequency can only be determined modulo $1/T$.

number of free parameters, numerical solutions can be obtained via a standard least-square fitting algorithm. Note that as in traditional direct FC spectroscopy, the frequencies can only be determined modulo $1/T = \langle f_{rep} \rangle$ (see Fig. 6.7(c)). This ambiguity, however, can be solved either by previous knowledge or by comparing measurements with slightly different repetition rates.

6.3.3 Numerical simulations of the time-domain fitting algorithm

In order to investigate the performance and precision of the developed fitting algorithm, the phase-fitting procedure was tested on a set of simulated Ramsey signals. The parameter space was kept comprehensible by limiting the simulations to two transitions ($M = 2$) with frequencies

of $f_1 = 800$ THz, $f_2 = f_1 + 40$ MHz and amplitudes $A_1 = 1$, $A_2 = 0.8$, unless stated otherwise. Figure 6.8 shows an example phase trace that is obtained from $N = 25$ simulated Ramsey scans. Gaussian noise with a standard deviation of 0.1 was added to model experimental noise, and a common upper-state lifetime of $\tau = 40$ ns was incorporated according to Eq. (6.22) as an example of a line-broadening mechanism.

As can be seen from Fig. 6.8, the reduction of signal amplitude due to the modeled lifetime leads to a less accurate determination of the Ramsey-signal phases for longer delay times. However, because the sensitivity of Φ_{fit} to changes in signal amplitude or frequency increases with delay time, the signal phases for longer delays also still have a comparable influence on the fitting result. In order to show this, Φ_{fit} was detuned from its best fit result by changing f_1 by 500 kHz (the dashed

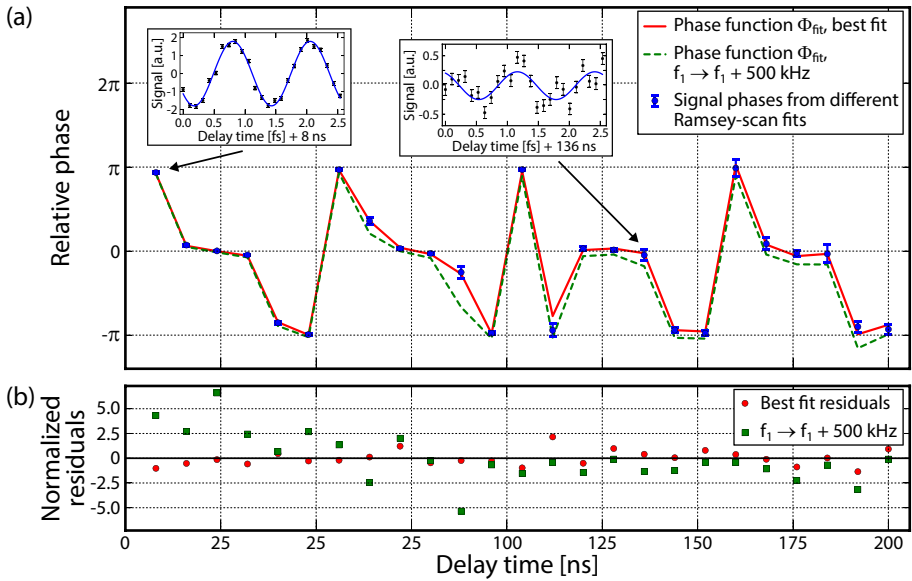


FIGURE 6.8: Example of a phase fit of simulated Ramsey signals. (a) Relative phase trace obtained from simulated Ramsey signals of two unequal transitions (for more details see the text). The insets show two of the Ramsey scans and the corresponding sinusoidal fits to determine the signal phase. The solid line visualizes the best fit result of the phase function Φ_{fit} , while the dashed line represents the same Φ_{fit} with the parameter for the first transition frequency changed by 500 kHz. (b) Residuals for both the best fit (dots) solution and the detuned Φ_{fit} (squares), both normalized to the uncertainties of the signal phase determination.

line in Fig. 6.8(a)). While for shorter delays the detuned phase function is still reasonably close to the obtained signal phases, it exhibits a more pronounced deviation for longer delay times.

Based on the parameter set shown in Fig. 6.8, a number of fits were performed for different sets of noise and randomly chosen initial fit parameters. The initial values for the frequencies and amplitudes were varied with standard deviations of 200 kHz and 10% of their absolute value, respectively. In Fig. 6.9, the results for 300 of such fits are shown. Note that during the fitting process, the amplitude of the first transition (A_1) was kept fixed since Φ_{fit} is only sensitive to the ratio of the amplitudes. Also, the common constant phase ϕ_c is not fitted, but in each fit iteration step the average offset between signal and fit phases is subtracted from the fit results. Figure 6.9 shows that not only the transition frequencies but also the amplitude ratio can be obtained very

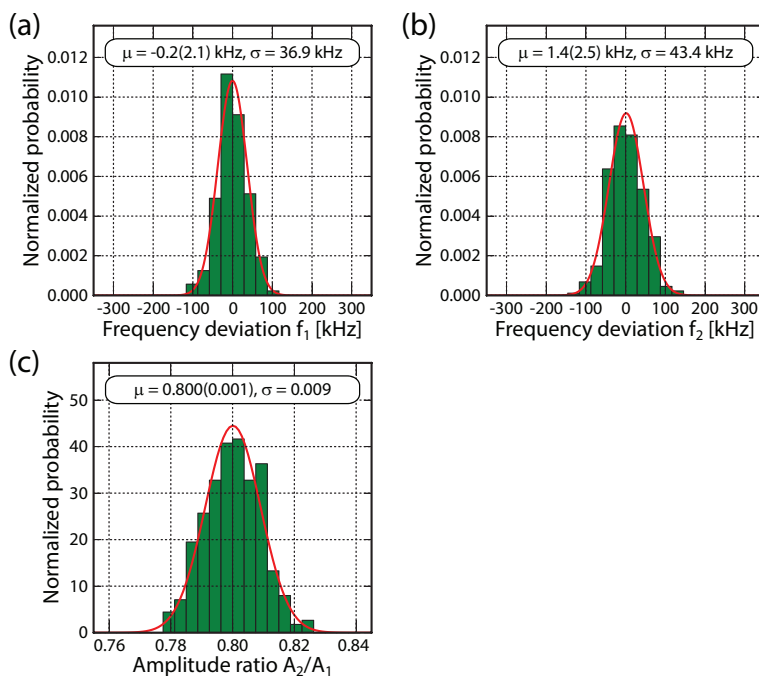


FIGURE 6.9: Phase-fit results for 300 simulated data sets for two transitions with an amplitude ratio $A_2/A_1 = 0.8$; see the text for more details. (a, b) Frequency results relative to the two input transition frequencies. (c) Obtained transition amplitude ratio. For each histogram, the standard deviation σ and the mean value μ with its statistical uncertainty are given.

accurately without any knowledge of the upper-state lifetime or a potential (transition-independent) constant phase shift. The achievable precision of the fitting (the standard deviation of the fit results based on 300 data sets with different noise and starting parameters) depends on the modeled signal-to-noise ratio of the Ramsey signals, and scales approximately linearly with the standard deviation of the applied Gaussian noise.

6.3.3.1 Influence from neighboring transitions

As the presented fitting algorithm acts purely in the time domain and is insensitive to common line shape mechanisms, it is interesting to investigate the resolution of this method, i.e., how the algorithm performs for two transitions close in frequency. In particular, for the case of two very unequal transitions one typically expects a strong effect for the weaker transition. We therefore simulated sets of 25 Ramsey signals as described previously but with a more unequal amplitude ratio of $A_2/A_1 = 0.4$ and various frequency spacings. As can be seen from Fig. 6.10, the fit precision gets worse when the two transitions are within about one linewidth (≈ 5 MHz) of the transitions. However, even when the two transitions are almost indistinguishable in the spectral domain, the transition frequency results can still be obtained without sizable systematic offsets.

6.3.3.2 Transition-dependent phase shifts and spectral line-broadening mechanisms

So far we have assumed that both line-broadening mechanisms and constant phase shifts affect all transitions exactly the same way. While this is a good approximation for many practical spectroscopic targets of Ramsey-comb spectroscopy, one can also extend the phase fit function Φ_{fit} to incorporate these transition-dependent effects according to

$$\Phi_{fit}^{ext} := \Phi_{(A_1(\Delta t), \dots, A_M(\Delta t), f_1, \dots, f_M, \phi_1, \dots, \phi_M, \phi_c=0)}^{ext}(\Delta t) - \phi_c - 2\pi f_{ref} \Delta t, \quad (6.32)$$

where Φ^{ext} now relates to an extended version of Eq. (6.28):

$$\hat{S}_t^{ext} = \sum_{k=1}^M A_k(\Delta t) \exp[-i(2\pi f_k \Delta t + \phi_k + \phi_c)]. \quad (6.33)$$

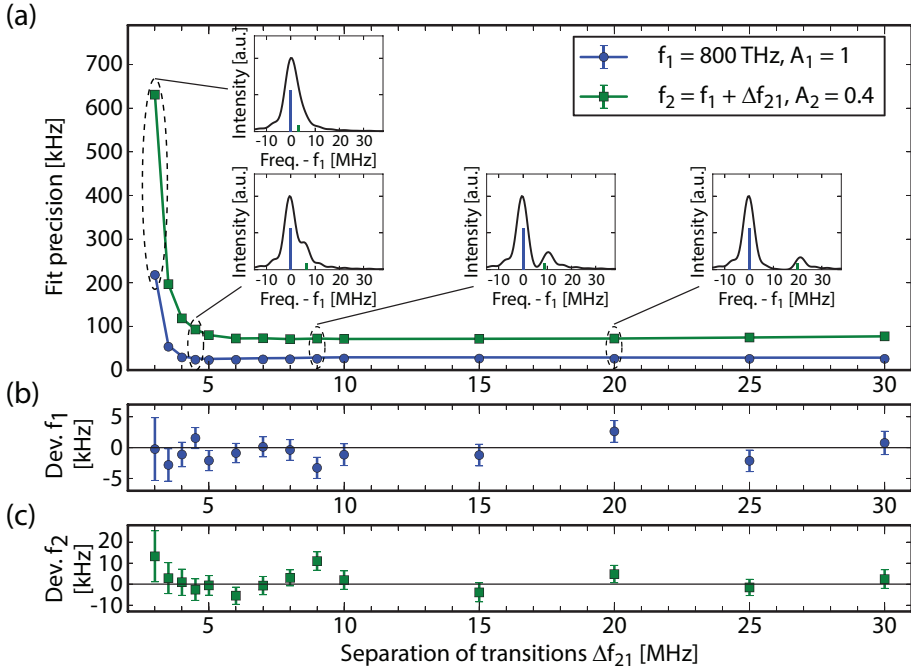


FIGURE 6.10: Fit results for two transitions with an amplitude ratio of $A_2/A_1 = 0.4$ and different frequency spacings $\Delta f_{21} = f_2 - f_1$. (a) Fit precision from 300 simulated Ramsey-signal sets. The insets show the frequency-domain representation of four spectra according to certain frequency spacings. (b, c) Deviations of the mean fit values relative to the modeled transition frequencies of the first and second transitions.

The ϕ_k -terms allow for additional transition-dependent phase shifts, whereas ϕ_c still represents a transition-independent constant phase shift and is treated as before. Furthermore, the previously constant amplitudes A_k can now also have a dependence on the delay time Δt , which allows us to incorporate individual spectral line-broadening mechanisms.

To investigate individual phase shifts, again 300 datasets are produced analogously to the simulations that led to the results shown in Fig. 6.9 but this time incorporating a constant phase shift of 0.4 rad for the first transition and 0.7 rad for the second; the initial starting parameters for the individual phase shifts were varied with a standard deviation of 10% of their absolute value. The results of the fitting series are shown in Fig. 6.11.

As compared to the results without a differential phase shift (see

Fig. 6.9), the uncertainties of the transition frequencies have increased by about a factor of two, but still no systematic deviations are introduced. In addition, the value of the differential phase shift $\Delta\phi_{21} = \phi_2 - \phi_1$ is also obtained from the analysis (the common phase shift of 0.4 rad is incorporated in ϕ_c). Note that apart from A_1 , ϕ_1 was also fixed during the fitting since for both parameters only the differential values are of significance.

Returning to common constant phase shifts ($\phi_k = 0$), we now investigate the influence of delay-time-dependent amplitudes $A_k(\Delta t)$. For the case that all transitions are affected the same way, we already discussed in Sec. 6.2.6 the reduction of signal strength due to, e.g., natural decay of the upper state or the Doppler effect. Analogous to Eq. (6.22), we

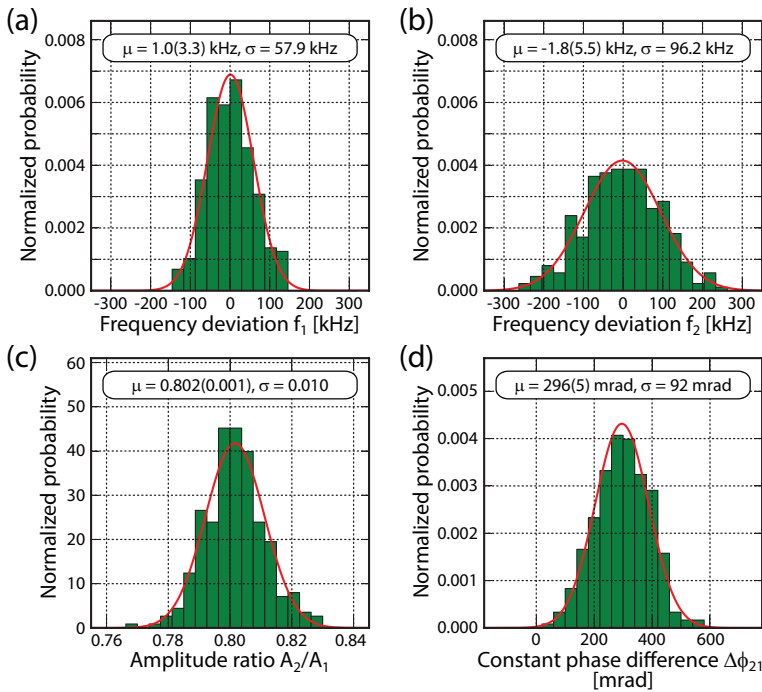


FIGURE 6.11: Phase-fit results for 300 simulated data sets for two transitions with an amplitude ratio $A_2/A_1 = 0.8$ and a differential constant phase shift of $\Delta\phi_{21} = 300$ mrad; see the text for more details. (a, b) Frequency results relative to the two input transition frequencies. (c) Obtained transition amplitude ratio. (d) Obtained differential phase shift. For each histogram, the standard deviation σ and the mean value μ with its statistical uncertainty are given.

now incorporate individual lifetimes τ_k in the form of delay-dependent amplitudes according to:

$$A_k(\Delta t) = A_k(0) \cdot e^{-\frac{\Delta t}{2\tau_k}}. \quad (6.34)$$

Again, the performance of Φ_{fit}^{ext} is investigated by simulating 300 signal sets as before but with a 10% increased lifetime for the second transition of $\tau_2 = 44$ ns; the initial starting parameters for the lifetimes τ_k were varied with a standard deviation of 10%. From the results in Fig. 6.12, we see again that the uncertainties increased in contrast to the results shown in Fig. 6.9. Nevertheless, the inclusion of the lifetime does not induce sizable systematic shifts on the determination of the frequencies or the amplitude ratio.

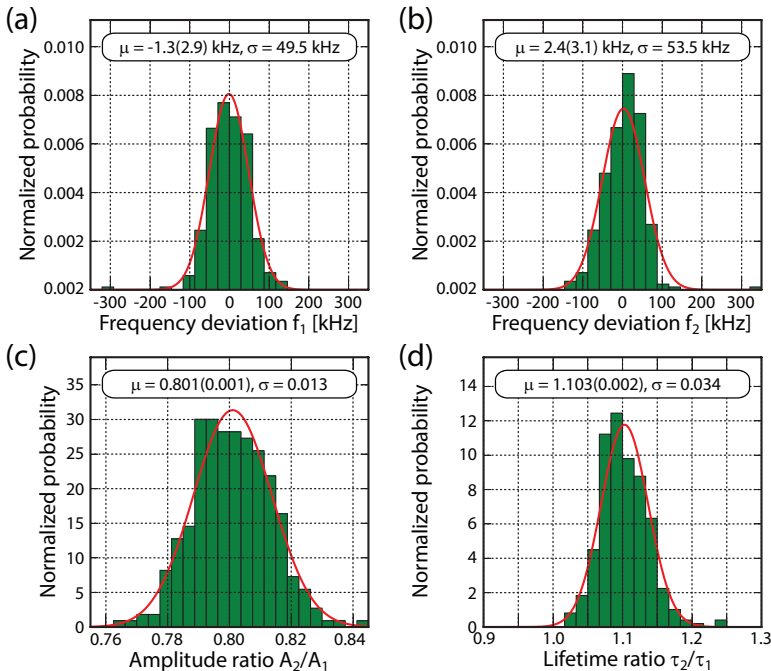


FIGURE 6.12: Phase-fit results for 300 simulated data sets for two transitions with an amplitude ratio $A_2/A_1 = 0.8$ and an upper-state lifetime ratio of $\tau_2/\tau_1 = 1.1$; see the text for more details. (a, b) Frequency results relative to the two input transition frequencies. (c) Obtained transition amplitude ratio. (d) Obtained transition lifetime ratio. For each histogram, the standard deviation σ and the mean value μ with its statistical uncertainty are given.

6.4 Conclusion

In this chapter we presented a comprehensive framework describing the temporal and spectral representations of spectroscopic signals obtained by the Ramsey-comb method [120], which relies on the combination of optical Ramsey signals at variable macro delays. Based on this framework, fitting algorithms in both the time and frequency domains were developed. The spectral-domain approach was found to be severely compromised because of additional interference terms that are not present in traditional comb spectroscopy. In the time domain, however, it was shown that the spectroscopic analysis can be performed solely based on the Ramsey-signal phases from different macro delays. The performance of the fitting algorithm was investigated via numerical simulations, verifying that common line-broadening mechanisms and constant phase shifts, e.g., due to the AC-stark effect do not affect the fitting outcome. Furthermore, the inclusion of also transition-dependent line-broadening mechanisms and constant phase shifts only affects the uncertainty of the fit results but does not introduce sizable additional shifts.

CHAPTER 7

OUTLOOK

In the first part of this outlook chapter, upgrades of the experimental system are suggested to further enhance its performance. The second part discusses potential future spectroscopy targets for the Ramsey-comb spectroscopy method.

7.1 Upgrades of the current system

For the experiments carried out in the course of this thesis, the output of the employed laser system was fully sufficient. However, the approach of selective frequency comb (FC) pulse amplification allows for straightforward further scaling in both peak and average energy, which would be beneficial for future experiments requiring higher energies.

In terms of peak energy, the limiting factor is the damage threshold of the amplifier crystals for the high-energy pump pulses in the post-amplifier. For lowering the peak intensity by increasing the maximum useable beam diameter, a second diode-pumped post-amplifier module with an almost two times larger crystal rod diameter of 10 mm (REA10008-3P200H, Cutting Edge Optronics) is ready to be implemented. In the meantime, such an amplifier module has been incorporated and tested in a similar amplifier configuration producing 1064 nm pulses with up to 130 mJ of pulse energy [86] (the maximum pump pulse energy in the rubidium/cesium experiment was 40 mJ). The same company now also offers laser rod diameters of up to 15 mm diameter with prospects for even larger-diameter rods in the near future. Therefore, by implementing such an additional post-amplifier stage, amplified FC pulse energies of tens of millijoules can straightforwardly be achieved.

In order to speed up the acquisition rate and gather more statistics, the repetition rate of the system (currently working at 28 Hz) can be

increased. In fact, a potential increase in repetition rate was one of the main motivations for changing the pump amplifier to a completely diode-pumped system. The pre-amplifier readily supports operation at 300 Hz without any physical adjustment [91], and also the post-amplifier can be operated at the same rate (see [86]), thus enabling an about ten times higher acquisition rate than what has been used during the spectroscopy experiments in this thesis. In order to change the repetition rate of the post-amplifier, only the imaging within and directly after the post-amplifier has to be changed to incorporate the increased thermal lensing.

7.2 Future spectroscopy targets

We have demonstrated that in terms of statistics and systematics, the achievable accuracy of Ramsey-comb spectroscopy is on the same level as the most precise traditional (i.e., FC) spectroscopy methods. However, the available high pulse energies makes it particularly interesting to investigate transitions that are very weak and/or require nonlinear wavelength conversion.

7.2.1 Molecular hydrogen

The two-photon X-EF transitions in molecular hydrogen and hydrogen like systems are particularly interesting targets for Ramsey-comb spectroscopy. These transitions have recently been measured by our group [30] with an accuracy of a few MHz using a narrowband, nanosecond pulsed amplified dye laser and nonlinear crystals to produce the required ultraviolet radiation around 200 nm. By using the method of Ramsey-comb spectroscopy and the experimental system described in this thesis, two of the main contributions to the error budget, the uncertainty of the AC-Stark shift determination and frequency shifts due to the chirp of the excitation pulses, would not be of concern anymore. The biggest systematic uncertainty would likely be the residual Doppler shift, which in [30] led to a systematic uncertainty of 1.1 MHz. However, this shift can be calibrated considerably more accurately by changing the velocity of the hydrogen molecules via seeding the hydrogen gas with heavier atoms and extrapolating to zero velocity (in [30] this was not performed because the uncertainties from other systematic effects dominated the systematic error budget). Therefore, an accuracy of tens of kHz on these transitions seems feasible, a result, which apart from stringently testing the theory of quantum electrodynamics (QED)

in molecules would also put tighter constraints on speculative 5th forces outside the standard model [122].

7.2.2 The helium ion

While precision spectroscopy on hydrogen currently makes QED the most accurately tested theory in physics [123], helium exhibits a higher nuclear charge, which results in an increased sensitivity to high-order QED corrections [32]. A particular interesting transition would be the two-photon 1S-2S transition in He^+ , which so far has not been measured at all. Similar to hydrogen, the simple, mono-electronic structure of He^+ allows for a very accurate calculation of its energy levels and thus facilitates very stringent tests of QED by comparing theory and experiments. It could also provide new insights into the highly-debated proton-size puzzle [88, 110]. An additional advantage is that because of its electrical charge, the helium ion can be trapped and (sympathetically) cooled [124]. Hence, it allows for long interaction times and low systematic uncertainties from second-order Doppler shifts. Direct excitation of the 1S-2S transition requires two photons at 61 nm. While the wavelength as such can be reached straightforwardly via high-harmonic generation in a gas jet as employed in [92], producing sufficient power to drive the weak non-resonant two-photon transition is still a challenge.

APPENDIX A

FOURIER TRANSFORMS

For the convenience of the reader, this chapter contains a range of Fourier transforms and functional relationships that were used in the course of this thesis

A.1 Definition of the Fourier transform

The Fourier transform connecting the time- and frequency-domain representations of reasonably well-behaved functions* is by convention defined as [125]:

$$h_f = \mathcal{FT}\{h_t\}(f) = \int_{-\infty}^{+\infty} h_t(t) e^{-i2\pi ft} dt, \quad (\text{A.1a})$$

$$h_t = \mathcal{FT}^{-1}\{h_f\}(t) = \int_{-\infty}^{+\infty} h_f(f) e^{i2\pi ft} df. \quad (\text{A.1b})$$

If we use angular instead of regular frequencies ($\omega = 2\pi f$), the convention changes accordingly to:

$$h_\omega = \mathcal{FT}\{h_t\}(\omega) = \int_{-\infty}^{+\infty} h_t(t) e^{-i\omega t} dt, \quad (\text{A.2a})$$

$$h_t = \mathcal{FT}^{-1}\{h_\omega\}(t) = \frac{1}{2\pi} \int_{-\infty}^{+\infty} h_\omega(\omega) e^{i\omega t} d\omega. \quad (\text{A.2b})$$

*An all-encompassing condition for the existence of the Fourier transform of a function $h(x)$ is $\int_{-\infty}^{\infty} |h(x)|^2 dx < \infty$.

A.2 Lists of common Fourier transforms and relationships

Most of the applied Fourier transforms throughout the thesis can be deduced from the following set of standard transforms (Tab. A.1) and relations (Tab. A.2), which can be found, e.g., in [125]; $\text{sinc}(x) = \sin(\pi x)/(\pi x)$ and $\text{rect}(t)$ is 1 for $|t| < 1/2$ and 0 otherwise.

$h_t(t)$	$h_f(f)$	$h_\omega(\omega)$
$e^{-\alpha t^2}$	$\sqrt{\frac{\pi}{\alpha}} e^{-\frac{\pi^2 f^2}{\alpha}}$	$\sqrt{\frac{\pi}{\alpha}} e^{-\frac{\omega^2}{4\alpha}}$
$e^{-\alpha t }$	$\frac{2\alpha}{\alpha^2 + 4\pi^2 f^2}$	$\frac{2\alpha}{\alpha^2 + \omega^2}$
$\text{rect}(\alpha t)$	$\frac{1}{\alpha} \text{sinc}\left(\frac{f}{\alpha}\right)$	$\frac{1}{\alpha} \text{sinc}\left(\frac{\omega}{2\pi\alpha}\right)$
$\text{sinc}(\alpha t)$	$\frac{1}{\alpha} \text{rect}\left(\frac{f}{\alpha}\right)$	$\frac{1}{\alpha} \text{rect}\left(\frac{\omega}{2\pi\alpha}\right)$
$\delta(t - \alpha)$	$e^{-i\alpha 2\pi f}$	$e^{-i\alpha\omega}$
$\cos(\alpha t)$	$\frac{1}{2} \left[\delta\left(f - \frac{\alpha}{2\pi}\right) + \delta\left(f + \frac{\alpha}{2\pi}\right) \right]$	$\pi \left[\delta(\omega - \alpha) + \delta(\omega + \alpha) \right]$
$\sin(\alpha t)$	$\frac{1}{2i} \left[\delta\left(f - \frac{\alpha}{2\pi}\right) - \delta\left(f + \frac{\alpha}{2\pi}\right) \right]$	$\frac{\pi}{i} \left[\delta(\omega + \alpha) + \delta(\omega - \alpha) \right]$
$\sum_{n=-\infty}^{\infty} \delta(t - nT)$	$\frac{1}{T} \sum_{n=-\infty}^{\infty} \delta\left(f - \frac{n}{T}\right)$	$\frac{2\pi}{T} \sum_{n=-\infty}^{\infty} \delta\left(\omega - \frac{2\pi n}{T}\right)$
$\left \sum_{n=0}^{\infty} \delta(t - nT) \right $	$\left \frac{1}{T} \sum_{n=0}^{\infty} \delta\left(f - \frac{n}{T}\right) \right $	$\left \frac{2\pi}{T} \sum_{n=0}^{\infty} \delta\left(\omega - \frac{2\pi n}{T}\right) \right $

TABLE A.1: Set of Fourier-transform pairs that were commonly used in the course of this thesis. The Fourier transforms of the time-domain function $h_t(t)$ were converted to the frequency-domain representations $h_f(f)$ and $h_\omega(\omega)$ via Eqs. (A.1b) and (A.2b), respectively; α and T are positive real numbers.

Time domain	Frequency domain	
$h_t(t) \cdot \tilde{h}_t(t)$	$h_f(f) \star \tilde{h}_f(f)$	$\frac{1}{2\pi} h_\omega(\omega) \star \tilde{h}_\omega(\omega)$
$h_t(t) \star \tilde{h}_t(t)$	$h_f(f) \cdot \tilde{h}_f(f)$	$h_\omega(\omega) \cdot \tilde{h}_\omega(\omega)$
$h_t(t - \alpha)$	$e^{-i\alpha 2\pi f} \cdot h_f(f)$	$e^{-i\alpha \omega} \cdot h_\omega(\omega)$
$e^{i2\alpha\pi t} \cdot h_t(t)$	$h_f(f - \alpha)$	$h_\omega(\omega - 2\pi\alpha)$

TABLE A.2: Set of functional Fourier transform relationships between the time and frequency domains (for both regular and angular frequencies), based on the definitions in Eqs. (A.1) and (A.2); α is a positive real number.

APPENDIX B

QUANTUM INTERFERENCE EXCITATION WITH LASER PULSES

In this chapter, we present the quantum-mechanical derivation leading to the basic Ramsey-fringe expression Eq. (6.1), which was used as the starting point for the Ramsey-comb framework as described in Ch. 6.

B.1 Single-pulse excitation

The state vector of an isolated two-level atomic system can be written as:

$$|\Psi\rangle = \begin{pmatrix} c_e(t) \\ c_g(t) \end{pmatrix}, \quad (\text{B.1})$$

where $c_g(t)$ and $c_e(t)$ denote the quantum-mechanical probability amplitudes of finding the atom in the ground and excited states, respectively. The energy of the system is determined by the Hamilton operator, which in the case of an unperturbed two-level system is:

$$\mathcal{H}_0 = \hbar \begin{pmatrix} -\omega_k/2 & 0 \\ 0 & \omega_k/2 \end{pmatrix}, \quad (\text{B.2})$$

with the transition frequency determined by the energy difference of the two states, $\omega_k = (E_e - E_g)/\hbar$ (see Fig. B.1); \hbar is the reduced Planck constant. The zero off-diagonal elements of \mathcal{H}_0 imply that there is no interaction allowed between the two energy states. However, an external electric field $\mathbf{E}(t) = \mathbf{E}_0 e^{-i\omega_L t} + \mathbf{E}_0^* e^{i\omega_L t}$, approximately resonant with the atomic transition ($\omega_L \approx \omega_k$), lifts this limitation by inducing a

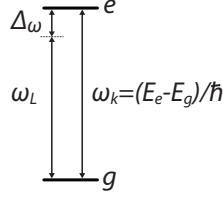


FIGURE B.1: Schematic of the abstract two-level atomic system used in the derivation. Indicated are the external laser frequency ω_L and its detuning $\Delta\omega$ from the transition frequency ω_k , which is related to the energy difference between the excited (e) and ground (g) state; \hbar is the reduced Planck constant.

coupling between the states. Since in many cases the size of the atom is much smaller than the wavelength of the electromagnetic radiation, we assume a pure dipole interaction that is described by the dipole operator \mathbf{d}_{21} connecting the lower and upper energy states [126]:

$$\begin{aligned}\mathcal{H}_{int}(t) &= -\mathbf{d}_{21} \cdot \mathbf{E}(t) \\ &= -\begin{pmatrix} 0 & \mathbf{d}_{21}^* \\ \mathbf{d}_{21} & 0 \end{pmatrix} \cdot (\mathbf{E}_0 e^{-i\omega_L t} + \mathbf{E}_0^* e^{i\omega_L t}) \\ &= -\hbar \begin{pmatrix} 0 & \Omega_R e^{-i\omega_L t} + \tilde{\Omega}_R e^{i\omega_L t} \\ \tilde{\Omega}_R^* e^{-i\omega_L t} + \Omega_R^* e^{i\omega_L t} & 0 \end{pmatrix}, \quad (\text{B.3})\end{aligned}$$

where the Rabi frequency ($\Omega_R = \mathbf{d}_{21} \cdot \mathbf{E}_0/\hbar$) and the counter-rotating frequency ($\tilde{\Omega}_R = \mathbf{d}_{21} \cdot \mathbf{E}_0^*/\hbar$) were introduced in the last step. Consequently, the complete Hamiltonian of the perturbed two-level system is:

$$\begin{aligned}\mathcal{H}_{tot}(t) &= \mathcal{H}_0(t) + \mathcal{H}_{int}(t) \\ &= -\hbar \begin{pmatrix} -\omega_k/2 & \Omega_R e^{-i\omega_L t} + \tilde{\Omega}_R e^{i\omega_L t} \\ \tilde{\Omega}_R^* e^{-i\omega_L t} + \Omega_R^* e^{i\omega_L t} & \omega_k/2 \end{pmatrix}. \quad (\text{B.4})\end{aligned}$$

As a first step to deal with the complex time dependence of \mathcal{H}_{tot} , we transform to another, time-dependent frame of reference (“Schrödinger picture”) via the unitary transformation described by:

$$\mathcal{U}(t) = \begin{pmatrix} e^{-i\omega_L t/2} & 0 \\ 0 & e^{i\omega_L t/2} \end{pmatrix}, \quad (\text{B.5})$$

which relates the initial state $|\Psi\rangle$ with the transformed state $|\bar{\Psi}\rangle$ via the matrix multiplication:

$$|\Psi\rangle(t) = \mathcal{U}(t) |\bar{\Psi}(t)\rangle. \quad (\text{B.6})$$

In order to transform the Hamiltonian, we insert Eq. (B.6) into the Schrödinger equation:

$$i\hbar \frac{\partial |\Psi(t)\rangle}{\partial t} = \mathcal{H}_{tot}(t) |\Psi(t)\rangle \quad (\text{B.7})$$

and multiply the resulting expression by the Hermitian conjugate of the transformation matrix, $\mathcal{U}^\dagger(t)$. The result is the transformed Hamiltonian:

$$\begin{aligned} \bar{\mathcal{H}}_{tot}(t) &= -i\hbar \mathcal{U}(t)^\dagger \dot{\mathcal{U}}(t) + \mathcal{U}(t)^\dagger \mathcal{H}_{tot}(t) \mathcal{U}(t) \\ &= -\hbar \begin{pmatrix} (\omega_L - \omega_k)/2 & \Omega_R + \tilde{\Omega}_R e^{i2\omega_L t} \\ \tilde{\Omega}_R^* e^{-2i\omega_L t} + \Omega_R^* & -(\omega_L - \omega_k)/2 \end{pmatrix}. \end{aligned} \quad (\text{B.8})$$

The remaining time-dependent terms that oscillate at $2\omega_L$ are commonly neglected since under the assumption $\omega_L \approx \omega_k$ they are assumed to average out quickly [127]. By applying this so-called “rotating-wave approximation” (we implicitly neglect the previously defined counter-rotating frequency $\tilde{\Omega}_R = \mathbf{d}_{21} \cdot \mathbf{E}_0^*/\hbar$), the Hamiltonian is now completely time-independent. Writing the difference between the transition and external field frequencies as $\Delta_\omega = \omega_k - \omega_L$ (see Fig. B.1), we can express the Hamiltonian in the compact form of:

$$\bar{\mathcal{H}}_{tot} = -\hbar \begin{pmatrix} -\Delta_\omega/2 & \Omega_R \\ \Omega_R^* & \Delta_\omega/2 \end{pmatrix}. \quad (\text{B.9})$$

The approximated, time-independent Hamiltonian allows a straightforward integration of the Schrödinger equation. For a square pulse of length τ_p , we obtain the evolved state vector as a function of the initial state as:

$$|\bar{\Psi}(\tau_p)\rangle = e^{-i\bar{\mathcal{H}}_{tot}\tau_p/\hbar} |\bar{\Psi}(0)\rangle. \quad (\text{B.10})$$

In order to arrive at a more insightful representation of Eq. (B.10), we rewrite the Hamiltonian as $\bar{\mathcal{H}}_{tot} = -\hbar \mathbf{b} \cdot \boldsymbol{\sigma}$, with:

$$\mathbf{b} = \begin{pmatrix} \text{Re}\{\Omega_R\} \\ \text{Im}\{\Omega_R\} \\ -\Delta_\omega/2 \end{pmatrix} \text{ and } \boldsymbol{\sigma} = \begin{pmatrix} \sigma_x \\ \sigma_y \\ \sigma_z \end{pmatrix}, \quad (\text{B.11})$$

in which $\boldsymbol{\sigma}$ is a vector holding the Pauli matrices:

$$\sigma_x = \begin{pmatrix} 0 & 1 \\ 1 & 0 \end{pmatrix}, \sigma_y = \begin{pmatrix} 0 & -i \\ i & 0 \end{pmatrix}, \sigma_z = \begin{pmatrix} 1 & 0 \\ 0 & -1 \end{pmatrix}. \quad (\text{B.12})$$

We can then expand the exponential operator according to [128]:

$$\begin{aligned} e^{-i\bar{\mathcal{H}}_{tot}\tau_p/\hbar} &= e^{i\mathbf{b}\cdot\boldsymbol{\sigma}\tau_p} \\ &= \sum_{n=0}^{\infty} \frac{1}{n!} (i\mathbf{b}\cdot\boldsymbol{\sigma})^n \\ &= \cos(b\tau_p) \mathbf{1} + i(\mathbf{b}/b)\cdot\boldsymbol{\sigma}\sin(b\tau_p), \end{aligned} \quad (\text{B.13})$$

where $\mathbf{1}$ denotes the identity matrix and the generalized Rabi frequency is defined as:

$$b = |\mathbf{b}| = \sqrt{|\Omega_R|^2 + (\Delta_\omega/2)^2}. \quad (\text{B.14})$$

We can now write the matrix describing the state evolution due to the interaction with the light pulse as a function of the pulse duration τ_p in the convenient form of:

$$\begin{aligned} \mathcal{M}_{pulse} &= e^{i\mathbf{a}\cdot\boldsymbol{\sigma}\tau_p} \\ &= \begin{pmatrix} \cos(a\tau_p) - i\frac{\Delta_\omega}{2a}\sin(a\tau_p) & i\frac{\Omega_R}{a}\sin(a\tau_p) \\ i\frac{\Omega_R^*}{a}\sin(a\tau_p) & \cos(a\tau_p) + i\frac{\Delta_\omega}{2a}\sin(a\tau_p) \end{pmatrix}. \end{aligned} \quad (\text{B.15})$$

Within the underlying approximations (dipole interaction, rotating-wave approximation and square, monochromatic excitation pulses), \mathcal{M}_{pulse} enables us to calculate the state vector of an atomic system after excitation with the first laser pulse:

$$|\bar{\Psi}(\tau_p)\rangle = \mathcal{M}_{pulse} |\bar{\Psi}(0)\rangle. \quad (\text{B.16})$$

B.2 Ramsey fringes from a coherent double-pulse sequence

In order to incorporate a second interaction with a delayed excitation pulse, we need to account for the free evolution $T - \tau_p$ of the atomic state in between the pulses (see Fig. B.2). Neglecting spontaneous decay and other external influences such as dephasing due to the movement of the atoms (Doppler broadening), the free evolution matrix \mathcal{M}_{free} can be derived from \mathcal{M}_{pulse} for $\Omega_R = 0$, i.e., in the absence of an external electric field:

$$\mathcal{M}_{free} = \begin{pmatrix} e^{-i(\Delta t - \tau_p)\Delta_\omega/2} & 0 \\ 0 & e^{i(\Delta t - \tau_p)\Delta_\omega/2} \end{pmatrix}. \quad (\text{B.17})$$

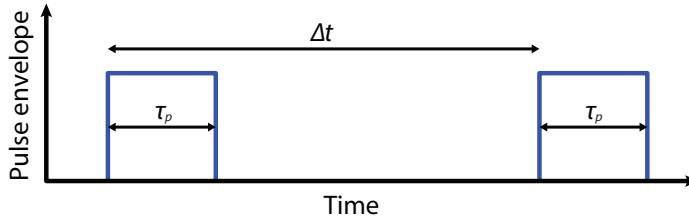


FIGURE B.2: Schematic of the two square pulses (each of length τ_p and delayed by Δt) as assumed in the derivation.

Now we can derive the atomic state vector directly after the second excitation pulse from a series of matrix multiplications:

$$|\bar{\Psi}(\Delta t + \tau_p)\rangle = \mathcal{M}_{pulse}\mathcal{M}_{free}\mathcal{M}_{pulse}|\bar{\Psi}(0)\rangle. \quad (\text{B.18})$$

If we assume the atom to be initially in the ground state ($c_g(0) = 1$, $c_e(0) = 0$, see Eq. (B.1)), the excited-state amplitude will be:

$$c_e(\Delta t + \tau_p) = i\frac{2\Omega_R}{b}\sin(b\tau_p)\left[\cos(b\tau_p)\cos\left(\frac{\omega_k\Delta t - \tau_p\Delta\omega}{2}\right) - \frac{\Delta\omega}{2b}\sin(b\tau_p)\sin\left(\frac{\omega_k\Delta t - \tau_p\Delta\omega}{2}\right)\right]. \quad (\text{B.19})$$

The absolute value squared of Eq. (B.19) is (with $\delta_{ex} = \omega_L\Delta t$) equivalent to Eq. (6.1), which in Ch. 6 was used as the starting point for the derivation of the Ramsey-comb framework.

When the external laser field is exactly resonant ($\Delta\omega = 0$ and hence $b = \Omega_R$), Eq. (B.19) collapses to:

$$c_e(\Delta t + \tau_p) = i2\sin(\Omega_R\tau_p)\cos(\Omega_R\tau_p)\cos(\omega_k\Delta t/2). \quad (\text{B.20})$$

The experimentally measurable quantity, however, is not c_e but the upper-state population $\mathcal{P} \propto |c_e|^2$, hence for the dependence on the inter-pulse delay Δt we find:

$$\boxed{\mathcal{P}(\Delta t) \propto 1 + \cos(\omega_k\Delta t)}. \quad (\text{B.21})$$

The characteristic periodic pattern of \mathcal{P} is usually referred to as Ramsey fringes [2].

Finally, it should be noted that the derivations in this chapter are based on the somewhat unphysical assumption of square excitation-pulse

envelopes. In order to study the influence of more realistic pulse shapes one can numerically integrate a set of Bloch equations for the density matrix of the system [129–131]. It can be shown that while the temporal pulse envelope \mathbf{E}_0 has an influence on the signal amplitude, it does not introduce further phase shifts of the Ramsey fringes. Even a temporal chirp, i.e., a time-dependent instantaneous frequency, does not affect the phase as long as both excitation pulses are equally chirped [132].

BIBLIOGRAPHY

- [1] N. F. Ramsey, *A New Molecular Beam Resonance Method*, Physical Review **76**, 996 (1949).
- [2] N. F. Ramsey, *A Molecular Beam Resonance Method with Separated Oscillating Fields*, Physical Review **78**, 695 (1950).
- [3] N. F. Ramsey, *Experiments with separated oscillatory fields and hydrogen masers*, Review of Modern Physics **62**, 541 (1990).
- [4] S. A. Diddams, J. C. Bergquist, S. R. Jefferts, and C. W. Oates, *Standards of Time and Frequency at the Outset of the 21st Century*, Science **306**, 1318 (2004).
- [5] N. F. Ramsey, *Resonance Experiments in Successive Oscillatory Fields*, Review of Scientific Instruments **28**, 57 (1957).
- [6] Y. V. Baklanov, B. Y. Dubetsky, and V. P. Chebotayev, *Non-linear ramsey resonance in the optical region*, Applied Physics **9**, 171 (1976).
- [7] J. C. Bergquist, S. A. Lee, and J. L. Hall, *Saturated Absorption with Spatially Separated Laser Fields: Observation of Optical “Ramsey” Fringes*, Physical Review Letters **38**, 159 (1977).
- [8] M. M. Salour and C. Cohen-Tannoudji, *Observation of Ramsey’s Interference Fringes in the Profile of Doppler-Free Two-Photon Resonances*, Physical Review Letters **38**, 757 (1977).
- [9] J. C. Bordé, *Sur les franges de Ramsey en spectroscopie sans élargissement Doppler*, Comptes Rendus de l’Académie des Sciences Paris **248B**, 101 (1977).
- [10] R. Teets, J. Eckstein, and T. W. Hänsch, *Coherent Two-Photon Excitation by Multiple Light Pulses*, Physical Review Letters **38**, 760 (1977).
- [11] J. N. Eckstein, A. I. Ferguson, and T. W. Hänsch, *High-Resolution Two-Photon Spectroscopy with Picosecond Light Pulses*, Physical Review Letters **40**, 847 (1978).

- [12] T. W. Hänsch, *Laser Spectroscopy III* (Springer-Verlag, 1978).
- [13] D. J. Jones, S. A. Diddams, J. K. Ranka, A. Stentz, R. S. Windeler, J. L. Hall, and S. T. Cundiff, *Carrier-Envelope Phase Control of Femtosecond Mode-Locked Lasers and Direct Optical Frequency Synthesis*, *Science* **288**, 635 (2000).
- [14] S. A. Diddams et al., *Direct Link between Microwave and Optical Frequencies with a 300 THz Femtosecond Laser Comb*, *Physical Review Letters* **84**, 5102 (2000).
- [15] R. Holzwarth, T. Udem, T. W. Hänsch, J. C. Knight, W. J. Wadsworth, and P. S. J. Russell, *Optical Frequency Synthesizer for Precision Spectroscopy*, *Physical Review Letters* **85**, 2264 (2000).
- [16] T. Udem, J. Reichert, R. Holzwarth, and T. W. Hänsch, *Accurate measurement of large optical frequency differences with a mode-locked laser*, *Optics Letters* **24**, 881 (1999).
- [17] T. Udem, J. Reichert, R. Holzwarth, and T. W. Hänsch, *Absolute Optical Frequency Measurement of the Cesium D_1 Line with a Mode-Locked Laser*, *Physical Review Letters* **82**, 3568 (1999).
- [18] H. Schnatz, B. Lipphardt, J. Helmcke, F. Riehle, and G. Zinner, *First Phase-Coherent Frequency Measurement of Visible Radiation*, *Physical Review Letters* **76**, 18 (1996).
- [19] C. O. Weiss, G. Kramer, B. Lipphardt, and H. Schnatz, *Frequency Measurement and Control, Advanced Techniques and Future Trends*, vol. 79 (Springer-Verlag, 2000), 1st ed.
- [20] J. L. Hall, *Nobel Lecture: Defining and measuring optical frequencies*, *Review of Modern Physics* **78**, 1279 (2006).
- [21] T. W. Hänsch, *Nobel Lecture: Passion for precision*, *Review of Modern Physics* **78**, 1297 (2006).
- [22] A. Baltuska et al., *Attosecond control of electronic processes by intense light fields*, *Nature* **421**, 611 (2003).
- [23] T. Steinmetz et al., *Laser Frequency Combs for Astronomical Observations*, *Science* **321**, 1335 (2008).
- [24] T. Udem, R. Holzwarth, and T. W. Hänsch, *Optical frequency metrology*, *Nature* **416**, 233 (2002).
- [25] T. Rosenband et al., *Frequency Ratio of Al^+ and Hg^+ Single-Ion*

- Optical Clocks; Metrology at the 17th Decimal Place*, Science **319**, 1808 (2008).
- [26] C. W. Chou, D. B. Hume, J. C. J. Koelemeij, D. J. Wineland, and T. Rosenband, *Frequency Comparison of Two High-Accuracy Al^+ Optical Clocks*, Physical Review Letters **104**, 070802 (2010).
- [27] A. Marian, M. C. Stowe, J. R. Lawall, D. Felinto, and J. Ye, *United Time-Frequency Spectroscopy for Dynamics and Global Structure*, Science **306**, 2063 (2004).
- [28] A. Marian, M. C. Stowe, D. Felinto, and J. Ye, *Direct Frequency Comb Measurements of Absolute Optical Frequencies and Population Transfer Dynamics*, Physical Review Letters **95**, 023001 (2005).
- [29] S. T. Cundiff and J. Ye, *Colloquium: Femtosecond optical frequency combs*, Review of Modern Physics **75**, 325 (2003).
- [30] G. D. Dickenson, M. L. Niu, E. J. Salumbides, J. Komasa, K. S. E. Eikema, K. Pachucki, and W. Ubachs, *Fundamental Vibration of Molecular Hydrogen*, Physical Review Letters **110**, 193601 (2013).
- [31] D. Z. Kandula, C. Gohle, T. J. Pinkert, W. Ubachs, and K. S. E. Eikema, *Extreme Ultraviolet Frequency Comb Metrology*, Physical Review Letters **105**, 063001 (2010).
- [32] M. Herrmann et al., *Feasibility of coherent xuv spectroscopy on the 1S-2S transition in singly ionized helium*, Physical Review A **79**, 052505 (2009).
- [33] E. Peik and C. Tamm, *Nuclear laser spectroscopy of the 3.5 eV transition in Th-229*, Europhysics Letters **61**, 181 (2003).
- [34] W. G. Rellergert, D. DeMille, R. R. Greco, M. P. Hehlen, J. R. Torgerson, and E. R. Hudson, *Constraining the Evolution of the Fundamental Constants with a Solid-State Optical Frequency Reference Based on the ^{229}Th Nucleus*, Physical Review Letters **104**, 200802 (2010).
- [35] A. Ozawa, W. Schneider, T. W. Hänsch, T. Udem, and P. Hommelhoff, *Phase-stable single-pass cryogenic amplifier for high repetition rate few-cycle laser pulses*, New Journal of Physics **11**, 083029 (2009).
- [36] A. Ruehl, A. Marcinkevicius, M. E. Fermann, and I. Hartl, *80W*,

- 120 fs Yb-fiber frequency comb*, Optics Express **35**, 3015 (2010).
- [37] S. Witte, R. T. Zinkstok, W. Ubachs, W. Hogervorst, and K. S. E. Eikema, *Deep-Ultraviolet Quantum Interference Metrology with Ultrashort Laser Pulses*, Science **307**, 400 (2005).
- [38] C. Gohle et al., *A frequency comb in the extreme ultraviolet*, Nature **436**, 234 (2005).
- [39] R. Jones, K. Moll, M. Thorpe, and J. Ye, *Phase-Coherent Frequency Combs in the Vacuum Ultraviolet via High-Harmonic Generation inside a Femtosecond Enhancement Cavity*, Physical Review Letters **94** (2005).
- [40] A. Cingöz, D. C. Yost, T. K. Allison, A. Ruehl, M. E. Fermann, I. Hartl, and J. Ye, *Direct frequency comb spectroscopy in the extreme ultraviolet*, Nature **482**, 68 (2012).
- [41] I. I. Sobelman, *Atomic Spectra and Radiative Transitions* (Springer-Verlag, 1996), 2nd ed.
- [42] M. Born and E. Wolf, *Principles of optics: electromagnetic theory of propagation, interference and diffraction of light* (Cambridge University Press, 1999), 7th ed.
- [43] J. C. Diels and W. Rudolph, *Ultrashort laser pulse phenomena* (Elsevier Academic Press, 2006), 2nd ed.
- [44] R. W. Boyd, *Nonlinear optics* (Elsevier Academic Press, 2003), 2nd ed.
- [45] G. P. Agrawal, *Nonlinear fiber optics* (Elsevier Academic Press, 1995), 2nd ed.
- [46] O. Svelto, *Principles of Lasers* (Plenum Press, 1998), 4th ed.
- [47] A. E. Siegman, *Lasers* (University Science Books, 1986), 1st ed.
- [48] R. Ell et al., *Generation of 5-fs pulses and octave-spanning spectra directly from a Ti:sapphire laser*, Optics Express **26**, 373 (2001).
- [49] J. C. Knight, T. A. Birks, P. S. J. Russell, and D. M. Atkin, *All-silica single-mode optical fiber with photonic crystal cladding*, Optics Letters **21**, 1547 (1996).
- [50] N. G. R. Broderick, T. M. Monro, P. J. Bennett, and D. J. Richardson, *Nonlinearity in holey optical fibers: measurement and future opportunities*, Optics Letters **24**, 1395 (1999).

- [51] J. K. Ranka, R. S. Windeler, and A. J. Stentz, *Visible continuum generation in air-silica microstructure optical fibers with anomalous dispersion at 800 nm*, *Optics Letters* **25**, 25 (2000).
- [52] A. Baltuška, T. Fuji, and T. Kobayashi, *Controlling the Carrier-Envelope Phase of Ultrashort Light Pulses with Optical Parametric Amplifiers*, *Physical Review Letters* **88**, 133901 (2002).
- [53] C. P. Hauri, P. Schlup, G. Arisholm, J. Biegert, and U. Keller, *Phase-preserving chirped-pulse optical parametric amplification to 17.3 fs directly from a Ti:sapphire oscillator*, *Optics Letters* **29**, 1369 (2004).
- [54] R. T. Zinkstok, S. Witte, W. Hogervorst, and K. S. E. Eikema, *High-power parametric amplification of 11.8-fs laser pulses with carrier-envelope phase control*, *Optics Letters* **30**, 78 (2005).
- [55] A. Renault et al., *Phase stability of terawatt-class ultrabroadband parametric amplification*, *Optics Letters* **32**, 2363 (2007).
- [56] Y. R. Shen, *The Principles of Nonlinear Optics* (Wiley-Interscience, 2002), 1st ed.
- [57] G. Cerullo and S. de Silvestri, *Ultrafast optical parametric amplifiers*, *Review of Scientific Instruments* **74**, 1 (2003).
- [58] S. Witte, *Terawatt-intensity few-cycle laser pulses - Optical parametric chirped pulse amplification and frequency comb spectroscopy*, Ph.D. thesis, Vrije Universiteit Amsterdam (2008).
- [59] I. N. Ross, P. Matousek, G. H. C. New, and K. Osvay, *Analysis and optimization of optical parametric chirped pulse amplification*, *Journal of the Optical Society of America B* **19**, 2945 (2002).
- [60] G. New, *Introduction to Nonlinear Optics* (Cambridge University Press, 2011), 1st ed.
- [61] W. H. Press, *Numerical recipes 3rd edition: The art of scientific computing* (Cambridge University Press, 2007), 3rd ed.
- [62] G. van Rossum, *Python tutorial, Technical Report CS-R9526*, Tech. rep., Centrum voor Wiskunde en Informatica (CWI), Amsterdam (1995).
- [63] W. Koechner, *Solid-state laser engineering*, vol. 1 (Springer-Verlag, 2006), 6th ed.

- [64] L. Frantz and J. S. Nodvik, *Theory of pulse propagation in a laser amplifier*, Journal of Applied Physics **34**, 2346 (1963).
- [65] J. E. Bernard, E. McCullough, and A. J. Alcock, *High gain, diode-pumped Nd:YVO₄ slab amplifier*, Optics Communications **109**, 109 (1994).
- [66] A. Agnesi, F. Pirzio, and G. Reali, *High gain solid-state modules for picosecond pulses amplification*, in *Society of Photo-Optical Instrumentation Engineers (SPIE) Conference Series*, vol. 7721, p. 7 (2010).
- [67] *High Q Laser (part of Spectra Physics)*, www.highqlaser.at.
- [68] *Time-Bandwidth Products AG*, www.time-bandwidth.com.
- [69] R. Lavi, S. Jackel, Y. Tzuk, M. Winik, E. Lebiush, M. Katz, and I. Paiss, *Efficient pumping scheme for neodymium-doped materials by direct excitation of the upper lasing level*, Applied Optics **38**, 7382 (1999).
- [70] L. Sun et al., *880 nm LD pumped passive mode-locked TEM₀₀ Nd:YVO₄ laser based on SESAM*, Laser Physics Letters **7**, 711 (2010).
- [71] T. C. Briles, D. C. Yost, A. Cingöz, J. Ye, and T. R. Schibli, *Simple piezoelectric-actuated mirror with 180 kHz servo bandwidth*, Optics Express **18**, 9739 (2010).
- [72] S. Witte, R. T. Zinkstok, A. L. Wolf, W. Hogervorst, W. Ubachs, and K. S. E. Eikema, *A source of 2 terawatt, 2.7 cycle laser pulses based on noncollinear optical parametric chirped pulse amplification*, Optics Express **14**, 8168 (2006).
- [73] D. Herrmann, L. Veisz, R. Tautz, F. Tavella, K. Schmid, V. Pervak, and F. Krausz, *Generation of sub-three-cycle, 16 TW light pulses by using noncollinear optical parametric chirped-pulse amplification*, Optics Letters **34**, 2459 (2009).
- [74] S. Klingebiel et al., *High energy picosecond Yb:YAG CPA system at 10 Hz repetition rate for pumping optical parametric amplifiers*, Optics Express **19**, 5357 (2011).
- [75] D. J. Farrell and M. J. Damzen, *High power scaling of a passively modelocked laser oscillator in a bounce geometry*, Optics Express **15**, 205 (2007).

- [76] K. Nawata, M. Okida, K. Furuki, K. Miyamoto, and T. Omatsu, *Sub-100 W picosecond output from a phase-conjugate Nd:YVO₄ bounce amplifier*, Optics Express **17**, 20816 (2009).
- [77] M. Jelinek, V. Kubeček, M. Čech, and P. Hiršl, *0.8 mJ quasi-continuously pumped sub-nanosecond highly doped Nd:YAG oscillator-amplifier laser system in bounce geometry*, Laser Physics Letters (2011).
- [78] A. Agnesi, L. Carrà, F. Pirzio, G. Reali, F. Tomaselli, D. Scarpa, and C. Vacchi, *Amplification of a low-power picosecond Nd:YVO₄ laser by a diode-laser side-pumped grazing-incidence slab amplifier*, IEEE Journal of Quantum Electronics **42**, 772 (2006).
- [79] Y. Sato and T. Taira, *Comparative study on the spectroscopic properties of Nd:GdVO₄ and Nd:YVO₄ with hybrid process*, IEEE Journal on Selected Topics in Quantum Electronics **11**, 613 (2005).
- [80] R. D. Peterson, H. P. Jenssen, and A. Cassanho, *Investigation of the spectroscopic properties of Nd:YVO₄*, Proc. OSA TOPS, Advanced Solid-State Lasers, M. E. Fermann and L. R. Marshall, eds **68**, 294 (2002).
- [81] Y. Sato and T. Taira, *Spectroscopic properties of neodymium-doped yttrium orthovanadate single crystals with high-resolution measurement*, Japanese Journal of Applied Physics **41**, 5999 (2002).
- [82] A. Agnesi, P. Dallochio, S. Dell'Acqua, F. Pirzio, and G. Reali, *High peak power sub-nanosecond MOPA laser system*, in *Advanced Solid-State Lasers, 4th EPS-QEOD Europhoton Conference, Hamburg, paper WeB5* (2010).
- [83] J. Morgenweg and K. S. E. Eikema, *Tailored pulse sequences from an 880 nm pumped Nd:YVO₄ bounce amplifier*, Optics Letters **37**, 208 (2012).
- [84] Y. F. Chen, *Design criteria for concentration optimization in scaling diode end-pumped lasers to high powers: influence of thermal fracture*, IEEE Journal of Quantum Electronics **35**, 234 (1999).
- [85] T. J. Pinkert, D. Z. Kandula, C. Gohle, I. Barmes, J. Morgenweg, and K. S. E. Eikema, *Widely tunable extreme UV frequency comb generation*, Optics Letters **36**, 2026 (2011).

- [86] D. Noom, S. Witte, J. Morgenweg, R. K. Altmann, and K. S. E. Eikema, *High-energy, high-repetition-rate picosecond pulses from a quasi-CW diode pumped Nd:YAG system*, *Optics Letters* **38**, 3021 (2013).
- [87] M. F. Kling et al., *Control of Electron Localization in Molecular Dissociation*, *Science* **312**, 246 (2006).
- [88] A. Antognini et al., *Illuminating the proton radius conundrum: the μHe^+ Lamb shift*, *Canadian Journal of Physics* **89**, 47 (2011).
- [89] E. J. Salumbides, G. D. Dickenson, T. I. Ivanov, and W. Ubachs, *QED Effects in Molecules: Test on Rotational Quantum States of H_2* , *Physical Review Letters* **107**, 43005 (2011).
- [90] R. T. Zinkstok, S. Witte, W. Ubachs, W. Hogervorst, and K. S. E. Eikema, *Frequency comb laser spectroscopy in the vacuum-ultraviolet region*, *Physical Review A* **73**, 061801 (2006).
- [91] J. Morgenweg and K. S. E. Eikema, *A 1.8 mJ, picosecond Nd:YVO₄ bounce amplifier pump front-end system for high-accuracy XUV-frequency comb spectroscopy*, *Laser Physics Letters* **9**, 781 (2012).
- [92] D. Z. Kandula, C. Gohle, T. J. Pinkert, W. Ubachs, and K. S. E. Eikema, *XUV frequency-comb metrology on the ground state of helium*, *Physical Review A* **84**, 062512 (2011).
- [93] D. Z. Kandula et al., *Ultrafast double-pulse parametric amplification for precision Ramsey metrology*, *Optics Express* **16**, 7071 (2008).
- [94] M. Takeda, H. Ina, and S. Kobayashi, *Fourier-transform method of fringe-pattern analysis for computer-based topography and interferometry*, *Journal of the Optical Society of America* **72**, 156 (1982).
- [95] A. L. Wolf, *Frequency comb spectroscopy on trapped calcium ions*, Ph.D. thesis, Vrije Universiteit Amsterdam (2011).
- [96] S. Witte and K. S. E. Eikema, *Ultrafast Optical Parametric Chirped-Pulse Amplification*, *IEEE Journal on Selected Topics in Quantum Electronics* **18**, 296 (2012).
- [97] H. P. Li, C. H. Kam, Y. L. Lam, and W. Ji, *Femtosecond Z-scan measurements of nonlinear refraction in nonlinear optical crystals*, *Optical Materials* **15**, 237 (2001).

- [98] R. R. Ernst, *Application of Fourier Transform Spectroscopy to Magnetic Resonance*, Review of Scientific Instruments **37**, 93 (1966).
- [99] S. P. Davis, M. C. Abrams, and J. W. Brault, *Fourier transform spectrometry* (Elsevier Academic Press, 2001), 1st ed.
- [100] M. C. Stowe, M. J. Thorpe, A. Pe'er, J. Ye, J. E. Stalnaker, V. Gerginov, and S. A. Diddams, *Direct frequency comb spectroscopy*, Advances in Atomic, Molecular, and Optical Physics **55**, 1 (2008).
- [101] A. Marsman, M. Horbatsch, and E. A. Hessels, *Shifts due to neighboring resonances for microwave measurements of the 2^3P fine structure of helium*, Physical Review A **86**, 012510 (2012).
- [102] S. Cavalieri, R. Eramo, M. Materazzi, C. Corsi, and M. Bellini, *Ramsey-Type Spectroscopy with High-Order Harmonics*, Physical Review Letters **89**, 133002 (2002).
- [103] R. Eramo, S. Cavalieri, C. Corsi, I. Lontos, and M. Bellini, *Method for High-Resolution Frequency Measurements in the Extreme Ultraviolet Regime: Random-Sampling Ramsey Spectroscopy*, Physical Review Letters **106**, 213003 (2011).
- [104] J. Morgenweg and K. S. E. Eikema, *Multi-delay, phase coherent pulse pair generation for precision Ramsey-frequency comb spectroscopy*, Optics Express **21**, 5275 (2013).
- [105] E. Gomez, S. Aubin, L. A. Orozco, and G. D. Sprouse, *Lifetime and hyperfine splitting measurements on the $7s$ and $6p$ levels in rubidium*, Journal of the Optical Society of America B **21**, 2058 (2004).
- [106] A. Bartels, C. W. Oates, L. Hollberg, and S. A. Diddams, *Stabilization of femtosecond laser frequency combs with subhertz residual linewidths*, Optics Letters **29**, 1081 (2004).
- [107] H. C. Chui, M. S. Ko, Y. W. Liu, J. T. Shy, J. L. Peng, and H. Ahn, *Absolute frequency measurement of rubidium $5S-7S$ two-photon transitions with a femtosecond laser comb optics*, Optics Letters **30**, 842 (2005).
- [108] I. Barmes, S. Witte, and K. S. E. Eikema, *High-Precision Spectroscopy with Counterpropagating Femtosecond Pulses*, Physical Review Letters **111**, 023007 (2013).

- [109] J. E. Stalnaker, V. Mbele, V. Gerginov, T. M. Forter, S. A. Diddams, L. Hollberg, and C. E. Tanner, *Femtosecond frequency comb measurement of absolute frequencies and hyperfine coupling constants in cesium vapor*, Physical Review A **81**, 043840 (2010).
- [110] A. Antognini et al., *Proton Structure from the Measurement of 2S-2P Transition Frequencies of Muonic Hydrogen*, Science **339**, 417 (2013).
- [111] A. Ozawa and Y. Kobayashi, *Chirped-pulse direct frequency-comb spectroscopy of two-photon transitions*, Physical Review A **86**, 022514 (2012).
- [112] W. M. Hartmann, *Signals, Sound, and Sensation* (American Inst. of Physics, 2004), corr. 5th printing ed.
- [113] R. D. Cowan, *The theory of atomic structure and spectra (Los Alamos Series in Basic and Applied Sciences, vol. 3)* (Univ. of California Press, 1981).
- [114] J. W. Farley and W. H. Wing, *Accurate calculation of dynamic Stark shifts and depopulation rates of Rydberg energy levels induced by blackbody radiation. Hydrogen, helium, and alkali-metal atoms*, Physical Review A **23**, 2397 (1981).
- [115] B. Cagnac, B. Grynberg, and F. Biraben, *Spectroscopie d'absorption multiphotonique sans effet Doppler*, Journal de Physique (France) **34**, 845 (1973).
- [116] S. A. Webster, P. Taylor, M. Roberts, G. P. Barwood, and P. Gill, *Kilohertz-resolution spectroscopy of the $^2S_{1/2}$ - $^2F_{7/2}$ electric octupole transition in a single 171Yb^+ ion*, Physical Review A **65**, 052501 (2002).
- [117] G. K. Woodgate, *Elementary Atomic Structure* (Oxford University Press, 1983), 2nd ed.
- [118] P. Fendel, S. D. Bergeson, T. Udem, and T. W. Hänsch, *Two-photon frequency comb spectroscopy of the 6s-8s transition in cesium*, Optics Letters **32**, 701 (2007).
- [119] Wolf et al., *Direct Frequency Comb Spectroscopy of Trapped Ions*, Physical Review Letters **102**, 223901 (2009).
- [120] J. Morgenweg, I. Barmes, and K. S. E. Eikema, *Ramsey-comb spectroscopy with ultrashort Intense laser pulses*, Nature Physics

- 10**, 30 (2014).
- [121] F. Riehle, *Frequency Standards: Basics and Applications* (Wiley-VCH, 2004), 1st ed.
- [122] E. Salumbides, J. Koelemeij, J. Komasa, K. Pachucki, K. Eikema, and W. Ubachs, *Bounds on fifth forces from precision measurements on molecules*, *Physical Review D* **87**, 112008 (2013).
- [123] C. G. Parthey et al., *Improved Measurement of the Hydrogen 1S-2S Transition Frequency*, *Physical Review Letters* **107**, 203001 (2011).
- [124] B. Roth, U. Fröhlich, and S. Schiller, *Sympathetic Cooling of $^4\text{He}^+$ Ions in a Radio-Frequency Trap*, *Physical Review Letters* **94**, 053001 (2005).
- [125] W. D. Kammler, *A first course in Fourier analysis* (Cambridge University Press, 2010), 2nd ed.
- [126] C. Foot, *Atomic physics* (Oxford University Press, 2005), 1st ed.
- [127] L. Allen and J. H. Eberly, *Optical Resonance and Two-Level Atoms* (Dover Publications, 1988), 1st ed.
- [128] C. Cohen-Tannoudji, B. Diu, and F. Laloë, *Quantum mechanics* (John Wiley & Sons, 1977), 1st ed.
- [129] D. Felinto, C. A. C. Bosco, L. H. Acioli, and S. S. Vianna, *Accumulative effects in temporal coherent control*, *Physical Review A* **64**, 063413 (2001).
- [130] D. Felinto, C. A. C. Bosco, L. H. Acioli, and S. S. Vianna, *Coherent accumulation in two-level atoms excited by a train of ultrashort pulses*, *Optics Communications* **215**, 69 (2003).
- [131] D. Felinto, L. H. Acioli, and S. S. Vianna, *Accumulative effects in the coherence of three-level atoms excited by femtosecond-laser frequency combs*, *Physical Review A* **70**, 043403 (2004).
- [132] R. T. Zinkstok, *Direct frequency comb spectroscopy in the vacuum ultraviolet*, Ph.D. thesis, Vrije Universiteit Amsterdam (2008).

LIST OF PUBLICATIONS

This thesis is based on the following publications:

CHAPTER 3 (SECTION 3.2):

Tailored pulse sequences from an 880 nm pumped Nd:YVO₄ bounce amplifier

J. Morgenweg and K. S. E. Eikema
Optics Letters **37**, 208-210 (2012).

CHAPTER 3 (SECTION 3.3):

A 1.8 mJ, picosecond Nd:YVO₄ bounce amplifier pump front-end system for high-accuracy XUV-frequency comb spectroscopy

J. Morgenweg and K. S. E. Eikema
Laser Physics Letters **9**, 781-785 (2012).

CHAPTER 4:

Multi-delay, phase coherent pulse pair generation for precision Ramsey-frequency comb spectroscopy

J. Morgenweg and K. S. E. Eikema
Optics Express **21**, 5275-5286 (2013).

CHAPTER 5:

Ramsey-comb spectroscopy with intense ultrashort laser pulses

J. Morgenweg, I. Barmes and K. S. E. Eikema
Nature Physics **10**, 30-33 (2014).

CHAPTER 6:

Ramsey-comb spectroscopy: Theory and signal analysis

J. Morgenweg and K. S. E. Eikema
Accepted for publication in Physical Review A.

Publications to which the author contributed but that have not been reproduced in this thesis:

- *High-energy, high-repetition-rate picosecond pulses from a quasi-CW diode pumped Nd:YAG system*
D. W. E. Noom, S. Witte, J. Morgenweg, R. K. Altmann and K. S. E. Eikema
Optics Letters **38**, 3021-3023 (2013).
- *Widely tunable extreme UV frequency comb generation*
T. J. Pinkert, D. Z. Kandula, C. Gohle, I. Barmes, J. Morgenweg and K. S. E. Eikema
Optics Letters **36**, 2026-2028 (2011).
- *Direct frequency-comb spectroscopy of a dipole-forbidden clock transition in trapped $^{40}\text{Ca}^+$ ions*
A. L. Wolf, J. Morgenweg, J. C. Koelemeij, S. A. van den Berg, W. Ubachs and K. S. E. Eikema
Optics Letters **36**, 49-51 (2011).

SUMMARY

The most accurate, absolute measurements that we can perform are time/frequency measurements simply because the physical unit of the second is the most accurately defined SI-unit. Since 1967, the second is defined as the duration of 9,192,631,770 periods of a hyperfine transition frequency in ^{133}Cs and commercial products are available for distributing this frequency standard at the 10^{-13} -level in many metrology laboratories around the world. With the help of optical frequency combs (FC) based on mode-locked lasers, this remarkable accuracy can be transferred all the way from the microwave to the optical domain, thus enabling high-precision spectroscopy on atomic and molecular systems. Beyond their use as calibration tools for referencing continuous-wave lasers, FCs can also be employed themselves as the spectroscopy lasers. This very successful technique of direct FC spectroscopy combines high accuracy with high laser intensities and broad wavelength coverage from the pulsed laser oscillators. However, there are a range of applications that require even higher intensities, e.g. for the excitation of very weak transitions or in order to convert the wavelength of the FC to spectral regions inaccessible by laser oscillators.

In order to reach ultrahigh pulse intensities and energies, our group has followed the unique approach of coherently amplifying only selected (two) pulses derived from a regular FC pulse train. Because the average power can be kept low, this approach allows for a significantly higher amplification level than alternative methods based on, e.g., full repetition rate amplification in conjunction with enhancement cavities. While leading to the first high-precision measurement in the extreme ultraviolet wavelength region <60 nm, the initial approach nevertheless sacrificed part of the beauty of the underlying FC as only single, isolated transitions could be measured and the accuracy was limited by the maximum delay and phase shifts during the amplification process. To overcome this limitations a novel spectroscopic method has been developed, “Ramsey-comb spectroscopy”, which is introduced and demonstrated in the course of this thesis. Although the Ramsey-comb method still relies on amplified FC pulse pairs, the new ability to coherently change the inter-pulse delay over a wide range enables a fundamentally new way of measuring and

analyzing the spectroscopic signals. We show that the combination of high-energy laser pulses with the accuracy and resolution of FCs provides an extremely versatile tool for high-precision spectroscopy. A more detailed introduction and motivation for producing high peak power FC pulses is given in Ch. 1 along with a short outline of the thesis, whose content is summarized in the following paragraphs.

In order to efficiently discuss the technical and conceptual challenges in the course of this thesis, first some particularly relevant background is reviewed in Ch. 2. Starting from Maxwell's fundamental equations, the concept of temporal and spectral envelopes for laser pulses is derived and applied to study physical effects such as propagation and dispersion. Going from single pulses to pulse sequences, one of the key elements of the Ramsey-comb method is introduced, the optical FC, including a discussion of how FCs are implemented in practice. Finally, the theory of two different approaches for amplifying laser pulses is introduced: the concept of optical parametric amplification, which enables the phase-coherent amplification of FC pulses, and the more conventional amplification in laser gain media, which is employed to create the high-energy pump pulses for the parametric amplification.

Realizing Ramsey-comb spectroscopy requires a complex experimental laser system for producing high-energy, multi-delay coherent laser pulse pairs. The description of the developed system starts in Ch. 3, which contains a detailed discussion of the *pump* amplifier system for producing the high-energy pump pulse pairs for the parametric amplifier. First, the home-built, passively mode-locked pump oscillator is described, whose output is adjusted in terms of pulse duration and center wavelength. From the full pulse train, two pulses are selected via programmable pulse pickers at variable delays. Subsequently, these pulses are amplified in a two-stage, ultrahigh-gain pre-amplifier, boosting the pulse energy from less than 100 pJ to the 1 mJ-level. The pre-amplifier is followed by either a flashlamp-pumped or a diode-pumped post-amplifier. Altogether, the developed laser amplifier system is capable of producing 1064 nm pump pulse pairs at the 100 mJ-level with inter-pulse delays of multiples of the cavity round-trip time (~ 8 ns) of the master pump oscillator well into the microsecond range. Furthermore, the inter-pulse delay can quickly be changed while keeping the optical paths in the amplifier the same, thus minimizing wavefront deviations for the second pump pulse as a function of delay time.

The amplified pump pulse pairs from the system described in Ch. 3 are used to pump an optical parametric amplifier, which in turn selec-

tively amplifies pulse pairs from a synchronized FC oscillator operating at the same repetition rate as the pump oscillator. The performance of the parametric amplifier system, in particular the phase stability of the mJ-level amplified FC pulses, is the main subject of Ch. 4. First, the home-built Ti:sapphire FC is described, which acts as the seed for the parametric amplifier. A technical overview of the parametric amplifier system and the electronic synchronization scheme is then followed by an extensive study of the phase shift induced by the amplifier, both via numerical simulations and direct measurements. It is established that although the amplified FC pulses can exhibit a differential phase shift of a few 100 mrad, this phase shift remains effectively constant when changing the inter-pulse delay. This important outcome makes the experimental system suitable for high-accuracy Ramsey-comb spectroscopy.

Having concluded the detailed description of the developed laser system, Ch. 5 shows the capabilities of Ramsey-comb spectroscopy via a measurement of complex two-photon transitions in atomic rubidium and cesium. Owing to the good signal-to-noise ratio and a counter-propagating excitation scheme to reduce Doppler broadening, Ramsey signals are obtained at more than 40 different macro delays (in steps of 8 ns), which in the case of rubidium is more than four times the lifetime of the upper state. With the help of a novel time-domain fitting algorithm, the excited transition frequencies are determined with an accuracy better than 10 kHz including systematic uncertainties. For the weak transitions in cesium, this accuracy level represents a more than thirty-fold improvement to previous spectroscopic results. This shows that the Ramsey-comb method can significantly outperform traditional forms of spectroscopy on transitions that are too weak to be easily excited with conventional unamplified FCs or continuous-wave lasers.

After its first introduction in the previous chapter, a more comprehensive analytical framework of the Ramsey-comb method is presented in Ch. 6. Starting from Ramsey's originally derived equation describing excitation with separated oscillating fields, Ramsey signals from different macro delays are combined on a global time axis. In the frequency domain, this combination of individual measurements can be used to derive a "synthetic" excitation spectrum that resembles spectra obtained from traditional direct FC spectroscopy. However, it is shown that as opposed to traditional FC spectra, the spectral analysis is affected by additional interferences that severely complicate the frequency determination if more than one resonance is excited. Fortunately, the time-

domain analysis is found to be much more robust as it relies solely on the temporal phases of the individual Ramsey scans. This has the additional advantage of being insensitive towards common spectral line-broadening effects and (transition-independent) constant phase shifts, due to, e.g., the amplification process or the AC-Stark effect from the excitation pulses themselves. Finally, the performance of the presented time-domain fitting approach is investigated via numerical simulations for different parameter sets including cases of transition-dependent broadening mechanisms and phase shifts. Within the simulation uncertainties of a few kHz, no sizeable systematic effects on the fitting results are encountered.

The thesis is concluded by an outlook in Ch. 7, which describes possible upgrades of the experimental system as well as interesting future targets for Ramsey-comb spectroscopy such as H_2 and He^+ .

SAMENVATTING

De Nederlandse titel van dit proefschrift is “Ramsey-kamspectroscopie”.

De meest nauwkeurige absolute metingen die we kunnen uitvoeren zijn tijd- of frequentiemetingen, simpelweg omdat de fysische eenheid van de seconde de meest accuraat gedefinieerde SI-eenheid is. Sinds 1967 is de seconde gedefinieerd als de duur van 9,192,631,770 periodes van een hyperfijnovergang in ^{133}Cs , en commerciële producten zijn beschikbaar voor de distributie van deze frequentiestandaard op een niveau van 10^{-13} in vele metrologielaboratoria over de wereld. Met behulp van optische frequentiekammen (FK), gebaseerd op gepulste lasers, kan deze bijzondere nauwkeurigheid overgebracht worden van het microgolfdomein naar optische frequenties, en dus hoge-precisie spectroscopie op atomaire en moleculaire systemen mogelijk maken. Buiten het gebruik als ijkingsgereedschap voor het kalibreren van continue lasers kunnen FK's ook zelf gebruikt worden als spectroscopielasers. Deze succesvolle techniek van directe FK-spectroscopie combineert een hoge nauwkeurigheid met de hoge laserintensiteiten en het grote golflengtebereik van gepulste laseroscillatoren. Er zijn echter vele toepassingen die nog hogere intensiteiten nodig hebben, bijvoorbeeld voor de excitatie van zeer zwakke overgangen of om de golflengtes van de FK naar spectrale gebieden over te brengen die onbereikbaar zijn voor oscillatoren zelf.

Om ultrahoge pulsintensiteiten en energieën te bereiken heeft onze groep een unieke aanpak gebruikt waarbij (twee) geselecteerde pulsen uit een FK-pulstrein coherent worden versterkt. Omdat het gemiddelde vermogen laag gehouden kan worden, maakt deze aanpak een significant grotere versterking mogelijk dan alternatieve methoden, zoals bijvoorbeeld gebaseerd op versterking op de volle repetitiefrequentie gecombineerd met verdere versterking in trillholtes. Ook al heeft de oorspronkelijke aanpak geleid tot de eerste hoge-precisiemetingen in het extreem-ultraviolette golflengtegebied <60 nm, toch moest er wat van de elegantie van de FK worden opgeofferd omdat alleen individuele, geïsoleerde overgangen gemeten konden worden en de nauwkeurigheid gelimiteerd werd door de maximale pulsafstand en faseverschuivingen bij het versterkingsproces. Om deze beperkingen te overwinnen is een nieuwe

methode ontwikkeld, “Ramsey-kamspectroscopie”, die geïntroduceerd en gedemonstreerd wordt in dit proefschrift. Ondanks dat de Ramsey-kammethode nog steeds gebaseerd is op versterkte FK-pulsparen, biedt de nieuwe mogelijkheid om de vertraging tussen pulsen coherent te veranderen over een groot bereik een fundamentele nieuwe methode om spectroscopische signalen te meten en analyseren. We laten zien dat de combinatie van hoge-energie laserpulsen met de nauwkeurigheid en resolutie van FK’s zorgt voor een extreem veelzijdig gereedschap voor hoge-precisie-spectroscopie. Een meer gedetailleerde introductie en motivatie voor het maken van pulsen met hoog piekvermogen wordt gegeven in Hfdst. 1, samen met een kort overzicht van het proefschrift, waarvan de inhoud wordt samengevat in de volgende paragrafen.

Om de technische en conceptuele uitdagingen van het werk efficiënt te kunnen bediscussiëren wordt eerst een overzicht van de relevante achtergrondinformatie gegeven in Hfdst. 2. Beginnend met de fundamentele vergelijkingen van Maxwell wordt het concept van temporele en spectrale vormen van laserpulsen afgeleid en toegepast om fysische effecten zoals propagatie en dispersie te bestuderen. Bij de overstap van enkele pulsen naar pulssequenties wordt één van de belangrijkste elementen van de Ramsey-kammethode geïntroduceerd, de optische FK, inclusief een discussie over hoe FK’s in de praktijk geïmplementeerd worden. Als laatste wordt de theorie van twee verschillende methoden voor het versterken van laserpulsen geïntroduceerd: Het concept van parametrische versterking, die het fase-coherent versterken van FK-pulsen mogelijk maakt, en de meer conventionele versterking in laserversterkingsmedia, die wordt gebruikt om “pomp”-pulsen met hoge energie te genereren voor de parametrische versterking.

Het realiseren van Ramsey-kamspectroscopie vereist een complex experimenteel lasersysteem voor het produceren van hoge-energie laserpulsparen met variabele vertraging. De beschrijving van het systeem begint in Hfdst. 3, die een gedetailleerde discussie bevat van het *pomp*-versterkersysteem voor het produceren van pulsparen met hoge energie voor de parametrische versterker. Eerst wordt de door ons gebouwde passief-“modengekoppelde” gepulste pomp-oscillator beschreven waarvan de pulsduur en centrale golflengte aangepast kan worden. Van de volledige pulstrein worden twee pulsen geselecteerd op een variabele tijdsafstand via programmeerbare pulskiezers. Daarna worden deze pulsen versterkt in een tweetraps-voorversterker met hoge versterking die de pulsenergie opstuwt van minder dan 100 pJ tot het 1 mJ-niveau. De voorversterker wordt gevolgd door een flitslamp- of diodegepompte

naversterker. Het laserversterkingssysteem is in staat om 1064 nm pomp-pulsparen op 100 mJ-niveau te produceren met een vertraging tussen de pulsen die kan oplopen tot vele microseconden, in stappen van de omlooptijd (~ 8 ns) van de hoofd-pomposcillator. Bovendien kan de tijd tussen pulsen snel veranderd worden terwijl het optische pad in de versterker hetzelfde blijft, waarmee golffrontverstoringen geminimaliseerd worden voor de tweede pomppuls als functie van de vertragingstijd.

De versterkte pulsparen van het systeem wat beschreven wordt in Hfdst. 3 kunnen worden gebruikt om een optische parametrische versterker mee te pompen, die op zijn beurt selectief pulsparen van een gesynchroniseerde frequentiekamoscillator versterkt die op dezelfde repetitiefrequentie opereert als de oscillator van het pomplasersysteem. De prestaties van het parametrische-versterkersysteem, in het bijzonder de fasestabiliteit van de tot mJ-niveau versterkte pulsen, is het hoofdonderwerp van Hfdst. 4. Als eerste wordt de zelfgebouwde Ti:saffier-FK beschreven die dienst doet als beginpunt (“kiem”) voor de parametrische versterker. Een technisch overzicht van het parametrische-versterkersysteem en de opstelling voor de elektronische synchronisatie wordt dan gevolgd door een uitgebreide studie via zowel numerieke simulaties als directe metingen van de faseverschuiving die geïntroduceerd wordt door de versterker. Het wordt bevestigd dat zelfs als de versterkte FK-pulsen een differentieel faseverschil hebben van 100 mrad, dat dit faseverschil afdoende constant blijft wanneer de tijdafstand tussen de pulsen veranderd wordt. Dit belangrijke resultaat maakt het experimentele systeem geschikt voor Ramsey-kamspectroscopie met hoge nauwkeurigheid.

Na de gedetailleerde beschrijving van het ontwikkelde lasersysteem, laat Hfdst. 5 zien wat de mogelijkheden zijn van Ramsey-kamspectroscopie via een meting van complexe twee-fotonovergangen in atomair rubidium en cesium. Vanwege de goede signaal-ruisverhouding, en een configuratie met laserbundels in tegenovergestelde richting om Dopplerverbreding te reduceren, kunnen Ramsey-signalen verkregen worden op meer dan 40 verschillende macrovertragingen (in stappen van 8 ns), wat in het geval van rubidium meer dan vier keer de levensduur van de bovenste toestand is. Met behulp van een nieuw tijddomein-fit algoritme worden de frequenties van de aangeslagen overgangen bepaald met een nauwkeurigheid beter dan 10 kHz, inclusief systematische onzekerheden. Voor de zwakke overgangen in cesium is dit een meer dan dertigvoudige verbetering van eerdere spectroscopische resultaten. Dit laat zien dat de Ramsey-kammethode traditionele vormen van spectroscopie kan overtr-

effen bij overgangen die te zwak zijn om makkelijk geëxciteerd te worden met conventionele onversterkte FK's (of continue lasers).

Na de eerste introductie in het vorige hoofdstuk, wordt een uitgebreider analytisch raamwerk gepresenteerd van de Ramsey-kammethode in Hfdst. 6. Beginnend met Ramsey's originele afgeleide vergelijking die het exciteren met gescheiden oscillerende velden beschrijft, worden Ramsey-signalen met verschillende macrovertragingen gecombineerd op een globale tijdas. In het frequentiedomein kan deze combinatie van individuele meetresultaten gebruikt worden om een "synthetisch" excitatiespectrum af te leiden dat lijkt op spectra die verkregen worden met traditionele directe-kamspectroscopie. Echter, er wordt gedemonstreerd dat in tegenstelling tot traditionele FK-spectra, de spectrale analyse beïnvloed wordt door extra interferenties die de frequentiebepaling ernstig compliceren als er meer dan één resonantie aangeslagen wordt. Gelukkig blijkt de tijddomein-analyse een stuk robuuster te zijn omdat die alleen op de temporele fases van de individuele Ramsey-metingen berust. Dit heeft als extra voordeel dat het niet gevoelig is voor algemene spectraal-lijverbredingseffecten en (overgangsonafhankelijke) constante faseverschuivingen zoals door het versterkingsproces, of het AC-Stark-effect als gevolg van de excitatiepulsen zelf. Als laatste worden de prestaties van het tijddomein-fitten onderzocht via numerieke simulaties voor verschillende parameterverzamelingen, inclusief gevallen van overgangsafhanke-lijke verbredingsmechanismen en faseveranderingen. Binnen de simulatieonauwkeurigheden van een paar kHz worden geen aanzienlijke systematische effecten op de fitresultaten gevonden.

Het proefschrift wordt afgerond met een vooruitblik in Hfdst. 7 waarin mogelijke verbeteringen van het experimentele systeem worden beschreven, evenals interessante toekomstige doelen voor Ramsey-kamspectroscopie zoals H_2 en He^+ .

DANKWOORD

So here we are, the most-read part of a thesis. Not many people, in particular not the smart ones, would try to get a PhD without the help of other people. As much as I prefer the spoken to the written word when it comes to social relations, it is now the time to share some credits and to thank the large number of people which contributed to the good memories that I have of my time in Amsterdam. Among all these people, one person holds his impregnable pole position; other people will follow more or less alphabetically.

K., it was you that convinced me to come to Amsterdam (not that I could follow your explanation pace at the day of the interview, but it sounded impressive and you appeared to have a good sense of humour*) and kept me motivated in particular throughout the more exhausting and less rewarding phases of my experimental work. I got a great number of pearls of wisdom from your extensive technical and physical expertise (including in fields such as plumbing) and you were heavily involved in all stages of my PhD project, and that on a level much higher than supervisors typically do.

A., thanks for taking me as your apprentice at a rather stressed stage of your PhD. From you I learned the ropes of frequency combs and got valuable advice of how to master a PhD in experimental physics.

A., I will remember you as a very pleasant deipnosophist, for you taste of weird movies and as a talented “Magician” (sorry for the bad pun).

A., we were lucky that you decided to become a temporary member of our group as you possess a lot of practical knowledge that you are also very willing to share. Hope to see you soon at some laser conference.

A., late evening worker but still never losing his smile. I will miss our nice board and card game rounds.

A., pity that you did not come earlier and stayed longer at the VU, but fortunately we managed anyway to have a range of social and cultural events together and I hope this will continue so in the future despite the more challenging logistics.

*I intentionally kept the British spelling here.

C., you are the most helpful person I know (and the slowest eater) and I very much enjoyed and will remember the deep discussions about the important things in life that we had over the last years.

D., it was very nice to share some of the laser-development load with another thriving scientist. I like your attitude on doing only the things you like, hold on to it. And provide me with more of these brain teasers from time to time.

D., C., R., A., thank you for the pioneering work that provided the prerequisite for my PhD achievements.

D., V., thanks for sharing your python knowledge with me and the nice company; I am looking forward to hear about your promising scientific career!

E., you are the man for very pleasant and fruitful physical (or other topics including “theological”) discussions and I would have enjoyed to work with you on some projects together - but who knows, maybe it will happen at USC some day.

G., Alter, it is very hard to be in bad mood when you are around. You were a great skiing companion, patient surf teacher and motivated German student. All the best down under.

I., it was fun starting with you together on the project and we had a good time on various conferences and also non-work related get-togethers. Thanks also for your stimulating challenges of my explanations, which helped to progress and prepare.

J., it was great to still benefit for a few years from your experience, starting from drilling holes to advices for my personal fitness. But on top of this I will always remember a lot of nice conversations over a beer and listening to some great vinyl.

J., again less for work-related but all the more from the social point of view it is a real pity to move away from such a nice, smart and caring person with a refreshing idealistic attitude. Let’s keep in touch.

T., we had a good time at various non-work related events and I hope we will manage soon to visit you and P. over a pint in your lovely neighborhood in the island’s capital.

M., you had a big share on making my time in Amsterdam in particular outside work very enjoyable, also by introducing me to your country, family and a great number of your friends. I will work hard on keeping our friendship despite the supposedly longer distance in the future.

M., many thanks for all the administrative work and having an endless supply of all stationary items I could come up with.

R., it was actually thanks to you (an advert in the DPG journal) that I eventually started my PhD at the VU.

R., thanks for continuing with “my baby”. It was fun to transfer part of my knowledge to you and I hope you will keep my up to date concerning the future experiments.

R., fortunately I did not have to bother you with many projects but you left nothing to complain with the ones you did.

S., asking you for help with a problem was typically the most effective way to get some progress, and a lot of the work described in this thesis greatly benefitted from your previous achievements and advice. And of course I will also remember our various common social activities such as when we gained everlasting fame as Team Schlaaaaaaand.

T., I very much appreciate your altruistic attitude in particular when it comes to IT (Linux, of course) and hands-on electrical-engineering advice, but also thank you very much for helping me getting started with the complex experimental setup.

T., O., I was always looking forward to meet you guys at various get-togethers for some nice conversations. Keep on smashing T.!

W., thanks for providing a professional work environment but also assuring nice get-togethers be it on mountains or in your private backyard.

W., J., S., M., thanks for being always open for questions and share your profound knowledge on spectroscopy and related experimental challenges.

Z., A., M., H., I will remember the nice conversations that we had at various occasions, in particular exchanging many details about different cultures. I hope I will visit you all one day in your home countries!

A big collective thank goes to the teams of the electronic and mechanical workshops at the VU for repairing, developing, manufacturing and counseling in the great number of situations that came across during my PhD time.

Moreover, I also like to thank the Heeren 1 van SVU for giving “de Duitse” the opportunity of a healthy escape from work. We had some great times before, during, and after the matches.

Finally, some signs of gratitude to a few more people less related to the University, whose contributions nonetheless deserve to be mentioned here.

Mr. Frédéric C., Mr. Sergei R., Mr. Tom W., thank you all for producing fantastic pieces of music, which provided my personal soundtrack during the many hours of coding and writing.

J., H., thank you for your motivational teaching that made me become interested in physics.

A., thank you for a (almost) last proofreading of my thesis; D. (+K.), thank you (once again), for helping with the samenvatting.

Last but not least, I like to thank my loyal friends from Germany for keeping in very good contact despite the long distance and above all my family, in particular for providing a valuable place called “home” to which one can always come back to, even if only for a weekend.

A., thank you for everything.